

Binding Topologies of Amino Acid Binary Systems by Infrared Multiphoton
Dissociation (IRMPD) Spectroscopy

by

Haolu Wang

A thesis submitted in partial fulfillment of the requirements for the degree of

Master of Science

Department of Chemistry
University of Alberta

©Haolu Wang, 2022

Abstract

Studies of amino acids are essential because they are one of the building blocks of larger biomolecules, and it is crucial for us to understand how they interact with each other to fulfill all these various biological functions in our daily life. One interesting and noticeable fact from previous studies is that the amino acids found in proteins almost always possess only the left-handed configuration. When an enantiomer of a chiral molecule shows a stronger interaction with one enantiomer of another chiral molecule than with its mirror image, chirality recognition is observed.

In the past few decades, gas phase rotational and vibrational spectroscopies have been used to investigate non-covalent interactions in chiral molecular aggregates and in particular homochiral and heterochiral molecular pairs. Among them, infrared multiphoton dissociation (IRMPD) spectroscopy is a powerful spectroscopic technique for its high detection sensitivity and its capability to access larger chiral molecular systems without the complications in solution, while providing structural information. The following chapters include detailed work using IRMPD spectroscopy to determine the conformational and energetic relationship of the proton bound homochiral and heterochiral serine-asparagine and valine-asparagine dimers, as well as whether chirality recognition could be observed between the binary systems of interest. How the non-covalent inter/intra-molecular interactions affect the preferred binary structures, in particular the role of a polar or a non-polar sidechain, is also investigated.

Preface

This thesis is based on a research project that was performed in the Xu and Jäger groups in the Department of Chemistry at the University of Alberta between September 2019 and November 2021. Chapter 3 of this thesis has been published as Wang, H.; Heger, M.; Al-Jabiri, M. H.; Xu, Y. Vibrational Spectroscopy of Homo- and Heterochiral Amino Acid Dimers: Conformational Landscapes. *Molecules* **2022**, *27*, 38. My contributions included sample preparation, data curation, theoretical calculations, data analysis, visualization, validation, original draft preparation, reviewing, and editing. Dr. Matthias Heger mentored me, taught me how to use the script he developed, and was responsible for data curation, theoretical calculation, formal analysis, visualization, supervision, writing, reviewing, and editing. Mohamad H. Al-Jabiri was involved in data curation, formal analysis, writing, review, and editing. Professor Yunjie Xu was the supervisory author and was involved in the design of the experiments, constructive feedback, and manuscript composition for all the presented work. Professor Jäger and Professor Xu co-supervised my work in coupling our infrared multiphoton dissociation (IRMPD) instrument with a helium nanodroplet isolation (HENDI) spectrometer which is briefly mentioned in Chapter 2.

Acknowledgements

I would like to express my sincere gratitude to my supervisor, Dr. Yunjie Xu. It was her who provided me with the opportunity to do research during my undergraduate period and gave me the opportunity to learn and grow during my graduate studies. I could never have managed to finish the manuscript without her. Yunjie is always passionate about science. Her critical thinking and constructive suggestions have inspired me always. I would also like to thank Dr. Wolfgang Jäger for his encouragement and valuable advice during my time of both study and research work.

I want to show my appreciations to the past and present members of the Xu and Jäger groups. I express my special thanks to Dr. Matthias Heger for all the knowledge, guidance, and insightful discussions. I am grateful to have the chance to do my first calculation and measurements with Joseph Cheramy during my undergraduate study. A “thank you” to many other members, including Dr. Fan Xie, Yanqing Yang, Arsh Hazrah, Mohamad H. Al-Jabiri, Qian Yang, Guojie Li, Bowei Wu, Raiden Speelman, Boyang Zhao, Jiarui Ma, Colton Carlson, and Mutasem Alshalalfeh, from whom I have learned a lot during my time in the group.

I am glad to have had Dr. Yoram Apelblat as my lab coordinator for Chemistry 10X. I appreciate all the support you have shown me. A big thank you to Dr. Anna Jordan for her patience and writing guidance. I am thankful to my committee member, Dr. James Harynuk, for guiding me through my graduate studies.

Finally, I would like to thank the support provided by my family, friends, and my partner Boqun Zhang. Thank you for the encouragement since the beginning of my journey. Special appreciations to my roommates, Jianing He and Xuying Zhan. Thank you for being supportive and cheering me up. You are family to me.

This research was funded by the Natural Sciences and Engineering Research Council of Canada, the Canadian Foundation of Innovation, the Alberta Enterprise and Advanced Education and by the University of Alberta. I also gratefully acknowledge the access to computing resources provided by Westgrid and Compute/Calcul Canada. I acknowledge the University of Alberta for a Harry Emmett Gunning Post Graduate Scholarship.

Table of Contents

Abstract.....	ii
Preface.....	iii
Acknowledgements.....	iv
List of Figures.....	vii
List of Tables.....	ix
List of Abbreviations.....	x
Chapter 1 Introduction.....	1
1.1 References.....	4
Chapter 2 IRMPD Instrumentation and Experimental Details.....	10
2.1 IRMPD Spectroscopy.....	10
2.2 Instrumentation and Experimental Setups.....	12
2.2.1 Ion Sources.....	14
2.2.1.1 The ESI Source.....	14
2.2.1.2 The Electron Impact (EI) Ionization Source.....	14
2.2.2 Quadrupole Mass Filter and Ion Guide.....	15
2.2.3 The IRMPD Section of “SCORPION”.....	16
2.3 Instrumentation Modifications.....	19
2.3.1 An Early Ion Source.....	19
2.3.2 Spray Stability Optimization.....	20
2.4 References.....	24
Chapter 3 Vibrational Spectroscopy of Homo- and Heterochiral Amino Acid Dimers: Conformational Landscapes.....	26
3.1 Introduction.....	26
3.2 Material and Methods.....	28
3.2.1 Sample Preparation.....	28
3.2.2 Computational Details.....	29
3.2.3 IRMPD Experimental Details.....	29
3.3 Results and Discussion.....	30

3.3.1 Possible Low Energy Structures of the Four Diastereomers	30
3.3.2 Different Non-Covalent Binding Topologies	33
3.3.3 Comparison of the Experimental and Theoretical IRMPD Spectra.....	37
3.3.4 Chirality Recognition and Kinetic Effects in the IRMPD Spectra	41
3.3.5 Fragmentation Channel.....	47
3.4 Conclusions.....	49
3.5 Supplementary Data.....	49
3.6 References.....	50
Chapter 4 Conclusions and Future Applications	58
4.1 References.....	59
Bibliography	60
Appendix A Vibrational Spectroscopy of Homo- and Heterochiral Amino Acid Dimers: Conformational Landscapes	72

List of Figures

Figure 2-1. Schematic representation of IRMPD mechanism	11
Figure 2-2. Layout of the SCORPION instrumentation	12
Figure 2-3. View of the IRMPD section of the SCORPION instrument	13
Figure 2-4. View of the HENDI section of the SCORPION instrument	13
Figure 2-5. Matthieu stability diagram	16
Figure 2-6. Laser station of IRMPD instrumentation (b) with (a) extension of the pathway to the 3DIT	17
Figure 2-7. Experimental IRMPD spectrum of heterochiral HSerAsn ⁺ dimer under 5 mJ and 15 mJ irradiation energies	19
Figure 2-8. ESI setup (a) from the top view and (b) from the front view	21
Figure 2-9. Picture of (a) the capillary clogged by a large droplet and (b) the tip of a clogged capillary with visible sample residues under microscope	23
Figure 3-1. Correlation between 42 calculated <i>S,S</i> -HSerAsn ⁺ energies	32
Figure 3-2. Global minimum structures of the Type ZW, Type I and Type II binary species	33
Figure 3-3. Type I, II, III, and ZW binding topologies of <i>S,S</i> -HSerAsn ⁺ and <i>R,S</i> -HSerAsn ⁺	35
Figure 3-4. Type I, II, III, and ZW binding topologies of <i>S,S</i> -HValAsn ⁺ and <i>R,S</i> -HValAsn ⁺	36
Figure 3-5. The relative free energies of the four dimer species	37
Figure 3-6. Comparison of the experimental IRMPD spectra of <i>S,S</i> -HSerAsn ⁺ and <i>R,S</i> -HSerAsn ⁺ under two laser irradiation energies with the theoretical IR spectra of the most stable isomers of Type I, Type II, Type III, and ZW	38

Figure 3-7. Comparison of the experimental IRMPD spectra of <i>S,S</i> -HValAsn ⁺ and <i>R,S</i> -HValAsn ⁺ under two laser irradiation energies with the theoretical IR spectra of the most stable isomers of Type I, Type II, Type III, and ZW	41
Figure 3-8. NCI plots of the most stable homo- and heterochiral HSerAsn ⁺ at an iso-surface value of <i>s</i> =0.5	46
Figure 3-9. NCI plots of the most stable homo- and heterochiral HValAsn ⁺ at an iso-surface value of <i>s</i> =0.5	47
Figure A-1. IRMPD spectra at 15 mJ generated by using the HAsn ⁺ intensity directly and by taking into account the further fragmentation of HAsn ⁺	73
Figure A-2. Comparison of the theoretical and experimental IR spectra of <i>S,S</i> -HSerAsn ⁺	80
Figure A-3. Comparison of the theoretical and experimental IR spectra of <i>R,S</i> -HSerAsn ⁺	81
Figure A-4. Comparison of the theoretical and experimental IR spectra of <i>S,S</i> -HValAsn ⁺	82
Figure A-5. Comparison of the theoretical and experimental IR spectra of <i>R,S</i> -HValAsn ⁺	82
Figure A-6. Predicted IR spectra within the wavenumber region of 0-2650 cm ⁻¹ and 1000-1900 cm ⁻¹ of (a), (d) HSerAsn ⁺ Type I structures; (b), (e) HSerAsn ⁺ Type III structures; (c), (f) HValAsn ⁺ Type I structures.....	83

List of Tables

Table 3-1. The monomeric composition of the lowest energy isomers of each type of the four binary species studied.....	43
Table A-1. Calculated relative ZPE corrected electronic energies and Gibbs free energies of the <i>S,S</i> -HSerAsn ⁺ conformers and the percentage Boltzmann distribution of the free energy at room temperature	77
Table A-2. Calculated relative ZPE corrected electronic energies and Gibbs free energies of the <i>R,S</i> -HSerAsn ⁺ conformers and the percentage Boltzmann distribution of the free energy at room temperature.....	77
Table A-3 Calculated relative ZPE corrected electronic energies and Gibbs free energies of the <i>S,S</i> -HValAsn ⁺ conformers and the percentage Boltzmann distribution of the free energy at room temperature.....	78
Table A-4. Calculated relative ZPE corrected electronic energies and Gibbs free energies of the <i>R,S</i> -HValAsn ⁺ conformers and the percentage Boltzmann distribution of the free energy at room temperature.....	78
Table A-5. The monomeric composition of all isomers within 10 kJ mol ⁻¹ for the four binary species studied	79
Table A-6. Cartesian coordinates of the optimized isomers of <i>S,S</i> -HSerAsn ⁺	83
Table A-7. Cartesian coordinates of the optimized isomers of <i>R,S</i> -HSerAsn ⁺	95
Table A-8. Cartesian coordinates of the optimized isomers of <i>S,S</i> -HValAsn ⁺	106
Table A-9. Cartesian coordinates of the optimized isomers of <i>R,S</i> -HValAsn ⁺	114

List of Abbreviations

AC	Alternating Current
API	Active Pharmaceutical Ingredient
Asn	Asparagine
CC	Coupling Chamber
CREST	Conformer-Rotamer Ensemble Sampling Tool
DC	Direct Current
DC	Doping Chamber
DDET	Downstream Detector
DFT	Density Functional Theory
3DIT	3D-Quadrupole Ion Trap
EC	Extraction Chamber
ECD	Electron Circular Dichroism
ee	Enantiomeric Excess
EI	Electron Impact
ESI	Electrospray Ion Source
FTMW	Fourier Transform Microwave
HENDI	Helium Nanodroplet Isolation
HF	Hydrogen Fluoride
HLIT	HENDI Linear Ion Trap
ID	Inner Diameter
IDET	Inline Detector
IRMPD	Infrared Multiphoton Dissociation
IVR	Intramolecular Vibrational Redistribution
MD	Molecular Dynamics
MS	Extrel Quadrupole Mass Spectrometer Chamber
m/z	Mass-to-Charge
NC	Nozzle Chamber
NCI	Non-Covalent Interaction

OD	Outer Diameter
OPO	Optical Parametric Oscillator
PA	Proton Affinity
PDY	Photo-Dissociation Yield
PEEK	Poly-Ethyl Ethyl Ketone
Peni	Penicillamine
PTIG	Pre-Trapping Ion Guide
QTAIM	Quantum Theory of Atoms in Molecules
Quad	Quadrupole Mass Filter
RMSD	Root-Mean-Square Deviation
ROA	Raman Optical Activity
<i>R,S</i>	Heterochiral
Ser	Serine
SPIN	Sub-Ambient Pressure Ionization with Nano-Electrospray
<i>S,S</i>	Homochiral
TOF	Time-Of-Flight
Val	Valine
VCD	Vibrational Circular Dichroism
ZPE	Zero-Point Energy
ZW	Zwitterionic

CHAPTER 1

Introduction

The understanding of non-covalent interactions between chiral molecules is important to chemistry and life sciences. Even though a pair of enantiomers share the same chemical formula, they might exhibit very different responses when placed in a chiral environment, such as in stereo- sensitive chemical reactions or in human bodies. One of the widely known consequences of the different responses of a pair of enantiomers is the tragedy of birth defects caused by the misuse of thalidomide.^{1,2} In the late 1950s, thalidomide was found to have the ability to relieve morning sickness for pregnant women. However, for some women who took this drug during their pregnancy, their children were born with serious birth defects. Later, it was found that thalidomide was associated with severe teratogenic malformations because only the R enantiomer could suppress morning sickness actively, whereas the S enantiomer was the cause of these birth defects.^{2,3} The tragedy of thalidomide may not have been avoided by using just the R enantiomer because it was discovered later on that R and S enantiomers can interconvert in the human body,⁴ illustrating the complexity associated with chirality in medicine. This tragedy also emphasizes the importance of a better understanding of the chirality of molecular targets.

Studies of chiral molecular systems have been carried out extensively using many different spectroscopic techniques for the past few decades. For example, our research group has used chiroptical spectroscopies,⁵ such as electronic circular dichroism (ECD), vibrational circular dichroism (VCD), and Raman optical activity (ROA) extensively to probe the structural properties of chiral transition metal complexes,^{6,7} natural products,⁸ and also intermolecular interactions associated with chiral molecules directly in solution.^{9,10} In these solution studies, it was recognized that it sometimes is difficult to untangle spectral signatures of multiple species that co-exist in solution to extract the conformation specific structural information. In this regard, rotational spectroscopy coupled with a supersonic jet expansion has significant advantages and has been applied to probe non-covalent interactions in binary and even

larger clusters containing one or more (transiently) chiral molecules, for example, the methyl lactate-ammonia adduct¹¹ and the transiently chiral fluoroalcohol trimers^{12,13} and tetramers.¹⁴ In all these examples, conformer specific structure-energy information was extracted.

One area of special interest is related to the subject of chirality recognition. At the molecular level, we refer to the ability of a chiral molecule to differentiate a pair of enantiomers as chirality recognition. Without the complication of condensed phase perturbations, one can extract very detailed and precise information about structural and energetic properties of small chiral aggregates. For example, even small, relatively rigid chiral contact pairs or trimers, such as those containing propylene oxide,¹⁵⁻¹⁸ already show measurable chirality recognition. In another very recent example, Xie et al. demonstrated chirality-controlled structural preference in the dimers of tetrahydro-2-furoic acid using rotational spectroscopy and theoretical calculations.¹⁹ Indeed, this research effort has led to the application of chiral tag rotational spectroscopy for absolute configuration determination and enantiomeric excess (ee) determination.^{20,21} Studies on chirality recognition of neutral molecular complexes in a jet expansion also have been reported in the infrared and UV-vis regions, although less extensively.²²⁻²⁴ On the other hand, the size of molecular systems accessible for these gas phase studies is limited to about 300 to 500 mass units.

To access larger chiral molecular systems, while avoiding the complications in solution, we turned to a hybrid laser-mass spectroscopy, called infrared multiphoton dissociation (IRMPD) spectroscopy, which combines the detection sensitivity of mass spectrometry and the structural sensitivity of infrared spectroscopy.²⁵ In recent years, IRMPD spectroscopy has been applied to probe structural properties of some chiral molecular systems, such as amino acids in both the protonated²⁶⁻²⁸ and deprotonated forms,²⁹ and carbohydrates.³⁰ For example, with the use of ESI-MS, Fales and co-workers studied the structural changes of triethyl phosphate between protonation and sodium cationization,³¹ while Polfer et al. traced the binding pattern of complexes between tryptophan and alkali cations as a function of increasing cation sizes.³² The success of Kong's group in extracting structural information of ubiquitin ions with

different charges states, by comparison of IRMPD spectra and theoretical results, demonstrates that IRMPD is also a suitable method to understand some aspects of dissociation and dynamics of larger biomolecules, like protein ions.³³ Although conventional mass spectrometry is “blind” for stereochemistry analysis, several approaches have been developed to explore its potential application for stereochemical studies.^{34,35} With the aid of chiral ion mobility spectrometry, Dwivedi and co-workers were able to achieve enantiomeric separations successfully using (S)-(+)-2-butanol as a chiral modifier for a variety of racemates including but not limited to tryptophan, glucose and penicillamine.³⁶

Closely related to the current thesis work is the research effort in exploring the potential of IRMPD as a technique for elucidating the structural-energetic properties of homo- and hetero-chiral aggregates of amino acids³⁷⁻³⁹ and for stereochemical analyses. One well-known and noticeable fact is that the amino acids found in proteins almost always possess only the left-handed configuration. Several hypotheses have been proposed to explain why one enantiomer is naturally favored over the other.⁴⁰ With the bottom up, cluster science approach, IRMPD researchers have examined clusters of amino acid aggregates to look for possible clues. Among the aggregates of amino acids, the protonated serine octamer cluster is perhaps the most extensively investigated one for its unusual stability, originally reported by Cooks and co-workers.⁴¹ Subsequently, IRMPD spectroscopy has been applied by several research groups to study serine containing clusters, with the goal of gaining valuable structural information in order to provide a reasonable explanation for its “magic number” homochiral octamer preferences.^{8,42}

In my master’s thesis, I focused on two amino acid binary aggregates, specifically, the proton bound serine-asparagine complex and the valine-asparagine complex. We wanted to take a deeper look at the structural-energetic relationship of homochiral versus heterochiral proton bound serine-asparagine and valine-asparagine dimers using IRMPD spectroscopy and theoretical calculations, to evaluate potential aggregation preferences associated with chirality, and to analyze further the non-covalent interactions responsible for them. In general, precise information about the

structures and non-covalent interactions of amino acid monomers and their aggregates is important because these molecular systems are one of the essential building blocks of larger biomolecules. The knowledge of how two amino acids interact with each other at the molecular level provides a solid foundation to understand structure-function relationships of biological molecules in our body.

In total, this dissertation is divided into four chapters. In the following chapter, Chapter 2, I provide the relevant instrument details of each individual section of the IRMPD mass spectrometer, as well as the theoretical details for the conformational search of the molecular ions of interest, along with experimental details, including sample preparation and solutions to the problems that were encountered during the experiments. The main research results are provided in Chapter 3. Finally, a brief summary of my work and possible future plans are given in Chapter 4.

During my master study, I also was involved in the research effort to couple an existing helium nanodroplets isolation (HENDI) instrument^{43,44} with the IRMPD instrument⁴⁵ used in the current study. This work consists of testing the ion transfer efficiency to a new ion trap that is situated inside the HENDI instrument and is not included in the current thesis.

1.1 References

¹ Kim, J. H.; Scialli, A. R. Thalidomide: The Tragedy of Birth Defects and the Effective Treatment of Disease. *Toxicol Sci.* **2011**, *122*, 1-6.

² Lenz, W. Thalidomide and Congenital Abnormalities. *Lancet.* **1962**, *1*, 45-46.

³ Lenz, W. A Short History of Thalidomide Embryopathy. *Teratol.* **1988**, *38*, 203-215.

⁴ Eriksson, T.; Björkman, S.; Roth, B.; Fyge, A.; Höglund, P. Stereospecific Determination, Chiral Inversion in Vitro and Pharmacokinetics in Humans of the Enantiomers of Thalidomide. *Chirality* **1995**, *7*, 44-52.

⁵ Yang, G.; Xu, Y. Vibrational Circular Dichroism Spectroscopy of Chiral Molecules. *Top. Curr. Chem.* **2011**, *298*, 189-236.

-
- ⁶ Merten, C.; Hiller, K.; Xu, Y. Effects of Electron Configuration and Coordination Number on the Vibrational Circular Dichroism Spectra of Metal Complexes of *Trans*-1,2-Diaminocyclohexane. *Phys. Chem. Chem. Phys.* **2012**, *14*, 12884-12891.
- ⁷ Wu, T.; Li, G.; Kapitán, J.; Kessler, J.; Xu, Y.; Bouř, P. Two Spectroscopies in One: Interference of Circular Dichroism and Raman Optical Activity. *Angew. Chem. Int. Ed.* **2020**, *59*, 21895-21898.
- ⁸ Zhang, Y.; Poopari, M. R.; Cai, X.; Savin, A.; Dezhahang, Z.; Cheramy, J.; Xu, Y. IR and Vibrational Circular Dichroism Spectroscopy of Matrine- and Artemisinin-Type Herbal Products: Stereochemical Characterization and Solvent Effects. *J. Nat. Prod.* **2016**, *79*, 1012-1023.
- ⁹ Poopari, M. R.; Dezhahang, Z.; Xu, Y. A Comparative VCD Study of Methyl Mandelate in Methanol, Dimethyl Sulfoxide, and Chloroform: Explicit and Implicit Solvation Models. *Phys. Chem. Chem. Phys.* **2013**, *15*, 1655-1665.
- ¹⁰ Perera, A. S.; Thomas, J.; Poopari, M. R.; Xu, Y. The Clusters-in-a-Liquid Approach for Solvation: New Insights from the Conformer Specific Gas Phase Spectroscopy and Vibrational Optical Activity Spectroscopy. *Frontiers in Chemistry* **2016**, *4*, 9.
- ¹¹ Thomas, J.; Sukhorukov, O.; Jäger, W.; Xu, Y. Chirped-Pulse and Cavity-Based Fourier Transform Microwave Spectra of the Methyl Lactate...Ammonia Adduct: Lock and Key Selectivity and Internal Rotation Motions. *Angew. Chem. Int. Ed.* **2013**, *52*, 4402-4405.
- ¹² Thomas, J.; Seifert, N. A.; Jäger, W.; Xu, Y. A Direct Link from the Gas to the Condensed Phase: A Rotational Spectroscopic Study of 2,2,2-Trifluoroethanol Trimers. *Angew. Chem. Int. Ed.* **2017**, *56*, 6289-6293.
- ¹³ Thomas, J.; Liu, X.; Jäger, W.; Xu, Y. Unusual H-bond Topology and Bifurcated H-bonds in the 2-Fluoroethanol Trimer. *Angew. Chem. Int. Ed.* **2015**, *54*, 11711-11715.
- ¹⁴ Seifert, N. A.; Thomas, J.; Jäger, W.; Xu, Y. Rotational Spectra and Theoretical Study of Tetramers and Trimers of 2-Fluoroethanol: Dramatic Intermolecular Compensation for Intramolecular Instability. *Phys. Chem. Chem. Phys.* **2018**, *20*, 27630-27637.

-
- ¹⁵ Su, Z.; Borho, N.; Xu, Y. Chiral Self-Recognition: Direct Spectroscopic Detection of the Homochiral and Heterochiral Dimers of Propylene Oxide in the Gas Phase. *J. Am. Chem. Soc.* **2006**, *128*, 17126-17131.
- ¹⁶ Borho, N.; Xu, Y. Tailoring the Key in a Molecular Lock-and-Key Model System: The Propylene Oxide...2-Fluoroethanol Complex. *J. Am. Chem. Soc.* **2008**, *130*, 5916-5921.
- ¹⁷ Borho, N.; Xu, Y. Lock-and-Key Principle on a Microscopic Scale: The Case of the Propylene Oxide...Ethanol Complex. *Angew. Chem. Int. Ed.* **2007**, *46*, 2276-2279.
- ¹⁸ Xie, F.; Fusè, M.; Hazrah, A. S.; Jäger, W.; Barone, V.; Xu, Y. Discovering the Elusive Global Minimum in a Ternary Chiral Cluster: Rotational Spectra of Propylene Oxide Trimer. *Angew. Chem. Int. Ed.* **2020**, *59*, 22427-22430.
- ¹⁹ Xie, F.; Seifert, N. A.; Jäger, W.; Xu, Y. Conformational Panorama and Chirality Controlled Structure-Energy Relationship in a Chiral Carboxylic Acid Dimer. *Angew. Chem. Int. Ed.* **2020**, *59*, 15703-15710.
- ²⁰ Pate, B. H.; Evangelisti, L.; Caminati, W.; Xu, Y.; Thomas, J.; Patterson, D.; Perez, C.; Schnell, M. Quantitative Chiral Analysis by Molecular Rotational Spectroscopy. In *Chiral Analysis: Advances in Spectroscopy, Chromatography and Emerging Methods*, 2nd ed.; Elsevier, 2018, pp 679-729.
- ²¹ Domingos, S. R.; Pérez, C.; Marshall, M. D.; Leung, H. O.; Schnell, M. Assessing the performance of Rotational Spectroscopy in Chiral Analysis. *Chem. Sci.* **2020**, *11*, 10863-10870.
- ²² Medel, R.; Stelbrink, C.; Suhm, M. A. Vibrational Signatures of Chirality Recognition Between α -Piene and Alcohols for Theory Benchmarking. *Angew. Chem. Int. Ed.* **2019**, *58*, 8177-8181.
- ²³ Zehnacker, A.; Suhm, M. A. Chirality Recognition between Neutral Molecules in the gas phase. *Angew. Chem. Int. Ed.* **2008**, *47*, 6970-6992.
- ²⁴ Chai, H.; Chen, Z.; Wang, S.; Quan, M.; Yang, L.; Ke, H.; Jiang, W. Enantioselective Recognition of Neutral Molecules in Water by a Pair of Chiral Biomimetic Macrocyclic Receptors. *CCS Chem.* **2020**, *2*, 440-452.

-
- ²⁵ Polfer, N. C. Infrared Multiple Photon Dissociation Spectroscopy of Trapped Ions. *Chem. Soc. Rev.* **2011**, *40*, 2211-2221.
- ²⁶ Rajabi, K.; Fridgen, T. D. Structure of Aliphatic Amino Acid Proton-Bound Dimers by Infrared Multiple Photon Dissociation Spectroscopy in the 700-2000 cm⁻¹ Region. *J. Phys. Chem. A* **2008**, *112*, 23-30.
- ²⁷ Feng, R.; Yin, H.; Kong, X. Structure of Protonated Tryptophan Dimer in the Gas Phase Investigated by IRPD Spectroscopy and Theoretical Calculations. *Rapid Commun. Mass Spectrom.* **2016**, *30*, 24-28.
- ²⁸ Poline, M.; Rebrov, O.; Larsson, M.; Zhaunerchyk, V. Theoretical Studies of Infrared Signatures of Proton-Bound Amino Acid Dimers with Homochiral and Heterochiral Moieties. *Chirality* **2020**, *32*, 359-369.
- ²⁹ Scuderi, D.; Correia, C. F.; Balaj, O. P.; Ohanessian, G.; Lemaire, J.; Maitre, P. Structural Characterization by IRMPD Spectroscopy and DFT Calculations of Deprotonated Phosphorylated Amino Acids in the Gas Phase. *ChemPhysChem* **2009**, *10*, 1630-1641.
- ³⁰ Tan, Y.; Zhao, N.; Liu, J.; Li, P.; Stedwell, C. N.; Yu, L.; Polfer, N. C. Vibrational Signatures of Isomeric Lithiated N-acetyl-D-hexosamines by Gas-Phase Infrared Multiple-Photon Dissociation (IRMPD) Spectroscopy. *J. Am. Soc. Mass Spectrom.* **2017**, *28*, 539-550.
- ³¹ Fales, B. S.; Fujamade, N. O.; Oomens, J.; Rodgers, M. T. Infrared Multiple Photon Dissociation Action Spectroscopy and Theoretical Studies of Triethyl Phosphate Complexes: Effects of Protonation and Sodium Cationization on Structure. *J. Am. Soc. Mass Spectrom.* **2011**, *22*, 1862-1871.
- ³² Polfer, N. C.; Oomens, J.; Dunbar, R. C. IRMPD Spectroscopy of Metal-Ion/Tryptophan Complexes. *Phys. Chem. Chem. Phys.* **2006**, *8*, 2744-2751.
- ³³ Yang, Y.; Liao, G.; Kong, X. Charge-state Resolved Infrared Multiple Photon Dissociation (IRMPD) Spectroscopy of Ubiquitin Ions in the Gas Phase. *Sci. Rep.* **2017**, *7*, 16592.

-
- ³⁴ Schug, K. A.; Lindner, W. Chiral Molecular Recognition for the Detection and Analysis of Enantiomers by Mass Spectrometric Methods. *J. Sep. Sci.* **2005**, *28*, 1932-1955.
- ³⁵ Han, D. -Q.; Yao, Z. -P. Chiral Mass Spectrometry: An Overview. *TrAC Trends Anal. Chem.* **2020**, *123*, 115763.
- ³⁶ Dwivedi, P.; Wu, C.; Matz, L. M.; Clowers, B. H.; Seims, W. F.; Hill, H. H. Jr. Gas-Phase Chiral separations by Ion Mobility Spectrometry. *Anal. Chem.* **2006**, *78*, 8200-8206.
- ³⁷ Sunahori, F. X.; Yang, G.; Kitova, E. N.; Klassen, J. S.; Xu, Y. Chirality Recognition of the Protonated Serine Dimer and Octamer by Infrared Multiphoton Dissociation Spectroscopy. *Phys. Chem. Chem. Phys.* **2013**, *15*, 1873-1886.
- ³⁸ Lepere, V.; Barbu-Debus, K. L.; Clavaguéra, C.; Scuderi, D.; Piani, G.; Simon, A. -L.; Chirot, R.; MacAleese, L.; Dugourd, P.; Zehnacker, A. Chirality-Dependent Structuration of Protonated or Sodiated Polyphenylalanines: IRMPD and Ion Mobility Studies. *Phys. Chem. Chem. Phys.* **2016**, *18*, 1807-1817.
- ³⁹ Cheng, R.; Loire, E.; Martens, J.; Fridgen, T. D. An IRMPD Spectroscopic and Computational Study of Protonated Guanine-Containing Mismatched Base Pairs in the Gas Phase. *Phys. Chem. Chem. Phys.* **2020**, *22*, 2999-3007.
- ⁴⁰ Podlech, J. Origin of Organic Molecules and Biomolecular Homochirality. *Cell. Mol. Life Sci.* **2001**, *58*, 44-60.
- ⁴¹ Cooks, R. G.; Zhang, D.; Koch, K. J.; Gozzo, F. C.; Eberlin, M. N. Chiroselective Self-Directed Octamerization of Serine: Implications for Homochirogenesis. *Anal. Chem.* **2001**, *73*, 3646-3655.
- ⁴² Kong, X.; Lin, C.; Infusini, G.; Oh, H. -B.; Jiang, H.; Breuker, K.; Wu, C. -C.; Charkin, O. P.; Chang, H. -C.; McLafferty, F. W. Numerous Isomers of Serine Octamer Ions Characterized by Infrared Photodissociation Spectroscopy. *ChemPhysChem* **2009**, *10*, 2603-2606.
- ⁴³ Raston, P. L.; Knapp, C. J.; Jäger, W. Rotovibrational Spectroscopy of Hydrogen Peroxide Embedded in Superfluid Helium Nanodroplets. *Phys. Chem. Chem. Phys.* **2011**, *13*, 18789-18798.

⁴⁴ Das, P.; Knapp, C. J.; Jäger, W. Ro-Vibrational Spectroscopy of the Formic Acid-*d*₁ Monomer Embedded in Helium Nanodroplets. *J. Mol. Spectrosc.* **2017**, *341*, 17-22.

⁴⁵ Herger, M.; Cheramy, J.; Xie, F.; Chen, Z.; Xu, Y. Structural and Energetic Properties of Protonated and Sodiated Asparagine Probed by a New Laboratory IRMPD Spectrometer. *J. Mol. Spectrosc.* **2018**, *352*, 36-44.

CHAPTER 2

IRMPD Instrumentation and Experimental Details

2.1 IRMPD Spectroscopy

Vibrational spectroscopy, also referred to as infrared spectroscopy, is used often to obtain information about molecular properties, assist in a deeper understanding of structural preferences, or identify unknown molecules. It measures the interaction of the infrared radiation with a sample in forms of absorption, emission, or reflection. Generally, when an infrared photon is in resonance with an allowed vibrational transition of a functional group of a molecule, the absorption of this resonant photon occurs, resulting in vibrational excitation of this specific vibrational mode. An IR spectrum typically is plotted with the frequency scale in wavenumbers, i.e., the reciprocal centimeters, cm^{-1} , against the light intensity.

In my MSc research, I utilized infrared multiphoton dissociation (IRMPD) spectroscopy, a type of action spectroscopy in the infrared region. Compared to traditional vibrational spectroscopy, instead of monitoring how the radiation intensity is affected by molecules, action spectroscopy follows how the molecules are affected by the radiation. IRMPD spectroscopy monitors the fragmentation of molecular ions that is caused by the absorption of multiple resonant photons. The absorbed energy from one photon at a resonant frequency is distributed to the other parts of the ion via intramolecular vibrational redistribution (IVR). This process happens quickly (sub-ns),^{1,2} and then the ion is ready to absorb another resonant photon. The IVR mechanism is illustrated by Figure 2-1. As shown in the figure, each absorption of a resonant photon increases the internal energy of the parent ion, and this process repeats itself until the internal energy of the ion exceeds the dissociation threshold, resulting in fragmentation of the parent ion.

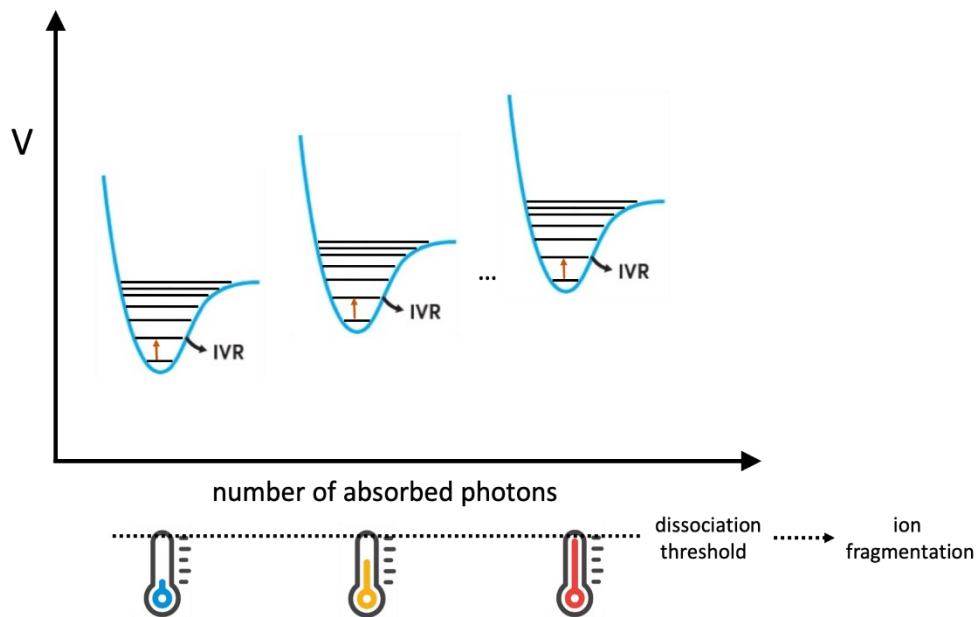


Figure 2-1. Schematic representation of IRMPD mechanism. The absorbed energy is distributed to other parts of the molecular ion through IVR. This allows the ion to accept the energy from another resonant photon. The molecular ion keeps absorbing resonant photons until the internal energy reaches the dissociation threshold, resulting in fragmentation of the molecular ion.

After fragmentation, a mass spectrum of all the fragments and the remaining parent ions is collected. The overall photo-dissociation yield (PDY) at each laser frequency is calculated using the following formula:

$$PDY = \frac{\sum_i I_i}{I_p + \sum_i I_i} \quad (2.1)$$

where I_p is the intensity of the molecular ion after dissociation and I_i is the intensity of the detected fragment ions. The contribution of each individual fragment ion can be represented by:

$$PDY_i = \frac{I_i}{I_p + \sum_i I_i} \quad (2.2)$$

with the summation of all PDY_i for each fragment ions equal to the overall PDY, i.e., $PDY = \sum PDY_i$.

The PDY is plotted against the laser wavenumber to produce the IRMPD spectrum, from which structural information can then be extracted.

2.2 Instrumentation and Experimental Setups

The experiments presented in this thesis have been carried out using our newly built IRMPD mass spectrometer.³ We nick-named the instrument “SCORPION” because of its overall shape resembling that of a scorpion. There have been several modifications made compared to our previous publication.³ A schematic overview is provided in Figure 2-2, along with two photographs of the instrument in Figure 2-3 and Figure 2-4 for comparison.

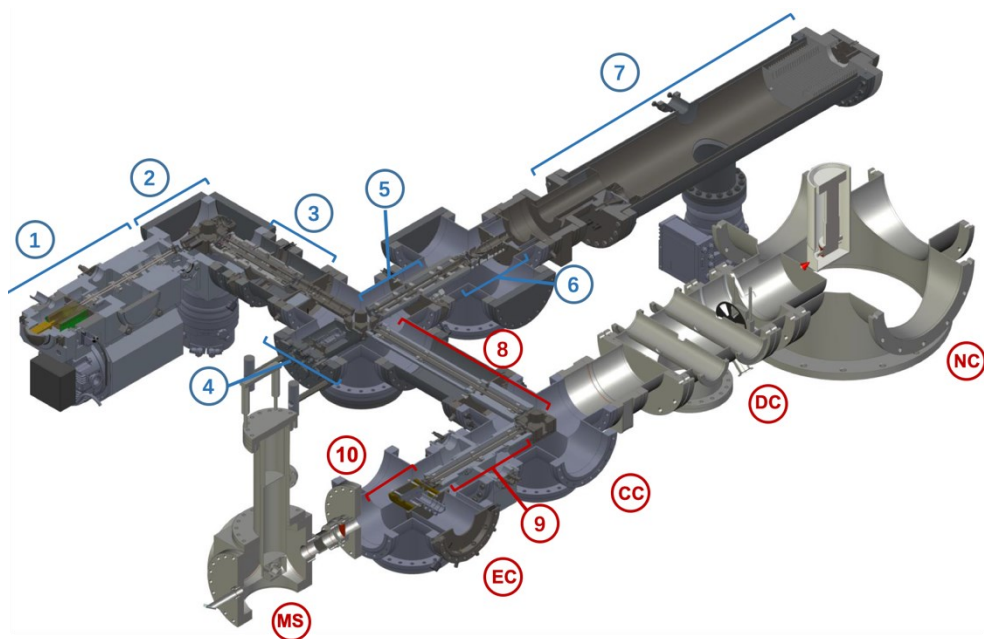


Figure 2-2. Layout of the SCORPION instrument. IRMPD components are labeled in blue: 1 ESI source, 2 Source Deflector/EI Source Cube, 3 Quadrupole (Quad), Ion lenses/ Inline detector (IDET), 4 Downstream Deflector/ Detector (DDet), 5 IRMPD Pre-Trapping Ion Guide (PTIG), 6 3D Ion Trap (3DIT), 7 TOF. HENDI components are labeled in red: 8 HENDI Coupling Ion Guide/HENDI Deflector, 9 HENDI Linear Ion Trap (HLIT), 10 HENDI Extractor, NC Nozzle Chamber, DC Doping Chamber, CC Coupling Chamber, EC Extraction Chamber, MS Extrel Quadrupole Mass Spectrometer Chamber.

As introduced in the above section, IRMPD has the advantages of detection sensitivity of mass spectrometry and the structural sensitivity of infrared spectroscopy. The instrumentation contains two parts: the mass spectrometer section and the laser section. The mass spectrometer section of the instrumentation can be divided into three main components: a nano-electrospray ion source (ESI) that is responsible for ion production; a quadrupole mass filter (Quad) and the following located ion guide that

are in charge of ion selection and transfer; and finally, a Time-Of-Flight (TOF) mass spectrometer at the end of the instrument, which is used for signal detection. The laser spectroscopy takes place in the 3D-quadrupole ion trap (3DIT) where the laser is shined into the ion trap and interacts with the trapped ions. In addition to the IRMPD arm described above, the instrument contains a second arm, which is designed for the helium nanodroplet isolation (HENDI) experiments.^{4,5}

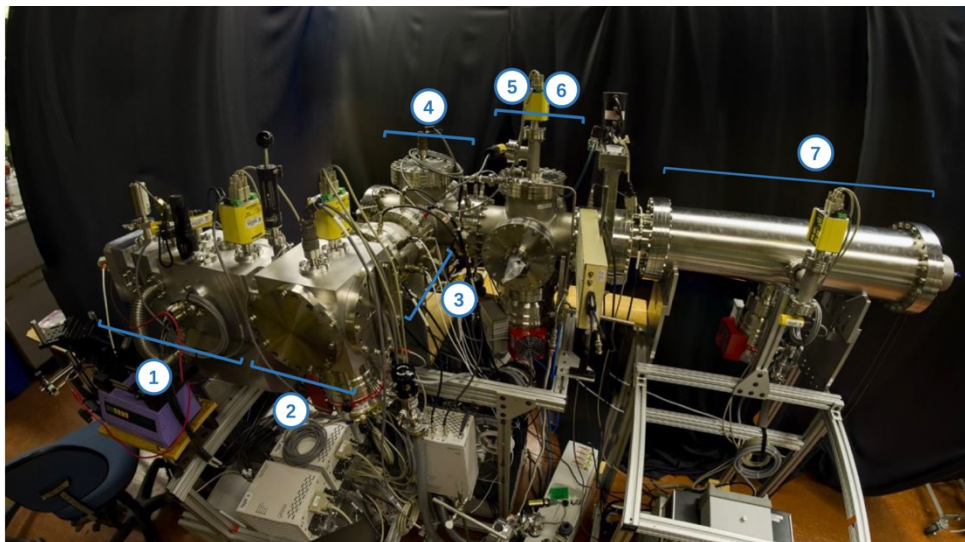


Figure 2-3. View of the IRMPD section of the SCORPION instrument with the same Labels as in **Figure 2-2.**

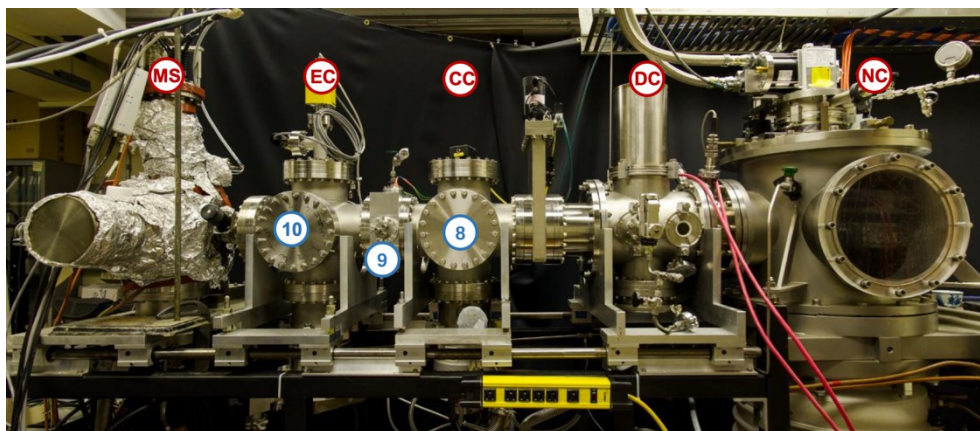


Figure 2-4. A photo of the HENDI section of the SCORPION instrument with the same Labels as in **Figure 2-2.**

2.2.1 Ion Sources

2.2.1.1 The ESI Source

The ESI device is responsible for ion production. It is a soft ionization method that is operated under atmospheric pressure. The setup is the same as in our previous “SCORPION” publication with some modifications made.³ The liquid sample is drawn into a microliter syringe (Hamilton Gastight 1710) which is installed onto the syringe pump (Harvard Apparatus 11Plus) that is set to a flow rate of 0.05 $\mu\text{l}/\text{min}$. The sample then flows through a section of PEEK (poly-ethyl ethyl ketone) tubing with an inner diameter (ID) of 65 μm that is connected to a metal union block. A high spray voltage of up to 400V, supplied by the Electrospray Source Controller on the device rack, is applied to de-solvate and ionize the sample solution.⁶ After that, the sample is injected to the spray emitter, which is composed of a fused-silica capillary with a typical ID of 20 μm and an outer diameter (OD) of 360 μm . The solution forms a Taylor cone and a fine filament of liquid. Relatively large droplets with charges are formed at first, while later they shrink in size due to evaporation. As the droplets evaporate, the surface tension of the droplets is smaller than the charge repulsion inside, which makes the droplets become unstable, break apart, and finally form a fine spray of charged gas phase ions. To help us establish a stable and efficient spray, the tip of the capillary is etched to a fine taper shape with an HF solution following the procedure by Smith et al.,⁷ while at the same time a flow of N_2 also is applied to improve the de-solvation of the sprayed droplets and provide a guidance of the spray to the ESI inlet.

2.2.1.2 The Electro Impact (EI) Ionization Source

Other than the ESI source mentioned above, another ionization device we have in the instrument is an EI ionization source. This is a hard ionization method, which utilizes energetic electrons to interact with gas phase samples to produce ions.⁸ This source is robust and requires little maintenance. We use it as an ion source for testing the performance of the instrument only.

2.2.2 Quadrupole Mass Filter and Ion Guide

After the ionization, the gas phase ions are transferred through the ion funnel to reach the source deflector and are deflected by 90° so that they are passed to the quadrupole mass filter. In the quadrupole mass filter, four parallel metal rods are used to create an electric field by applying a constant direct current (DC) voltage to one pair of opposite rods and also a simultaneous alternating current (AC) to the second pair of opposite rods.⁹ By controlling the ratio between the AC and DC voltages, a narrow mass band filter can be produced. The created electric field acts as a mass filter that deflects ions with a specific mass-to-charge (m/z) ratio, which we call resonant ions, so that they can pass through the filter, while the other non-resonant ions are neutralized by colliding with the rods as they migrate along. The ions selected by the quadrupole mass filter are transferred into the ion guide. We had an inline detector installed at the end of the filter for testing and debugging purposes. This allows us to check if the ions are transmitted through the quadrupole mass filter successfully.

In addition, the “RF-Only” option is used to work as a non-selective ion guide to transfer ions of a wide range of masses by applying no DC voltages to the poles.¹⁰ Since nothing is filtered out, the stability of the spray can be determined by the mass spectrum obtained, and further adjustments can be made. The way by which the “RF-Only” mode works can be explained by the Mathieu stability diagram. Below, an explanation based on my understanding is provided. An explanation of the Mathieu equations and other details can be found in several well-written papers, for example, by Pedder^{11,12} and by Miller and Denton.¹⁰

Figure 2-5 shows an example of a Mathieu stability diagram of an ion at m/z 230, plotted with the RF voltage on the x-axis and the DC voltage on the y-axis, along with a straight mass scan line. Whether ions of m/z 230 could be passed stably through the quadrupole for any set of RF and DC voltages can be read directly from the diagram. The area within the “triangular-like” boundaries represents the set of voltages where the ions are stable, and the area outside the boundaries represents the settings where the ions are unstable. When the quadrupole is set to the “RF-only” mode, the value of the DC component is always zero.¹³ The point of this setting would be found always on the x-axis, that is, always within the stable trajectory area no matter

what the m/z value is. This offers an explanation for the fact that ions at all m/z values are transferred stably through the quadrupole under the “RF-Only” mode. In this way, the quadrupole mass filter works as a non-selective ion guide, providing a detailed profile on ion existing as they are transferred stably through the quadrupole.

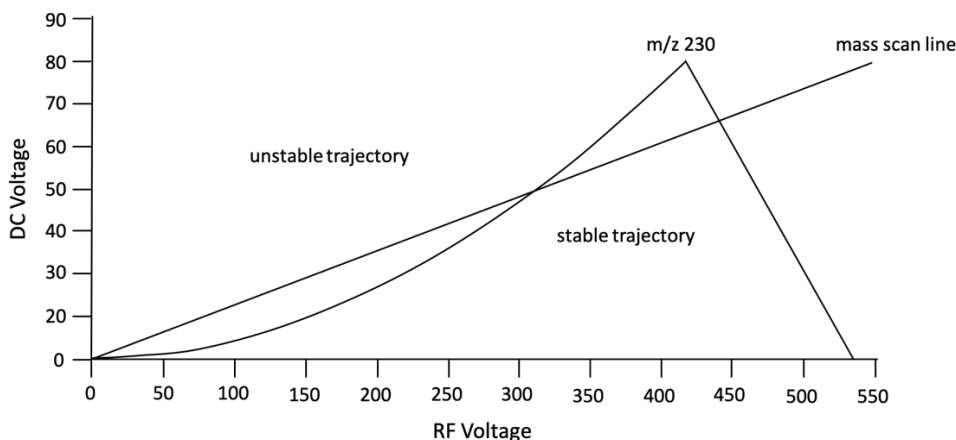


Figure 2-5. Mathieu stability diagram for an ion with m/z 230 plotted in RF-DC voltage space, showing a straight mass scan line through the origin.^{11,12} The region within the boundaries illustrates the voltage settings where the ion with a certain m/z is stable. Outside the boundaries the ion is unstable and cannot be transferred through the quadrupole.

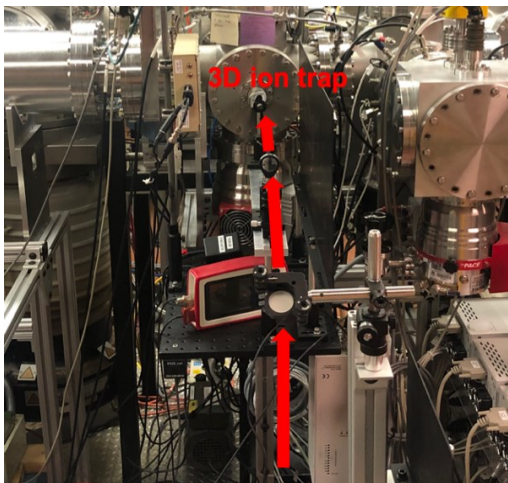
2.2.3 The IRMPD Section of “SCORPION”

Ions with a specific m/z are filtered out and passed to the downstream deflector to make another 90° turn in order to arrive at the rectilinear ion guide located in the IRMPD “arm” of the whole instrument.

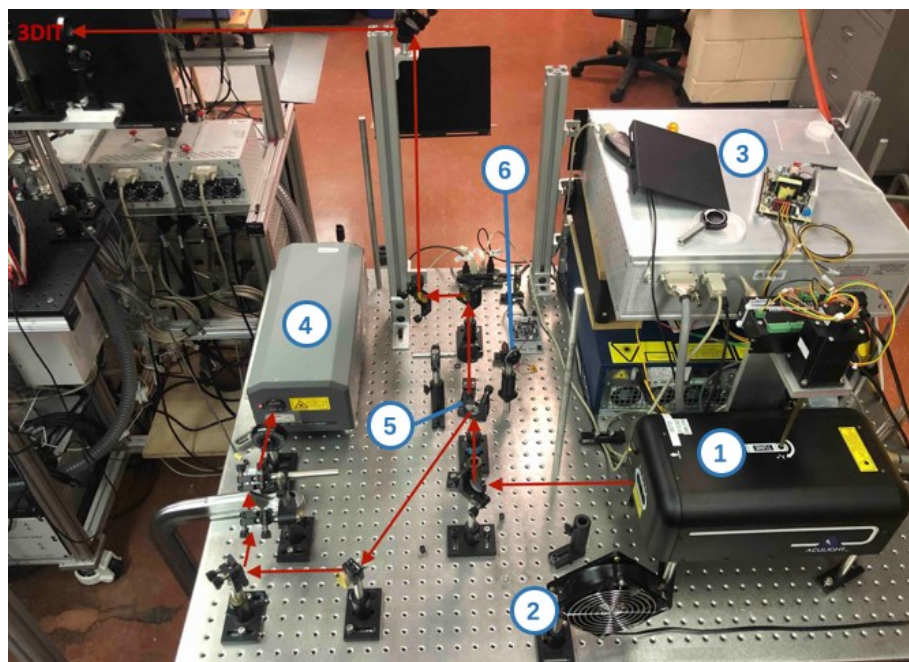
The three segments of the rectilinear ion guide are supplied with gradually increasing positive voltages in order to slow down the ions before they enter the 3D ion trap. The trap is filled with a small amount of helium gas so that the helium atoms can collide with the gas phase ions and cool them down in order to have them trapped inside the 3DIT. Then, the trapped ions are ready to receive the laser irradiation.

Figure 2-6 illustrates the laser path with the important elements labeled. The optical parametric oscillator (OPO) laser beam is directed through several mirrors and straightly onto the ions inside the 3DIT through a CaF_2 window. About 80% of the laser power goes into the 3D ion trap, whereas the remaining 20% goes to the wavelength meter (Bristol Model 621), providing an accurate wavenumber reading of the laser beam. When the absorbed photon is in resonance with a vibrational band of a

trapped ion, fragmentation occurs, and a mass spectrum of the fragmented ions is obtained by passing them to the TOF mass spectrometer at the end of the instrument. Then, structural information and chirality information can be extracted by comparing the theoretical and experimental IRMPD spectra.



(a)



(b)

Figure 2-6. Laser station of the IRMPD instrument with laser pathway labeled in red arrows and important elements labeled in blue. (a) Is the extension of the pathway to the 3DIT that is not shown in (b), which has the following labels: 1 OPO laser, 2 beam dump fan, 3 OPO controller/ Seed laser/ Seed Amplifier, 4 Wavelength Meter, 5 CaF₂ Window, 6 Laser Shutter. Missing from this picture: Beam dump next to beam dump fan, power meter and beam alignment apertures.

In our IRMPD experiments, two tunable, continuous wave, optical parametric oscillator (OPO) lasers, Module B and Module C, are used. Module B and C are specified to cover a range of 3200 to 3800 cm^{-1} wavenumbers and a range of 2600 to 3200 cm^{-1} , respectively. However, in operation, Module B could not reach as low a value as specified due to an absorption feature of the nonlinear crystal, while Module C could not reach as high a value as specified because of the dropping off of the output power at the interface between two modules. Figure 2-7 shows an experimental IRMPD spectrum of heterochiral protonated serine-asparagine (*R,S*-HSerAsn⁺) dimer. The unavailable wavenumber regions of our OPO laser are indicated by the shaded regions from 3120 to 3220 cm^{-1} and from 3400 to 3420 cm^{-1} . The experimental IRMPD spectra were recorded by taking wavenumber spacing of 5 cm^{-1} between 2600 and 3800 cm^{-1} at two irradiation energies, 5 mJ and 15 mJ. The setting of two irradiation energies was utilized since a low laser power is sometimes not powerful enough to break a vibrational bond and thus useful molecular information could not be extracted. For instance, the shoulder peak around 3525 cm^{-1} is noticeable at 15 mJ, and not visible under the 5 mJ condition. Operating at both low and high irradiation energies allows us to understand the fragmentation mechanism better and, therefore, the structural preferences of the molecular dimers.

To ensure the irradiation energy is kept the same at all times during the experiments, a remotely controlled laser shutter was installed to meet this purpose. This installation offered us the opportunity to control the irradiation time length and also the irradiation energy for each measurement cycle. The irradiation energy is calculated using the following formula:

$$E_N = P_{\text{cw}} \times t_s \quad (2.3)$$

where E_N is for the nominal irradiation energy, P_{cw} is the laser power at each laser frequency, and t_s is the shutter opening time. By the use of a power meter, the laser power at a specific laser frequency can be measured. Then, the opening time of the laser shutter can be calculated using the above formula and controlled to maintain a constant laser irradiation energy when the shutter is open for laser experiments.

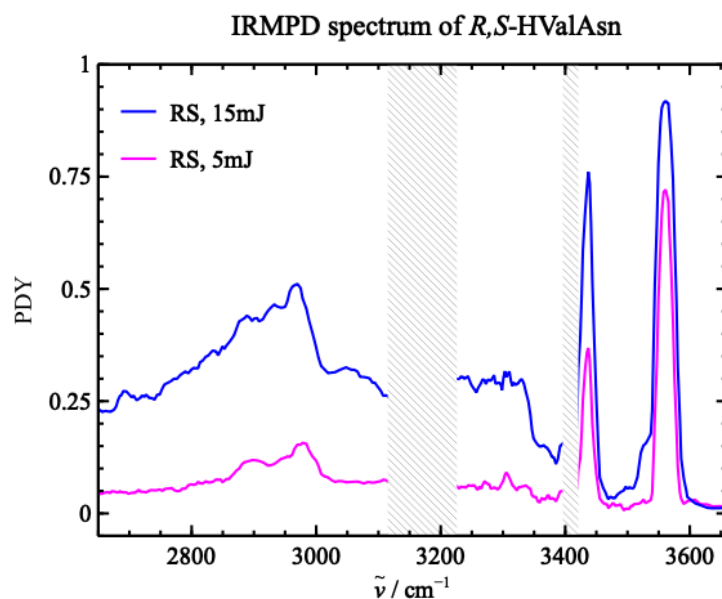


Figure 2-7. Experimental IRMPD spectra of the heterochiral HSerAsn⁺ dimer recorded with the 5 mJ and 15 mJ irradiation energies. The two unavailable frequency regions of the OPO laser are indicated by two shaded grey rectangles: from 3120 to 3220 cm^{-1} and from 3400 to 3420 cm^{-1} .

2.3 Instrumental Modifications

Over the past few years, we have made several modifications to the ESI source to maximize the signal intensity to the greatest extent, to establish a stable spray, as well as to handle the serious clogging issue that occurred both inside and outside the instrumentation. I summarize some of the modifications that I was involved with in this section. The current stage of the ESI source is shown in Figure 2-2 in the above section. With these improvements, we are now able to perform the experiments with a steady spray and obtain consistent experimental signals instead of spending a large amount of time stabilizing it.

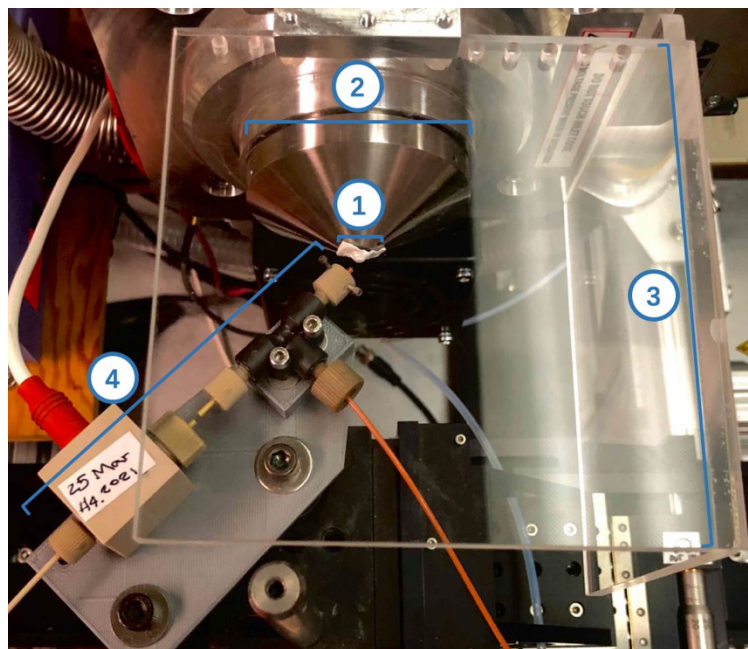
2.3.1 An Early Ion Source

Before the success with the current ESI source, we tested another ion source, which is called Sub-ambient Pressure Ionization with Nano-electrospray (SPIN) source. This source was invented by Smith, Tang, and co-workers.¹⁴⁻¹⁵ Unlike the usual atmospheric ESI device, which has a spray taking place outside the vacuum chamber, SPIN has the emitter capillary located inside the vacuum chamber so that the electrospray takes place

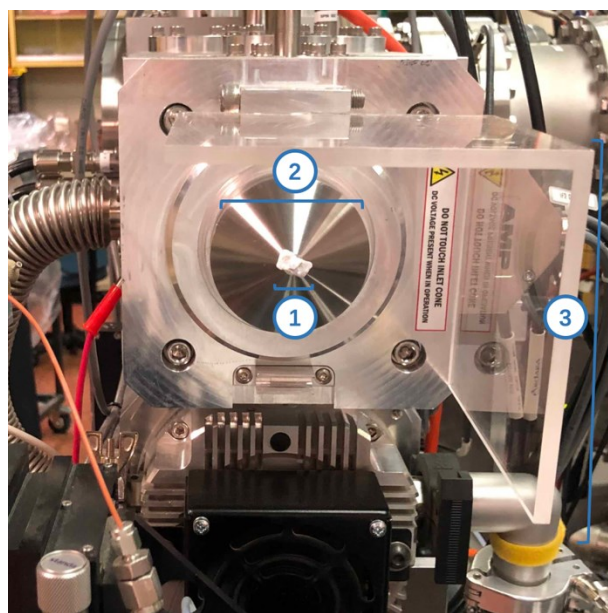
under a sub-ambient pressure environment. In order to aid the de-solvation of the sprayed sample droplets, a heated CO₂ flow also is added. Generally speaking, SPIN is an even softer and gentler ionization method compared to the soft ionization nano-ESI method. By eliminating the atmospheric-to-vacuum interface in the ion production step, the loss in ion abundance that occurs in traditional ESI setups can be avoided. Smith and co-workers showed that the SPIN source had a better performance than the normal atmospheric ESI source in transferring medium to large biological molecules into the gas phase without any noticeable fragmentation.^{16,17} Unfortunately, the SPIN source provided by the company did not perform as expected. Generally, a high concentration in the range of mM is needed for producing sufficient amino acid ions for detection in comparison to the typical μ M range used for a nano-ESI source. Frequent clogging inside the instrument under vacuum rendered the routine task of ion generation challenging. Consequently, we decided to stay with the traditional atmospheric ESI source described above.

2.3.2 Spray Stability Optimization

The signal intensity is optimized by changing the angle and the distance between the emitter capillary and the ESI inlet capillary. Figure 2-8 shows the setup of the ESI source that currently is used in our lab. A certain angle between the emitter capillary and the inlet is preferred since fewer neutral droplets are sprayed right into the inlet capillary. One important thing to note is that it is important to keep an eye on the distance between the capillary and the inlet. The tip of the capillary is etched by HF.¹⁶ This procedure helps to establish a stable and efficient spray. Note that the tip of the capillary is really fragile and can break by a simple touch.



(a)



(b)

Figure 2-8. Picture of the ESI setup currently used in our lab (a) from the top view and (b) from the front view. ESI components shown in (a) and (b): 1 inlet capillary covered by a piece of white tape, 2 metal cone, 3 acrylic safety shield, 4 capillary holder stage. The capillary holder stage is moved away from the inlet when the ion source is shut down to standby mode, therefore missing in (b).

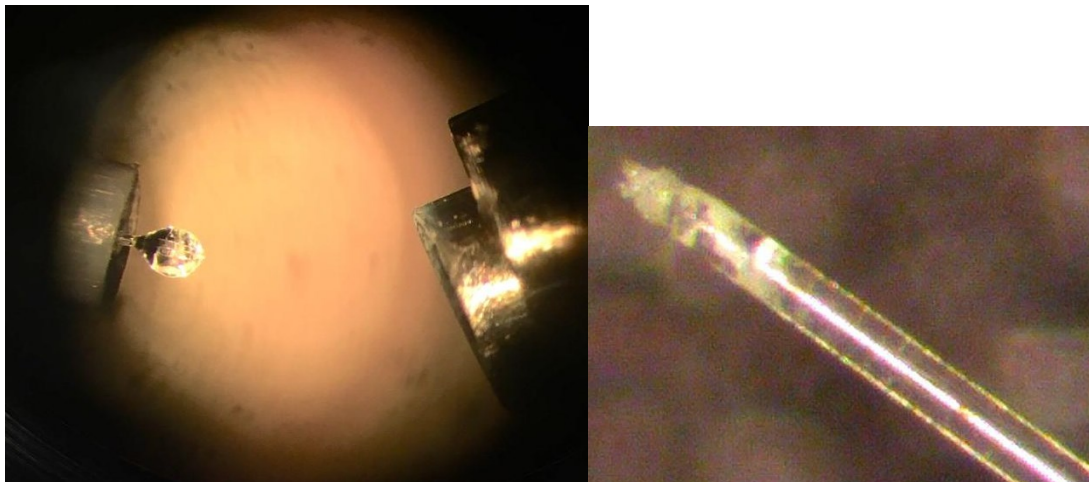
The stability of the spray is optimized in several ways. When drawing a liquid sample into the syringe, avoid the creation of air bubbles in the syringe. One must

remove air bubbles before carrying out further experimental steps. The presence of the air bubble will cause the ion signal to fluctuate noticeably. This then leads to a much longer time for the spray to stabilize. If air bubbles are noticed, it is good practice to empty the syringe and redraw the liquid sample to avoid bubbles, minimizing their influence on the stability of the spray.

An acrylic protective shield surrounding the ESI source, shown in Figure 2-8 (a) and (b), is added to minimize the inconsistency caused by the surrounding air flow interruption. From experience, it was established that the stability of the spray was affected by an unintentional air flow interruption. For example, there were a few times when the laboratory door was left open while the experiment was in operation, and the spray was unstable even after a few hours. After checking and eliminated all other possibilities of destabilization, the instability problem persisted. Working with the door closed during experiments seemed to help with the situation. Therefore, we established “closing laboratory door” as a standard step for the ESI operation and added an additional shield to minimize the effects of a sudden air flow change during experiments.

Unlike the SPIN source mentioned in the above section, whose emitter capillary is located inside the vacuum chamber so that the electrospray takes place under a sub-ambient pressure environment, and the clogging happens inside the vacuum. In our cases using ESI, clogging mostly happened at the tip of the capillary outside the instrument, i.e., under the ambient environment, and sometimes at the inlet capillary shown in Figure 2-8 (b). Figure 2-9 (a) shows a typical clogging issue occurring at the tip of the capillary, resulting in the formation of a large droplet at the tip. Since the sample solution is now forming a large droplet instead of a fine spray, the capillary is clogged, and no gas phase ions are generated/detected. Typically, the problem of clogging is noticed when there is a sudden drop in signal intensity. In order to observe ion signals of amino acid ions and especially their larger aggregates, we often needed to use concentrations in the mM range, rather than in the typical μM range. Under such conditions, if the flow rate is set to be relatively high, the de-solvation of the charged droplets may not be completed entirely, leading to the formation of the large droplets

at the tip of the capillary. The problem can be corrected by wiping the droplet off very gently and turning the flow rate down. If crystallization at the tip occurs, as illustrated in Figure 2-9 (b), one needs to replace the whole capillary.



(a)

(b)

Figure 2-9. Picture of (a) the capillary clogged by a large droplet and (b) the tip of a clogged capillary with visible sample residues under microscope.

As mentioned above, clogging occurring on the inlet also can affect the stability of the spray, causing a significant drop in the signal intensity. It is not easy to tell if the clogging happens at the emitter capillary or at the inlet. Normally, the condition of the emitter capillary is checked first since it is easy to verify this situation. If the possibilities of fault in all parts outside of the instrument are eliminated, clogging at the inlet is the next suspect. To solve the problem, the inlet capillary needs to be taken out and cleaned thoroughly by soaking it in and rinsing it with a methanol and water mixture to dissolve any contaminations. If the inlet capillary is clean, it has no influence on the stability of the spray. To protect the inlet capillary from unwanted contaminations when not used, a piece of white tape, as shown in Figure 2-8 (b), is used to cover the tip and assist the efficiency of the experiments.

2.4 References

- ¹ Lehmann, K. K.; Scoles, G.; Pate, B. H. Intramolecular Dynamics from Eigenstate-Resolved Infrared Spectra. *Annu. Rev. Phys. Chem.* **1994**, *45*, 241-274.
- ² Nesbitt, D. J.; Field, R. W. Vibrational Energy Flow in Highly Excited Molecules: Role of Intramolecular Vibrational Redistribution. *J. Phys. Chem.* **1996**, *100*, 12735-12756.
- ³ Heger, M.; Cheramy, J.; Xie, F.; Chen, Z.; Xu, Y. Structural and Energetic Properties of Protonated and Sodiated Asparagine Probed a New laboratory IRMPD Spectrometer. *J. Mol. Spectrosc.* **2018**, *352*, 36-44.
- ⁴ Raston, P. L.; Knapp, C. J.; Jäger, W. Rotovibrational Spectroscopy of Hydrogen Peroxide Embedded in Superfluid Helium Nanodroplets. *Phys. Chem. Chem. Phys.* **2011**, *13*, 18789-18798.
- ⁵ Das, P.; Knapp, C. J.; Jäger, W. Ro-Vibrational Spectroscopy of the Formic Acid-*d*₁ Monomer Embedded in Helium Nanodroplets. *J. Mol. Spectrosc.* **2017**, *341*, 17-22.
- ⁶ Heger, M. SCORPION User Handbook. **2021**.
- ⁷ Kelly, R. T.; Page, J. S.; Luo, Q.; Moore, R. J.; Orton, D. J.; Tang, K.; Smith, R. D. Chemically Etched Open Tubular and Monolithic Emitters for Nano-electrospray Ionization Mass Spectrometry. *Anal. Chem.* **2006**, *78*, 7796-7801.
- ⁸ Finlayson-Pitts, B. J.; Pitts Jr., J. N. Analytical Methods and Typical Atmospheric Concentrations for Gases and Particles. In *Chemistry of the Upper and Lower Atmosphere*; Academic Press, 2000; pp 547-656.
- ⁹ Kicman, A. T.; Parkin, M. C.; Iles, R. K. An Introduction to Mass Spectrometry Based Proteomics- Detection and Characterization of Gonadotropins and Related Molecules. *Mol. Cell. Endocrinol.* **2007**, *260-262*:212-227.
- ¹⁰ Miller, P. E.; Denton, M. B. The Transmission Properties of an RF-Only Quadrupole Mass Filter Mass Filter. *Int. J. Mol. Sci.* **1986**, *72*, 223-238.
- ¹¹ Pedder, R. E. Practical Quadrupole Theory: Graphical Theory. *Extrel Application Note RA_2010A*.
- ¹² Pedder, R. E. Practical Quadrupole Theory: Peak Shapes at Various Ion Energies. *Extrel Application Note RA_2011A*.

¹³ Somogyi, Á. Mass Spectrometry Instrumentation and Techniques. In *Medical Applications of Mass Spectrometry*; Elsevier, 2008; pp 93-140.

¹⁴ Page, J. S.; Tang, K.; Kelly, R. T.; Smith, R. D. A Subambient Pressure Ionization with Nanoelectrospray (SPIN) Source and Interface for Improved Sensitivity in Mass Spectrometry. *Anal. Chem.* **2008**, *80*, 1800-1805.

¹⁵ Cox, J. T.; Kronewitter, S. R.; Shukla, A. K.; Moore, R. J.; Smith, R. D.; Tang, K. High Sensitivity Combined with Extended Structural Coverage of Labile Compounds via Nanoelectrospray Ionization at Subambient Pressures. *Anal. Chem.* **2014**, *86*, 9504-9511.

¹⁶ Heger, M. SCORPION SOP: Hydrofluoric Acid Etching of Tapered-Tip ESI Emitters. **2021**.

CHAPTER 3

Vibrational Spectroscopy of Homo- and Heterochiral Amino Acid Dimers: Conformational Landscapes

3.1 Introduction

Chirality is essential for life. While a pair of enantiomers share the same chemical formula, their responses to the surrounding environment could be drastically different. *D*-Penicillamine (Peni) is widely used as a heavy metal antagonists due to its ability to bind with heavy metals such as copper and lead.¹ While its *D*-enantiomer works effectively in treating Wilson's diseases, *L*-Peni is toxic because of the inhibition of Vitamin B6 due to their interaction.² Similarly, the *R*-enantiomer of thalidomide was capable of efficiently suppressing morning sickness of pregnant women, however, the *S*-enantiomer was the cause of serious birth defects although it was discovered later that the *R*- and *S*- forms could interconvert in vivo.^{3,4} The potential lethal consequences associated with chirality in pharmaceuticals has led to tighter government regulations and further developments of spectroscopic tools for chirality evaluation.⁵

The regulatory demands and the urgent need for better chiral spectroscopic tools also have inspired considerable research effort in characterizing chirality recognition events at the molecular level to gain a fundamental understanding of the driving forces of such recognition events. Chirality recognition is defined as the ability of a chiral probe, for example, chiral light or a chiral molecule, to differentiate between the two enantiomers of a chiral molecule.⁶ We utilize chiral light, i.e., circularly polarized light, as the chiral probe used widely in chiroptical spectroscopies to determine the absolute configuration of the molecule.^{7,8} While chirality recognition is well known to play an important role in biological events and (supramolecular) organic syntheses, it is difficult to characterize the non-covalent intermolecular interactions responsible in detail in the condensed phase.

In the last fifteen years or so, gas phase rotational and vibrational spectroscopies have been utilized to explore the non-covalent intermolecular interactions, which lead to different preferred binding topologies for the homochiral and heterochiral aggregates

at the molecular level. For example, Zehnacker, Fujii and co-workers examined chirality discrimination between tyrosine and β -cyclodextrin using cryogenic ion trap IR spectroscopy to understand how the latter recognizes a chiral biomolecule.⁹ Jet-cooled Fourier Transform microwave (FTMW) spectroscopy has been applied to probe preferred binding topologies of some prototype systems, such as the dimers of propylene oxide,¹⁰ tetrahydro-2-furoic acid,¹¹ and glycidol.¹² The advent of the chirped pulsed FTMW technique,¹³ in combination with the fundamental FTMW research results, has led to the development of a chiral-tag rotational spectroscopic technique for enantiomeric excess, ee, determination.¹⁴ Although the extremely high-resolution capability of FTMW spectroscopy allows one to characterize complex conformational landscapes of these homo- and heterochiral complexes and differentiate structural isomers with minute differences, the size of possible molecular systems still is limited to about 30 heavy atoms. In this regard, infrared multiphoton dissociation (IRMPD) spectroscopy¹⁵ coupled with the electrospray ionization (ESI) technique offers some noticeable advantages in terms of its easy sample introduction and accessibility to larger molecular sizes.

IRMPD spectroscopy utilizes the detection sensitivity of mass spectrometry and the structural sensitivity of IR spectroscopy and has been applied extensively to probe structural properties of chiral molecular systems in the gas phase, such as charged amino acids and complexes containing amino acid subunits. For example, Polfer et al. traced the binding pattern of the complexes formed between tryptophan and alkali cations as a function of increasing cation sizes;¹⁶ Wu and McMahon examined the protonation sites and conformation of a series of amino acids;¹⁷ Rodgers and co-workers studied the structural variation between protonated and sodiated triethyl phosphate;¹⁸ and Andersson et al. examined the structural properties of proton-bound methionine and tryptophan dimers.¹⁹ More recently, IRMPD studies of homo- and heterochiral amino acid aggregates also have been reported. Among the aggregates of amino acids, serine is one of the most extensively investigated α -amino acids for its unusually stable protonated octamer clusters, originally reported by Cooks et al.²⁰ IRMPD spectroscopy has been applied by several groups to study serine clusters, with

the aim of gaining valuable structural information in order to provide a reasonable explanation for its “magic number” homochiral octamer preferences.²¹⁻²³ Related aggregates with one or more serine subunits within the octamer replaced with *S*- or *R*-threonine also were investigated to identify any substitution effect on the preferred structural topology of the octamer.²⁴ IRMPD chirality recognition studies very recently were reviewed by Kong and co-workers,²⁵ with a focus on the potential application of IRMPD spectroscopy in chiral analysis.

In this project, we investigated the structural and energetic relationships in the protonated homo- and heterochiral serine-asparagine and valine-asparagine dimers. One motivation is to evaluate the ability of asparagine to differentiate between a pair of enantiomers of an amino acid, an important requirement for a chiral discriminator in chiral analysis.²⁵ The choice of molecular systems was, in part, inspired by the previous report that asparagine can serve as an ee inducer in amino acid co-crystals.²⁶ The choice of the systems also was inspired by the very different experimental conformational distributions of neutral serine,²⁷ valine,²⁸ and asparagine²⁹ revealed by FTMW studies, where polar and non-polar sidechains were identified as one key factor of influence. It would be of interest to examine what role the polar or non-polar sidechains play in the respective dimer structures and how non-covalent interactions influence the conformational distributions of the neutral/charged amino acid subunits.

3.2 Materials and Methods

3.2.1 Sample Preparation

Both *SS* and *RS* sample solutions for the ESI production of HSerAsn⁺ and HValAsn⁺ were prepared using purified water and methanol as solvent at a volume ratio of 50:50. The asparagine, serine, and valine samples (Sigma-Aldrich) were used as received without further purification.

3.2.2 Computational Details

The conformational searches were done using the Conformer-Rotamer Ensemble Sampling Tool (CREST) program.³⁰ The low-level geometry optimization at the revPBE-D3/def2-TZVP level of theory and single point energy calculations at the B3LYP-D3/def2-TZVP level of theory were carried out using MolPro.^{31,32,33} The final full geometry optimization and harmonic frequency calculations at B3LYP-D3BJ/def2-TZVP level of theory were carried out using Gaussian software packages.³⁴

3.2.3 IRMPD Experimental Details

The experiments were carried out using a recently completed IRMPD mass spectrometer, “SCORPION”.³⁵ Briefly, the spectrometer consists of an electrospray ionization (ESI) source, a quadrupole mass filter, and two separate “arms”: one with a 3D Paul ion trap for IRMPD experiments, while the other, with a linear quadrupole ion trap is coupled to an existing helium nanodroplet isolation (HENDI) instrument.^{36,37} For the IRMPD experiments, we used a reflectron time-of-flight detector for the acquisition of the mass spectra. Two tunable, continuous wave OPO lasers (Lockheed-Martin Argos Aculight, modules B and C) were used as the IRMPD light source. Module B and Module C has two “blind regions” from 3400 to 3420 cm^{-1} and 3120 to 3220 cm^{-1} . A step size of 2 to 5 cm^{-1} and two nominal laser irradiation energies of 5 mJ and 15 mJ were used. The latter was achieved by installing a remote-controlled laser shutter in the laser beam path and controlling the irradiation timing to achieve the “nominal” irradiation energy (laser power times shutter opening time) during each measurement cycle. In the current setup, we recorded alternating “irradiated” and “non-irradiated” (background) mass spectra of the trapped ion samples, thus correcting for the self-dissociation of the targeted parent ions in the absence of laser irradiation, which otherwise would manifest itself in the IRMPD spectra as a baseline offset. An IRMPD spectrum was produced by plotting the photodissociation yield (PDY) with a 3-point moving average filter as a function of laser frequency.

During the IRMPD measurements of the dimers, when the laser was off, the monomer peak at the m/z of 133 for HAsn^+ was still observed, whereas no further fragmentation was detected for all the four dimer species. Therefore, the detected

monomer fragment peak at the m/z of 133 contains contributions from both the laser induced and the self-dissociated fragmentation of the binary amino acid complex. The contribution of the latter can be corrected easily using the usual background subtraction procedure.³⁸ A detailed procedure is provided in Appendix A.

3.3 Results and Discussion

3.3.1 Possible Low Energy Structures of the Four Diastereomers

While chemical intuition and prior experimental structural evidences had been used in some reports, such as in the infrared spectroscopic study of $(\text{Ser}_8\text{Cl}_2)^{2-}$ ³⁹ and $(\text{HSer}_8)^+$,²² increasingly a global search for suitable structures has been carried out by the laser-mass spectrometry community using some MD simulation program packages, such as Macromodel by Schrödinger,⁴⁰ and DFTB+, which utilizes a DFT-based tight binding method.^{41,42} For example, Poline et al. applied this approach to investigate theoretically the IR signature of several homochiral and heterochiral proton-bound amino acid dimers.⁴³ We chose to use the Conformer-Rotamer Ensemble Sampling Tool (CREST), developed by Grimme and co-workers.³⁰ CREST has been applied extensively and successfully to rotational spectroscopic studies of complex conformational landscapes of mid-sized neutral organic molecules and their clusters.^{44,45} Furthermore, it also was benchmarked for its ability to predict correct protonation sites.⁴⁶

In some recent rotational spectroscopic studies of fluoroalcohol trimers and tetramers,^{47,48} it was recognized that the monomeric conformations that are not stable in their isolated form may become the main or even the only subunits in the larger aggregates, highlighting the importance of extensive sampling of the conformational space in a global search of possible low energy structures of non-covalently bonded clusters. While each CREST run has already 12 built-in MD runs to cover as much conformational space as possible, multiple CREST runs with the same or different starting geometries were added. One reason is that while performing conformational analyses, we found that a high torsional barrier exists in all species, locking the OH group of the carboxylic group in either a cis or trans configuration relative to the C=O

group. A similar phenomenon was reported in the rotational spectroscopic studies of tetrahydro-2-furoic acid and its dimer.^{49,11} Since the CREST runs were unable to surmount these barriers with the default program settings, we manually screened for these different structure types by changing the input structures. In a single CREST run, redundant structures are removed by the program itself. Since many conformers found in different CREST runs also could be the same, we used a Python program to calculate the root-mean-square deviation (RMSD) of atomic Cartesian coordinates for the obtained conformations. An RMSD value of zero indicates identical conformations, whereas, the larger the value, the more unlike the two conformations are. By trial and error, an RMSD threshold of 0.6 was used for our molecular systems to remove the redundant geometries.

While some chose to use xTB energy directly to choose structural candidates for further DFT optimization, our experience with the neutral aggregates suggested that xTB energy ranking may be misleading in some cases.⁴⁵ An initial survey of the single-point energies of the CREST geometries was done, and the results suggested that such energy values were still too far from the final ones for them to be used as credible discriminators. Because of the large number of initial CREST candidates, we decided to add a few additional fast computational steps to obtain a more reliable energy ranking so that one could select properly the low energy structures for final geometry optimization and harmonic frequency calculations. These include: 1) CREST output; 2) DFT optimizations with a relaxed convergence criteria for each initial CREST candidate at the revPBE-D3/def2-SVP⁵⁰ level, with the empirical D3 dispersion correction;^{51,52} and 3) a single-point energy evaluation at the B3LYP-D3/def2-TZVP level of theory of the optimized structures in Step 2.

Figure 3-1 shows the relative energies for 42 *S,S*-HSerAsn⁺ structures at the three different calculation stages and their correlation with the final B3LYP-D3/def2-TZVP energies after geometry optimization using Molpro.^{31,32,33} It is apparent that GFN2-xTB generally underestimates the relative energies of the CREST conformers, resulting in an “over-crowded” initial conformer ensemble within a given energy window, making it difficult to carry out the selection. The revPBE relative energies, on

the other hand, tend to be overestimated. Finally, the single-point B3LYP calculations at the revPBE-optimized structures yield very reliable estimates of the final B3LYP-D3/def2-TZVP energies after geometry optimization, save for a few outliers. This combined B3LYP-D3/revPBE-D3 step is, therefore, crucial in assessing the conformer ensembles since it strikes a very attractive balance between computational effort and accuracy without requiring the full B3LYP-D3 optimizations.

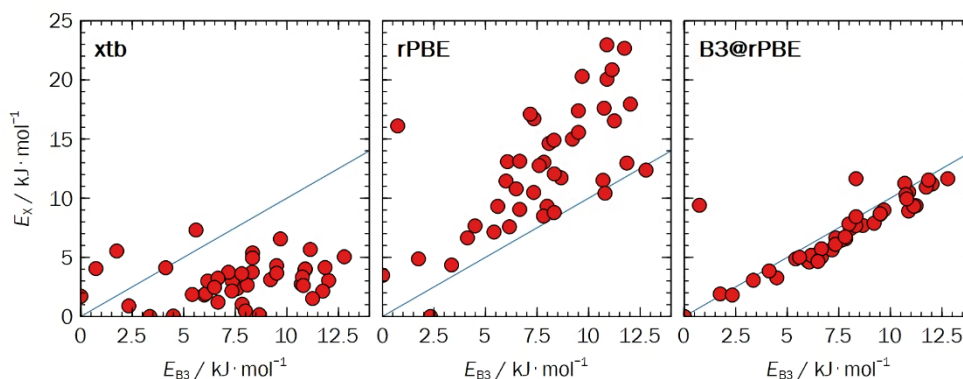


Figure 3-1. Correlation between 42 calculated S,S -HSerAsn⁺ energies, E_x , at various levels of computation with the final B3LYP-D3/def2-TZVP energies, E_{B3} . The blue line indicates that $E_x = E_{B3}$. From left to right: the GFN2-xTB energies from the CREST ('xtb'); revPBE-D3/def2-TZVP after geometry optimization ('rPBE'); and B3LYP-D3/def2-TZVP single-point calculations at the revPBE-optimized structures ("B3@rPBE").

For the four chiral diastereomers of interest, the final optimization and frequency calculation of the structures selected within ~ 10 kJ mol⁻¹ from the global minimum of each species were performed at the B3LYP-D3BJ/def2-TZVP level of theory using Gaussian 16.³⁴ The energetic properties and the associated Boltzmann factors are summarized in Appendix A for S,S -HSerAsn⁺, R,S -HSerAsn⁺, S,S -HValAsn⁺ and R,S -HValAsn⁺, respectively. The single-point energy calculations of all the above structures with the inclusion of a solvent polarizable continuum model (PCM) implemented in Gaussian 16³⁴ are also included in the corresponding Tables. Unsurprisingly, the zwitterionic (ZW) form of these binary clusters is strongly preferred with the inclusion of a solvent.

The global minimum structures of each species are presented in Figure 3-2 as well as the second most stable structures of S,S -HSerAsn⁺ and R,S -HSerAsn⁺. In addition, to visualize the full range of sidechain orientations that each dimer species

realizes within the 10 kJ mol^{-1} window, important atoms are color-coded. Then, the matching dots are used to indicate the positions of these specific atoms in all structures beyond the explicitly depicted minima. All these structures have the protonated side on serine or valine while asparagine takes on the neutral or ZW form.

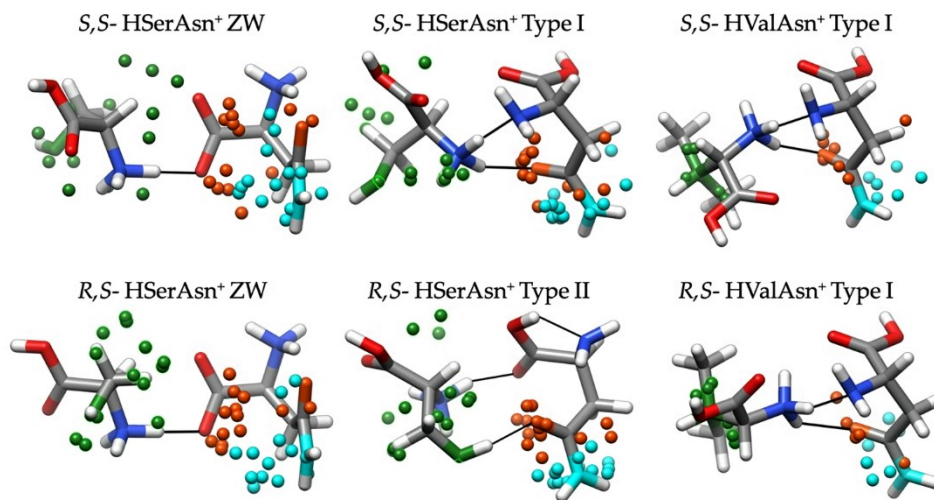


Figure 3-2. Global minimum structures of the Type ZW, Type I and Type II binary species. The O and N atoms in the asparagine sidechain are coloured in orange and turquoise, respectively, and the O and tertiary C atoms in the serine and valine sidechains are coloured in green. The additional points indicate the same sidechain atom positions among all other final structures.

3.3.2. Different Non-Covalent Binding Topologies

In the previous rotational spectroscopic studies of conformational landscapes of monomeric, neutral amino acids,⁵³ it was recognized that α -amino acids with a non-polar sidechain, such as valine, typically are present in only two dominant conformers stabilized by either a bifurcated $\text{N-H}\cdots\text{O}=\text{C}$ hydrogen bond with a *cis*-COOH configuration or a $\text{N}\cdots\text{H-O}$ hydrogen bond.²⁸ With the presence of polar sidechains, the number of conformers with similar energies tends to increase dramatically. For example, seven conformers were observed for neutral serine.²⁷ Interestingly, only one main conformer of asparagine was identified in the previous rotational spectroscopic study,²⁹ an exception to the rule. Generally, the greater conformational diversities of the serine monomer versus valine seems to be also reflected in their respective protonated binary species where the sidechain of the serine subunit as the tendency to occupy far more different regions in the above dimers than the sidechain of valine.

Asparagine utilizes only two structural configurations in the binary species studied here, although it can take on the neutral, protonated, or *ZW* forms, a point that will be discussed further in Section 3.3.4.

To appreciate the structural diversities in the homo- and heterochiral HSerAsn⁺ and HValAsn⁺ dimers better, we divided these isomers into five types, based mainly on their key intermolecular interaction difference, the subunit conformations, and whether the subunits take on the *ZW* form or not. These include Type I, II, and III of the protonated form, where the IR band signatures look very similar within each type but different from each other, then the *ZW* form, and finally some minor structures labelled as ‘Other’ that do not belong to the previous four categories. These labels also are listed in Appendix A for all four species. Based on the predicted relative free energies, Type I, II, and III of HValAsn⁺ make up almost all the population, whereas those labelled as ‘Other’ contribute very little. In contrast, for HSerAsn⁺, those labelled as “Other” have a higher contribution. This outcome is expected since the polar sidechain of serine offers more potential binding sites with asparagine.

In Figure 3-3, the geometries of the most stable isomers of each type of *S,S*-HSerAsn⁺ and *R,S*-HSerAsn⁺ are provided, where the dominant intermolecular hydrogen bonds are indicated. The relative ZPE corrected electronic energy (ΔE) and Gibbs free energy (ΔG) at room temperature in kJ mol⁻¹ at the B3LYP-D3BJ/def2-TZVP level of theory are included. Since the relative stability ranking of the isomers might change, based on ΔE or ΔG , we used ΔG for ranking. Type I structures contain two intermolecular hydrogen bonds connecting the NH₃⁺ group of serine with the nitrogen atom and the carbonyl oxygen of asparagine. Type II isomers have an intermolecular hydrogen bond between the serine NH₃⁺ group and the carboxyl O atom of asparagine and another from the serine OH group to the carbonyl O atom of asparagine. At the same time, the carboxyl OH group of asparagine maintains an intramolecular hydrogen bond with its own nitrogen atom where the backbone dihedral angle of asparagine subunit needs to be turned to facilitate this intramolecular hydrogen bond, leading to a slight destabilization of the whole structure. Type III isomers are unique compared to the other three because the protonation site is on the asparagine

subunit instead of serine. In Type III isomers, the nitrogen atom of serine forms an intermolecular hydrogen bond with the NH_3^+ group of asparagine, while an intramolecular hydrogen bond is formed between the carbonyl O atom of asparagine and its NH_3^+ group. As the asparagine subunit takes on the ZW form, there are two binding motifs identified for HSerAsn^+ : the polar sidechain of serine is 1) involved in the intermolecular interaction (ZW2) or 2) not (ZW1). By changing how a subunit approached the H(s) of the NH_3^+ group of serine to form the respective hydrogen bonding interactions, three isomers were found having Type I structures and two for each of Type II, III and ZW2.

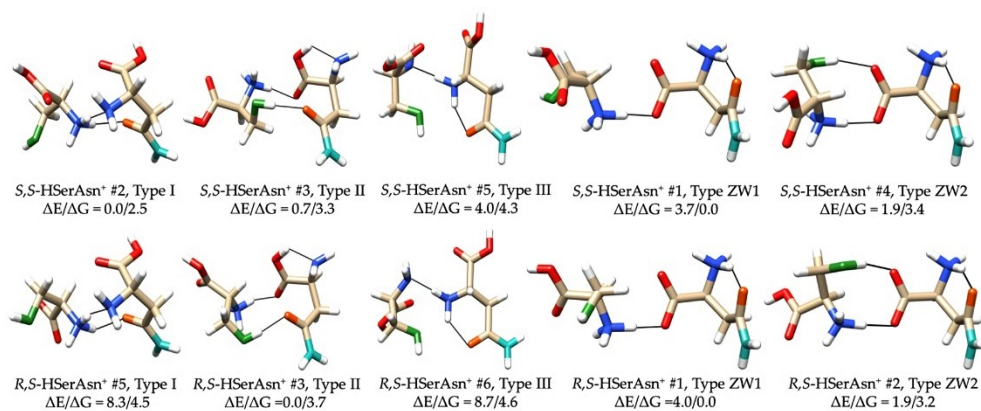


Figure 3-3. Type I, II, III, and ZW binding topologies of *S,S*-HSerAsn⁺ and *R,S*-HSerAsn⁺. The geometries shown are the most stable isomer in each type. The monomer subunit on the left is *S*- or *R*-serine while the one on the right is *S*-asparagine. The relative ZPE corrected electronic energy (ΔE) and Gibbs free energy (ΔG) at room temperature in kJ mol⁻¹ at the B3LYP-D3BJ/def2-TZVP level of theory are included. The ranking #1, #2, etc., is based on ΔG and is done for the homo- and heterochiral HSerAsn^+ , separately. The ΔE and ΔG values between the most stable isomer of *S,S*- and *R,S*-HSerAsn⁺ are 0.4 and 0.4 kJ mol⁻¹, respectively, with *S,S*-HSerAsn⁺ being the most stable one.

Similarly, the four types of binding topologies of *S,S*-HValAsn⁺ and *R,S*-HValAsn⁺ are depicted in Figure 3-4. Type I and II structures of the HValAsn⁺ species contain very similar intermolecular hydrogen bonds as in the corresponding Type I and II of the HSerAsn^+ species, respectively. The exception is that in the Type II of the HValAsn⁺ species, the COOH of valine acts as a proton donor instead of the OH group of serine in the HSerAsn^+ species case. This is not surprising since valine does not have an alcohol OH group. Type III of the HValAsn⁺ species utilizes the NH_3^+ of valine as the proton donor to the carbonyl and carboxylic O atoms of asparagine, a very different

binding topology compared to that of the HSerAsn⁺ species. Unlike HSerAsn⁺, only one binding motif is observed for ZW structures since their non-polar sidechain is not a competitive intermolecular hydrogen bond donor candidate compared to the OH group of serine.

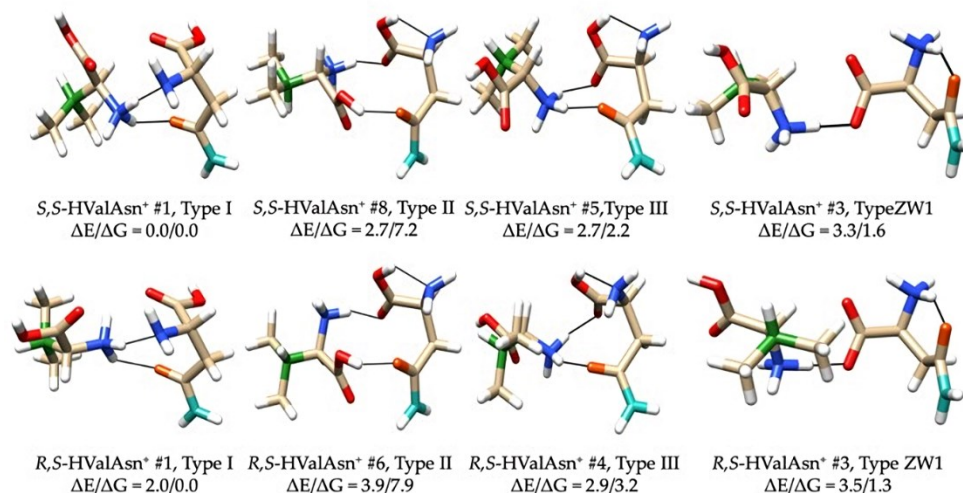


Figure 3-4. Type I, II, III, and ZW binding topologies of *S,S*-HValAsn⁺ and *R,S*-HValAsn⁺. The geometries shown are the most stable isomer in each type. The monomer subunit on the left is *S*- or *R*-valine, while the one on the right is *S*-asparagine. The relative ZPE corrected electronic energy (ΔE) and Gibbs free energy (ΔG) at room temperature in kJ mol⁻¹ at the B3LYP-D3BJ/def2-TZVP level of theory are included. The ranking #1, #2, etc., is based on ΔG and is done for the homo- and heterochiral HSerAsn⁺, separately. The ΔE and ΔG values between the most stable isomer of *S,S*- and *R,S*-HValAsn⁺ are 1.7 and 0.7 kJ mol⁻¹, respectively, with *S,S*-HValAsn⁺ being the most stable one.

Figure 3-5 visualizes the relative free energies of all final structures within the 10 kJ mol⁻¹ window for the four dimer species. The data points in each trace are coloured according to their binding topologies: Type I, II, III, ZW, and ‘Other’. In the case of the HSerAsn⁺ species, the lowest energy structure of the homochiral and heterochiral complex appear to be the same type, Type ZW. For the HValAsn⁺ species, the lowest energy structures of the homo- and heterochiral complex also appear to be the same type, Type I.

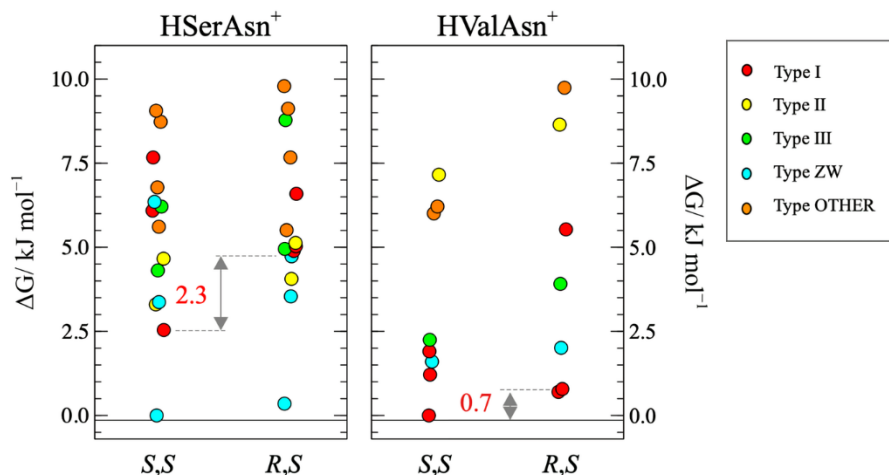


Figure 3-5. The relative free energies of the four dimer species. The energy gap between the experimentally observed Type I dimer structures of *S,S*- versus *R,S*-HSerAsn⁺ is indicated as 2.3 kJ mol⁻¹ and that of HValAsn⁺ is 0.7 kJ mol⁻¹.

3.3.3 Comparison of the Experimental and Theoretical IRMPD Spectra

Summaries of the IR spectra of all types of homo- and heterochiral HSerAsn⁺ and HValAsn⁺ are given in Appendix A. In Figure 3-6, the experimental IRMPD spectra of homo- and heterochiral HSerAsn⁺ dimers are compared with the theoretical, individual IR spectra of the most stable isomers of five relevant types. Both homo- and heterochiral experimental spectra show four clear band features, labelled as B, C, D, and E, in the region above 3200 cm⁻¹. Experimentally, there is also a small shoulder band to the lower cm⁻¹ side of D which only becomes obvious at a higher radiation power of 15 mJ. Based on the comparison between experimental and simulated spectral features, one can rule out contributions of Type II, ZW1 and ZW2 for both *S,S*-HSerAsn⁺ and *R,S*-HSerAsn⁺. Below, we focus on the remaining Type I and Type III structures.

For *S,S*-HSerAsn⁺, overall, Type I, #2 provides the best agreement with the experimental IR pattern, including the small shoulder band next to D and in terms of the predicted energetic preference, i.e., the most stable one among the remaining Type I and III. The other four isomers, i.e., Type I, #8 and #12, and Type III, #5 and #9, all show features consistent with C, D, and E. It appears that the contribution from them can be used to explain the broadening observed in the experimental D band and also

the much broader B band, where the corresponding calculated B bands of these isomers extend over about 10s of cm^{-1} .

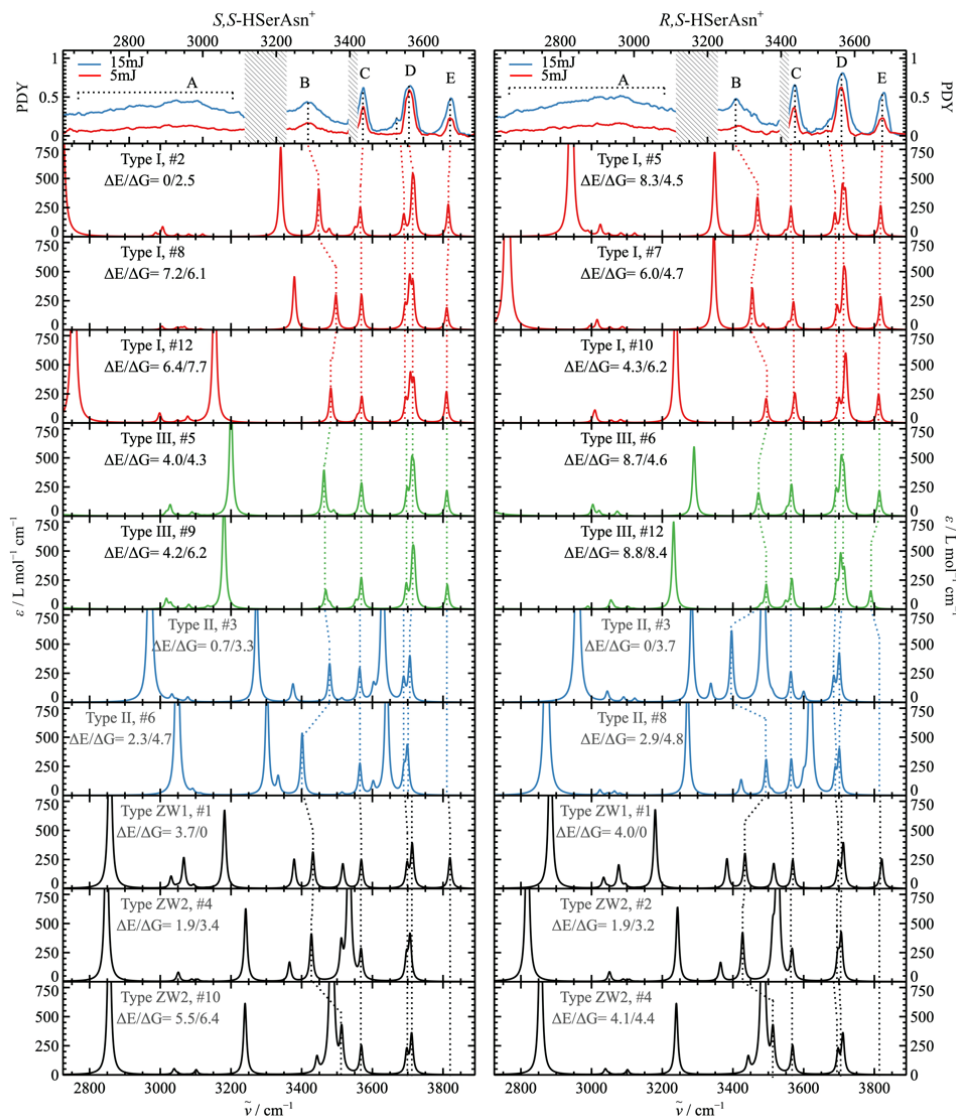


Figure 3-6. Comparison of the experimental IRMPD spectra of S,S -HSerAsn⁺ and R,S -HSerAsn⁺ under two laser irradiation energies with the theoretical IR spectra of the most stable isomers of Type I, Type II, Type III, and ZW. Top panel: experimental IRMPD spectra of S,S - and R,S -HSerAsn⁺ dimers under two laser energies. Lower panels: theoretical IR spectra of the most stable isomers of Type I (red), Type II (blue), Type III (green), and ZW (black). The relative electronic energy (ΔE) and Gibbs free energy (ΔG) values of respective isomers are given in the unit of kJ mol^{-1} . The theoretical IR bands correspond to the same (similar) vibrational motions are connected with the dashed lines which in turn connect to the experimental bands to indicate the assignment.

In terms of vibrational assignment, the highest frequency E band corresponds to the free OH stretch of serine that is not involved in the non-covalent intermolecular

interaction; the D band can be related to the carboxyl OH stretches of the serine and asparagine subunits. Neither of the carboxyl OH stretches are involved in the intermolecular hydrogen bonds, and they are predicted to be close in their frequencies. The “shoulder” peak (next to D) at $\sim 3550\text{ cm}^{-1}$ corresponds to the asymmetric stretching motions of the sidechain NH_2 group of asparagine. The C band contains the symmetric stretching information of the sidechain NH_2 group of asparagine as well as the asymmetric stretching motion of the proton acceptor NH_2 group of asparagine, whose intensity is lower and appear as a smaller “shoulder” in the predicted spectra. The B band is assigned to a collection of symmetric stretching motions of the proton acceptor NH_2 group of asparagine and the asymmetric NH_2 vibrations in the proton bound NH_3^+ groups of serine, analogously to the previously published assignments.²³ Note that the predicted proton bound NH_2 symmetric stretch band of serine falls into the “blind region” of our laser and could not be detected in the experiment.

In the region below 3200 cm^{-1} , the predicted IR bands are dominated by the stretching modes of NH_3^+ , which serves as a hydrogen bond donor in the dimers. These stretching bands exhibit typical characters, such as large red shifts and big enhancement in IR strength. Experimentally, it is well known in the jet cooled high resolution IR community that IR photons pumped into intermolecular hydrogen-bonds tend to lead to severe pre-dissociation broadening in the experimental IR spectra.⁵⁴ In the current case, this results in a broad and featureless contour which is marked as band A, similar to what was reported previously.²³ The backbone CH stretches from the asparagine and serine subunits are predicted to be in the $3000\text{-}3110\text{ cm}^{-1}$ region and tend to be featureless because of the high the density of CH vibrational states.²¹

For *R,S*-HSerAsn⁺, Type I, #5 and #7 isomers appear to provide the best agreement with the experiment, while contributions from Type I, #10 and Type II, #6 and #12 are also present. The IR band assignments for A-E remain analogous to those of *S,S*-HSerAsn⁺.

In Figure 3-7, the experimental IRMPD spectra of homo- and heterochiral HValAsn⁺ dimers are compared with the simulated individual IR spectra of the most stable isomers of Type I, II, III and ZW1. Type ZW2 is outside the 10 kJ mol^{-1} free

energy window. The most obvious difference to HSerAsn⁺ is the missing E band that belongs to the free OH of Ser since HValAsn⁺ does not have such a free OH group. Based on the simulated IR spectral patterns in the region surrounding the C band, we can rule out contributions of Type II and III. Both of them have a lower wavenumber band next to the predicted C band, which is not present in the experiment. The comparison of the simulated and experimental band gap between C and B'/B bands also allow one to discard the contribution of Type ZW1.

For *S,S*-HValAsn⁺, Type I, #1, #3 and #5 structures exhibit well-aligned C and D bands, i.e., very similar C and D frequencies among the three isomers, and more spread out B'/B bands, consistent with the experimental spectral appearance. The B and B' bands of the Type I structures are assigned to the symmetric and asymmetric stretches of the hydrogen bonded NH₃⁺ group of valine. The IR assignments of the C and D features are analogous to the HSerAsn⁺ case described above.

Similarly, for *R,S*-HValAsn⁺, Type I, #1, #2, and #5 structures contribute to the experimental IR spectra, as indicated by the good agreement with the experimental features. Contributions of Type II, III and ZW1 structures can be discarded for the same reasons provided for *S,S*-HValAsn⁺.

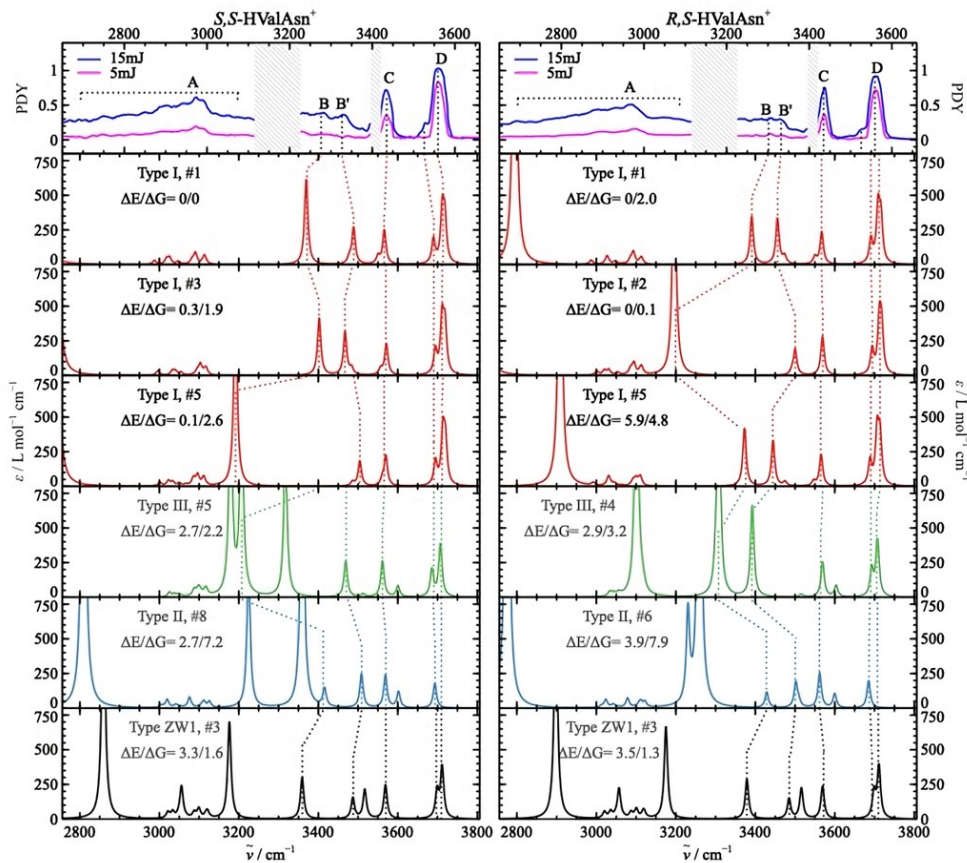


Figure 3-7. Comparison of the experimental IRMPD spectra of S,S -HValAsn⁺ and R,S -HValAsn⁺ under two laser irradiation energies with the theoretical IR spectra of the most stable isomers of Type I, Type II, Type III, and ZW. Top panel: experimental IRMPD spectra of S,S - and R,S -HValAsn⁺ dimers under two laser energies. Lower panels: theoretical IR spectra of the most stable isomers of Type I (red), Type II (blue), Type III (green), and ZW (black). The relative electronic energy (ΔE) and Gibbs free energy (ΔG) values of respective isomers are given in the unit of kJ mol^{-1} . The theoretical IR bands correspond to the same (similar) vibrational motions and are connected with the dashed lines which in turn connect to the experimental bands to indicate the assignment.

3.3.4 Chirality Recognition and Kinetic Effects in the IRMPD Spectra

The above IRMPD spectral analyses show that while one could discriminate clearly among different types of structures for the four binary species studied here, only minor differences between the homo- and heterochiral species of HSerAsn⁺ and HValAsn⁺ were observed experimentally. Does this mean that there is no or little chirality recognition in these homo- versus heterochiral species? In the following, we first address why the species which contribute to the experimental IRMPD patterns may not necessarily be the most stable structures that are predicted. Then, we discuss some noticeable chirality recognition signatures and energetic differences in these systems,

even if these are not reflected in the IRMPD features detected, and how one may tease out these signatures with modified experimental approaches.

Although the global minima predicted for both *S,S*-HSerAsn⁺ and *R,S*-HSerAsn⁺ belong to the ZW type, they were not observed experimentally. With respect to the most stable non-ZW heterochiral and homochiral dimer structures, *R,S*-HSerAsn⁺ Type II, #3 has a drastically different IR pattern compared to that of *S,S*-HSerAsn⁺ Type I, #2. This prediction appears to contradict the previous statement that experimentally only minor differences are present between the homo- and heterochiral IRMPD spectra (Figure 3-6). Furthermore, the observed heterochiral IRMPD spectra of HSerAsn⁺ can be accounted for mainly by *R,S*-HSerAsn⁺ Type I structures, with essentially no contribution from the *R,S*-HSerAsn⁺ Type II, #3 isomer, the most stable non-ZW form of *R,S*-HSerAsn⁺ predicted. While the predicted energy ordering or gaps may not be totally trustworthy, the level of theory used here generally has captured the energy ordering of similar neutral species quite well, as demonstrated by many examples reported by the rotational spectroscopic community.^{55,56} To explain the observation discussed above, we also examine if the amino acid dimers are formed mainly in solution or in the gas phase during the electrospray processes and the influence of the relative stabilities (i.e. abundances) of the monomeric subunits.

In Table 3-1, we list the monomeric composition of the most stable isomers of each type for HSerAsn⁺ and HValAsn⁺, while the related results of all low energy binary isomers are provided in Appendix A. In a previous study, Zhu et al.⁵⁷ estimated the degree of self-aggregation of serine in water with respect to the concentration. Eight different concentrations, ranging from 0.1 M to saturation, were studied, and no severe self-aggregation was observed in any of them. The concentration of our sample solution is ~3 mM, much lower than the concentrations used in the previous study, indicating that the formation of amino acid dimers in the mM solution is likely to be negligibly small. HSerAsn⁺ and HValAsn⁺ probably are formed mainly during the electrospray process. While amino acids exist mainly as zwitterions in pH (near) neutral aqueous solution, an isolated amino acid exists dominantly in a non-ZW form in the gas phase. This is the case even for the most basic amino acid arginine.⁵⁸ The poor stability of the

zwitterionic form in the gas phase provides an explanation for the non-observation of any binary species with zwitterionic subunits, irrespective of their predicted relative free energies.

Table 3-1. The monomeric composition of the lowest energy isomers of each type for the four binary species studied

ΔG^a	<i>S,S</i> -HSerAsn ⁺	<i>R,S</i> -HSerAsn ⁺	<i>S,S</i> -HValAsn ⁺	<i>R,S</i> -HValAsn ⁺
	Type, Ser/Asn Comp ^b	Type, Ser/Asn Comp	Type, Val/Asn Comp	Type, Val/Asn Comp
1	Type ZW1, HS1 ⁺ /ZW	Type ZW1, HS1 ⁺ /ZW	Type I, HV1 ⁺ /A1 ^c	Type I, HV1 ⁺ /A1 ^c
2	Type I, HS1 ⁺ /A1 ^c	Type II, HS3 ⁺ /A2	Type ZW1, HV1 ⁺ /ZW	Type ZW1, HV1 ⁺ /ZW
3	Type II, HS1 ⁺ /A2	Type I, HS1 ⁺ /A1 ^c	Type III, HV1 ⁺ /A2	Type III, HV1 ⁺ /A2
4	Type III, S1/HA ⁺ ^c	Type III, S1/HA ⁺ ^c	Type II, HV3 ⁺ /A2	Type II, HV3 ⁺ /A2

^a Ordering based on the free energy of the most stable isomer of each type. Note that the ordering of Type I and Type II of *S,S*- and *R,S*-HSerAsn⁺ are opposite.

^b The composition of the two monomeric subunits. S = Ser; V = Val; A = Asn. We add “H” and “+” for the protonated species, and 1, 2, etc., indicates the relative stability of the protonated subunit going from the most stable one to the least. For the neutral subunits, 1,2, etc. are used to indicate the structural difference among different subunits, rather than energy ordering because the structure inside a dimer species often differs greatly from its isolated ones. See the main text for discussions.

^c The shaded ones are those assigned, i.e., observed experimentally in Figure 3-6 and 3-7.

The homo- and heterochiral HSerAsn⁺ and HValAsn⁺ that have been assigned in the experimental IRMPD spectra are shaded in Table 3-1. It is interesting to note that all of them contain the most stable monomeric protonated species: HS1⁺, HV1⁺, and HA⁺. We note that the HS1⁺ identified here is also the most stable isomer reported in the previous IRMPD studies by Wu et al.¹⁷ and Sunahori et al.²³ HV1⁺ corresponds to the most stable configuration reported for the protonated monomer of valine methyl esters.⁵⁹ Two similar HA⁺ configurations are utilized the dimers and correspond to the two most stable protonated asparagine isomers reported by Heaton and co-workers⁶⁰ and by Heger et al;³⁵ their structures differ slightly depending on which carbonyl O lone pair is used in the intramolecular H-bond with the NH₃⁺ group.

The connection to the stability of the neutral monomeric species is less clear. For example, the observed Type I *S,S*-HSerAsn⁺ is made of HS1⁺/A1, where A1 (*cis*-COOH) has a very similar configuration as Ic, a higher energy isomer, reported in a previous jet microwave spectroscopic study.²⁹ The non-observed Type III *S,S*-HSerAsn⁺, on the other hand, is made of HS1⁺/A2 where A2 (*trans*-COOH) takes on a structure somewhere between II_a, the only one observed experimentally in a jet, and II_b, a much higher energy isomer.²⁹ The observed Type III structure of HSerAsn⁺ is made of S1/A⁺, where S1 has a structure somewhere between I_b and I'_b, two higher isomers of serine.²⁷ These observations are not too surprising because in a protonated dimer, the neutral subunit often opens up some of its intramolecular hydrogen bonds to accommodate strong intermolecular interactions with its protonated counterpart. It is noted that structural interconversions, for example, the proton migration which is discussed in section 3.3.5, may complicate the discussion of the formation of the gas-phase ions, although one would expect such processes to lead to more stable species. Overall, the abundance of the monomeric ZW and protonated subunits in the gas phase seems to play an important role in which dimer can be observed experimentally, rather than just the relative thermodynamic stability of the dimers.

To explore the possibility if any chirality recognition effects may be detected in some other frequency regions, the predicted IR spectra in the 0-2650 cm⁻¹ region of all the assigned structures, namely Type I and Type III structures of HSerAsn⁺ and Type I structures of HValAsn⁺, are depicted in Appendix A. The zoom-in spectra in the 1000-1900 cm⁻¹ region also are shown. The 1600-1700 cm⁻¹ region offers potentially the most noticeable different IR band features that are associated with the NH_x scissoring of the protonated NH₃⁺ and sidechain NH₂ functional groups, as well as the NH₃ umbrella bending motion.

Very recently, Andersson et al. reported minor differences in the IRMPD spectra of the homo- and heterochiral proton-bound asparagine dimer,⁶¹ similar to what we observe in terms of chirality effects in the IRMPD spectra of the four species discussed. Based on their experiment and also a related theoretical study,⁴³ the authors suggested that to observe chiral differences within the mid-IR region, sidechains must

be involved in the intermolecular interactions. For example, Type II *S,S*- and *R,S*-HSerAsn⁺ isomers have both sidechains of serine and asparagine involved in intermolecular interactions, and noticeable chiral effects, i.e., differences in the homo versus heterochiral IR spectra, are predicted. On the other hand, Type III structures have the least sidechain involvement in the intermolecular interactions, and their homo- and heterochiral IR spectra are more similar, showing least chiral effects. For the protonated asparagine dimers, the authors also suggested that dimers with limited interaction with the sidechain are favored energetically. This does not appear to apply to our current systems since the most favored binary species, based on the theoretical and experimental results, are Type I structures that have more or similar sidechain involvement as compared to the other Types of structures.

It is interesting to point out that the ZW types of HSerAsn⁺ and HValAsn⁺ are predicted to have a slight homochiral preference (see Figures 3-3 and 3-4), consistent with the homochiral preference trend reported in Ref. 26 where in a racemic mixture of serine or valine with excess *R*-asparagine, *R*-serine or *R*-valine preferentially co-crystallized, respectively. Since none of these ZW types were observed in the current experiment, to appreciate the role that chirality plays in the energy ordering, we carried out the non-covalent interaction (NCI⁶²) and quantum theory of atoms in molecules (QTAIM⁶³) analyses of the experimentally observed Type I binary homo- and heterochiral HSerAsn⁺ species. The NCI analyses are depicted in Figure 3-8. As one can see, the intermolecular hydrogen bonds are from the NH₃⁺ group of serine to the NH₂ and the O of the carbonyl group of asparagine in both homo- and heterochiral dimers, whereas serine has its carboxyl and the hydroxyl groups pointing away from asparagine. The NCI plots also show other intermolecular interactions besides the two hydrogen bonds mentioned above, more for *S,S*- than for *R,S*-HSerAsn⁺. To quantify the strength of the main hydrogen bonds, we also carried out a QTAIM analysis. The bond energies of the intermolecular N-H⁺···O interactions for the homo- and heterochiral HSerAsn⁺ are 44.7 kJ mol⁻¹ and 41.7 kJ mol⁻¹, respectively, very similar in strength. In contrast, the bond energies of the N-H⁺···N intermolecular hydrogen bonds for the homo- and heterochiral HSerAsn⁺ are 68.2 kJ mol⁻¹ and 57.5 kJ mol⁻¹,

respectively, $\sim 11 \text{ kJ mol}^{-1}$ smaller for $R,S\text{-HSerAsn}^+$ than for $S,S\text{-HSerAsn}^+$. It appears that constrained by its chirality, it is more difficult to optimize intermolecular interactions while it sustains/minimizes the attractive/repulsive intramolecular interactions simultaneously in $R,S\text{-}$ than in $S,S\text{-HSerAsn}^+$. Overall, a noticeable chirality recognition energy gap is present for $R,S\text{-}$ versus $S,S\text{-HSerAsn}^+$ at a value of 8.3 kJ mol^{-1} (ZPE corrected energy) and 2.3 kJ mol^{-1} (free energy) with the latter being more stable.

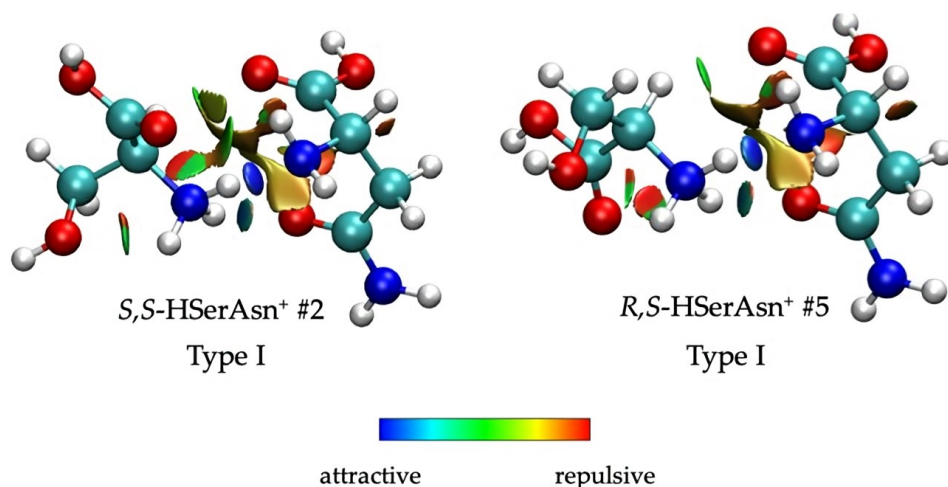


Figure 3-8. NCI plots of the most stable homo- and heterochiral HSerAsn⁺ at an iso-surface value of $s=0.5$.

For the case of Type I $S,S\text{-}$ and $R,S\text{-HValAsn}^+$, the NCI plots are provided in Figure 3-9. The corresponding QTAIM intermolecular $\text{N-H}^+\cdots\text{O}$ bond energies are 42.5 kJ mol^{-1} , 35.3 kJ mol^{-1} for the Type I $S,S\text{-}$ and $R,S\text{-HValAsn}^+$, respectively. For the $\text{N-H}^+\cdots\text{N}$ bond, these values are 70.3 kJ mol^{-1} and 65.3 kJ mol^{-1} for the Type I $S,S\text{-}$ and $R,S\text{-HValAsn}^+$, respectively. Overall, the chirality recognition energy is only about 1.7 kJ ml^{-1} (ZPE corrected energy) or 0.7 kJ mol^{-1} (free energy) in favour of the homochiral dimer. A plausible explanation is that valine has a non-polar sidechain that is less involved in non-covalent interactions, leading to less influence on chirality recognition. As a result, the chirality recognition energy of this system is relatively small by comparison to that of HSerAsn⁺.

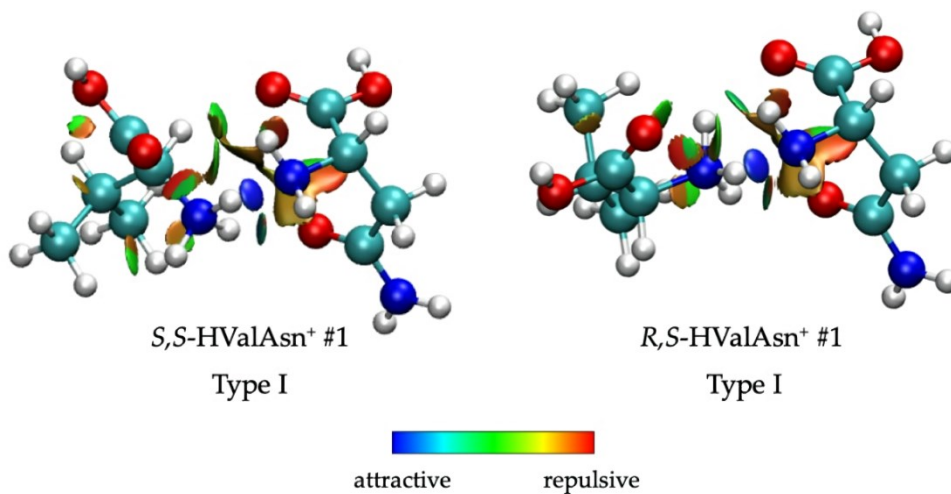


Figure 3-9. NCI plots of the most stable homo- and heterochiral HValAsn⁺ at an iso-surface value of $s=0.5$.

In comparison to the typical chirality recognition energies encountered in the neutral homo- and heterochiral dimers, for example, in those containing transient chiral subunits investigated using jet-cooled FTMW spectroscopy,^{64,65} the values predicted for the current series of homo- and heterochiral dimers are much larger. Certainly, the very high spectral resolution associated with jet-cooled FTMW spectroscopy provides a significant advantage in resolving possible conformers over the current IRMPD spectroscopy. If one can lower the experimental temperature to, for example 100 K, one would reduce the number of isomers populated and obtain a less crowded spectrum. At 100 K, one would expect only Type I, #2 for S,S -HSerAsn⁺ and Type I, #7 for R,S -HSerAsn⁺, based on both the thermodynamic and kinetic controlled process discussed, leading to more obvious differences between the homo- and heterochiral IR spectra. Indeed, a recent low temperature study of protonated glutamic acid dimers demonstrated that a cryogenic temperature approach could offer more clarity on chirality recognition spectral signature.⁶⁶

3.3.5 Fragmentation Channel

For all four species, their fragment mass spectra were dominated strongly by the protonated HAsn⁺ monomer at m/z 133, with minor contributions from smaller

fragments at m/z of 87 and 115 that were observed at specific irradiation wavenumbers. The observation is consistent with the expectation that these dimers can photodissociate into intact monomer units easily since their amino acid subunits are bound via weak non-covalent interactions, while any further “secondary” fragmentation of the monomers would require higher energies to overcome the dissociation threshold of covalent bonds. It is interesting to note that while the protonated HAsn^+ monomer peak at the m/z of 133 dominates the spectra, there is no sign of the corresponding HSer^+ or HVal^+ peaks at the m/z of 106 and 118. We further verified whether HSer^+ or HVal^+ experienced secondary fragmentation into even smaller pieces and found only smaller fragments at m/z of 87 and 115 which could be attributed to secondary fragmentation of HAsn^+ .^{35,67}

The detection of exclusively the HAsn^+ fragment ions for all four species was somewhat unexpected initially. The calculations suggest that the intact dimer structures generally prefer protonation on the serine or valine units, except for Type III HSerAsn^+ , where the proton prefers to stay with the asparagine subunit instead of serine. It is possible that the excess proton may migrate efficiently in the Type I structures from the serine/valine amino groups to the asparagine molecule during the photodissociation process. Two requirements are needed to achieve the above outcome: 1) the HAsn^+ fragment is more stable than HSer^+ or HVal^+ and 2) this proton migration happens with nearly complete efficiency. The thermodynamic aspect can be explained on the grounds that the Proton Affinity (PA) of asparagine ($\sim 940 \text{ kJ mol}^{-1}$) is higher than valine ($\sim 910 \text{ kJ mol}^{-1}$) and serine ($\sim 920 \text{ kJ mol}^{-1}$).^{68,69} In terms of the kinetic aspect of the proton migration, since the fragmentation process is highly energetic,⁷⁰ the proton may become loosely bonded between the two monomer subunits, largely free to migrate from one subunit to another. One can draw some comparison to proton mobility effects previously observed by Hopkins et al. in dimers of 3-cyanophenylalanine and trimethylamine, where irradiation of different vibrational bands in the fingerprint region led to different proton transfer patterns between the two dissociating fragments.⁷¹

3.4 Conclusions

In this project, we report the structural preferences for four homochiral and heterochiral HSerAsn⁺ and HValAsn⁺ complexes investigated using IRMPD spectroscopy, aided by a three-tiered computational approach that explores the conformational spaces of the four dimers systematically. The conformational space found for HSerAsn⁺ and HValAsn⁺ dimers are classified into Type I, II, III, and ZW, based on their binding topologies. The main species responsible for the experimentally observed IRMPD spectra are identified as Type I structures, where serine or valine form strong intermolecular hydrogen bonds from the NH₃⁺ group to the carbonyl O and NH₂ of asparagine, despite the fact that Type II structures of *R,S*-HSerAsn⁺ are predicted to be more stable than its Type I structure. This was explained based on a partially kinetically controlled dimer formation process, where the abundance of the protonated amino acid subunit plays a role in the final abundance of the corresponding dimer. We note that the protonated subunits in the observed dimers correspond to the most stable isomers of the isolated protonated amino acids detected experimentally in several previous IRMPD studies. A free energy gap of 2.3 kJ mol⁻¹ was predicted between the experimentally observed homo- and heterochiral HSerAsn⁺ dimers, while that value drops to 0.7 kJ mol⁻¹ between the observed *S,S*- and *R,S*-HValAsn⁺ dimers. The corresponding ZPE corrected energy gaps are 8.3 and 1.7 kJ mol⁻¹ for *S,S*- versus *R,S*-HSerAsn⁺ and *S,S*- versus *R,S*-HValAsn⁺, respectively, suggesting that a cryogenic experimental temperature may tease out the chirality recognition spectral signatures in these systems better.

3.5 Supplementary Data

Supplementary Data of Chapter 3, including details on PDY calculation, supporting tables, and figures, and cartesian coordinates of the corresponding isomers can be found in Appendix A

3.6 References

- ¹ Paezi, M.; Zamani, N.; Hassanian-Moghaddam, H.; Shadnia, S.; Zamani, N.; Chaleshi, V.; Mafi, A. A. Treatment of Adult Lead Poisoning with D-Penicillamine. *Drug Metab. Personal. Ther.* **2019**, *34*.
- ² Kajiwara, T. Effect of D-Penicillamine on Vitamin B6 and Collagen Metabolism (author's transl). *Nihon Seikeigeka Gakkai Zasshi.* **1979**, *53*, 1595–1605.
- ³ Lenz, W. Thalidomide and Congenital Abnormalities. *Lancet.* **1962**, *1*, 45-46.
- ⁴ Lenz, W. A Short History of Thalidomide Embryopathy. *Teratol.* **1988**, *38*, 203-215.
- ⁵ Brooks, W. H.; Guida, W. C.; Daniel, K. G. The Significance of Chirality in Drug Design and Development. *Curr. Top. Med. Chem.* **2011**, *11*, 760–770.
- ⁶ Zehnacker, A.; Suhm, M. A. Chirality Recognition between Neutral Molecules in the Gas Phase. *Angew. Chem. Int. Ed.* **2008**, *47*, 6970–6992.
- ⁷ Barron, L. D. *Molecular Light Scattering and Optical Activity*, Cambridge University Press, 2004.
- ⁸ Nafie, L. A. *Vibrational Optical Activity: Principles and Applications*, Wiley, 2011.
- ⁹ Hirata, K.; Mori, Y.; Ishiuchi, S.; Fujii, M.; Zehnacker, A. Chiral Discrimination between Tyrosine and β -Cyclodextrin Revealed by Cryogenic Ion Trap Infrared Spectroscopy. *Phys. Chem. Chem. Phys.* **2020**, *22*, 24887-24894.
- ¹⁰ Su, Z.; Borho, N.; Xu, Y. Chiral Self-Recognition: Direct Spectroscopic Detection of the Homochiral and Heterochiral Dimers of Propylene Oxide in the Gas Phase. *J. Am. Chem. Soc.* **2006**, *128*, 17126–17131.
- ¹¹ Xie, F.; Seifert, N. A.; Jäger, W.; Xu, Y. Conformational Panorama and Chirality Controlled Structure-Energy Relationship in a Chiral Carboxylic Acid Dimer. *Angew. Chem. Int. Ed.* **2020**, *59*, 15703-15710.
- ¹² Maris, A.; Giuliano, B. M.; Bonazzi, D.; Caminati, W. Molecular Recognition of Chiral Conformers: A Rotational Study of the Dimers of Glycidol. *J. Am. Chem. Soc.* **2008**, *130*, 13860-13861.
- ¹³ Brown, G. G.; Dian, B. C.; Douglass, K. O.; Geyer, S. M.; Shipman, S. T.; Pate, B. H. A Broadband Fourier transform Microwave Spectrometer Based on Chirped Pulse Excitation. *Rev. Sci. Instrum.* **2008**, *79*, 053103.

-
- ¹⁴ Pate, B. H.; Evangelisti, L.; Caminati, W.; Xu, Y.; Thomas, J.; Patterson, D.; Perez, C.; Schnell, M. Quantitative Chiral Analysis by Molecular Rotational Spectroscopy. In *Chiral Analysis, Advances in Spectroscopy, Chromatography and Emerging Methods*, Second Edition; ed. P. L. Polavarapu, Elsevier, 2018, pp 679-729. <https://doi.org/10.1016/B978-0-444-64027-7.00019-7>
- ¹⁵ Maitre, P.; Scuderi, D.; Corinti, D.; Chiavarino, B.; Crestoni, M. E.; Fornarini, S. Applications of Infrared Multiple Photon Dissociation (IRMPD) to the Detection of Posttranslational Modifications. *Chem. Rev.* **2020**, *120*, 3261–3295.
- ¹⁶ Polfer, N. C.; Oomens, J.; Dunbar, R. C. IRMPD Spectroscopy of Metal-Ion/Tryptophan Complexes. *Phys. Chem. Chem. Phys.* **2006**, *8*, 2744-2751.
- ¹⁷ Wu, R.; McMahon, T. B. An Investigation of Protonation Sites and Conformations of Protonated Amino Acids by IRMPD Spectroscopy. *ChemPhysChem* **2008**, *9*, 2826-2835.
- ¹⁸ Fales, B. S.; Fujamade, N. O.; Oomens, J.; Rodgers, M. T. Infrared Multiple Photon Dissociation Action Spectroscopy and Theoretical Studies of Triethyl Phosphate Complexes: Effect of Protonation and Sodium Cationization on Structure. *J. Am. Soc. Mass Spectrom.* **2011**, *22*, 1862-1871.
- ¹⁹ Andersson, Å.; Poline, M.; Kodambattil, M.; Rebrov, O.; Loire, E.; Maître, P.; Zhaunerchyk, V. Structure of Proton-Bound Methionine and Tryptophan Dimers in the Gas Phase Investigated with IRMPD Spectroscopy and Quantum Chemical Calculations. *J. Phys. Chem. A* **2020**, *124*, 2408–2415.
- ²⁰ Cooks, R. G.; Zhang, D.; Koch, K. J.; Gozzo, F. C.; Eberlin, M. N. Chiroselective Self-Directed Octamerization of Serine: Implications for Homochirogenesis. *Anal. Chem.* **2001**, *73*, 3646–3655.
- ²¹ Kong, X.; Tsai, I-A.; Sabu, S.; Han, C. –C.; Lee, Y. T.; Chang, H. –C.; Tu, S. –Y.; Kung, A. H.; Wu, C. –C. Progressive Stabilization of Zwitterionic Structure in [H(Ser)₂-8]⁺ Studied by Infrared Photodissociation Spectroscopy. *Angew. Chem. Int. Ed.* **2006**, *45*, 4130-4134.
- ²² Kong, X.; Lin, C.; Infusini, G.; Oh, H.-B.; Jiang, H.; Breuker, K.; Wu, C.-C.; Charkin, O. P.; Chang H.-C.; McLafferty, F. W. Numerous Isomers of Serine Octamer

Ions Characterized by Infrared Photodissociation Spectroscopy. *ChemPhysChem* **2009**, *10*, 2603–2606.

²³ Sunahori, F. X.; Yang, G.; Kitova, E. N.; Klassen, J. S.; Xu, Y. Chirality Recognition of the Protonated Serine Dimer and Octamer by Infrared Multiphoton Dissociation Spectroscopy. *Phys. Chem. Chem. Phys.* **2013**, *15*, 1873-1886.

²⁴ Ren, J.; Wang, Y. –Y.; Feng, R. –X.; Kong, X. –L. Investigation of L/D- Threonine Substituted L-Serine Octamer Ions by Mass Spectrometry and Infrared Photodissociation Spectroscopy. *Chinese Chemical Letters* **2017**, *28*, 537-540.

²⁵ Shi, Y.; Du, M.; Ren, J.; Zhang, K.; Xu, Y.; Kong, X. Application of Infrared Multiple Photon Dissociation (IRMPD) Spectroscopy in Chiral Analysis. *Molecules* **2020**, *25*, 5152.

²⁶ Kojo, S.; Uchino, H.; Yoshimura, M.; Tanaka, K. Racemic D, L-Asparagine Causes Enantiomeric Excess of Other Coexisting Racemic D,L- Amino Acids During Recrystallization: A Hypothesis Accounting for the Origin of L- Amino Acids in the Biosphere. *Chem. Commun.* **2004**, *19*, 2146-2147.

²⁷ Blanco, S.; Sanz, M. E.; López, J. C.; Alonso, J. L. Revealing the Multiple Structures of Serine. *PNAS* **2007**, *104*, 20183-20188.

²⁸ Lesarri, A.; Cocinero, E. J.; López, J. C.; Alonso, J. L. The Shape of Neutral Valine. *Angew. Chem. Int. Ed.* **2004**, *43*, 605-610

²⁹ Cabezas, C.; Varela, M.; Peña, I.; Mata, S.; Lopez, J. C.; Alonso, J. L. The Conformational Locking of Asparagine. *Chem. Commun.* **2012**, *48*, 5934–5936.

³⁰ Pracht, P.; Bohle, F.; Grimme, S. Automated Exploration of the Low-Energy Chemical Space with Fast Quantum Chemical Methods. *Phys. Chem. Chem. Phys.* **2020**, *22*, 7169-7192.

³¹ Werner, H.-J.; Knowles, P. J.; Knizia, G.; Manby, F. R.; Schütz, M.; Celani, P.; Györffy, W.; Kats, D.; Korona, T.; Lindh, R.; Mitrushenkov, A.; Rauhut, G.; Shamasundar, K. R.; Adler, T. B.; Amos, R. D.; Bernhardsson, A.; Berning, A.; Cooper, D. L.; Deegan, M. J. O.; Dobbyn, A. J.; Eckert, F.; Goll, E.; Hampel, C.; Hesselmann, A.; Hetzer, G.; Hrenar, T.; Jansen, G.; Köppl, C.; Liu, Y.; Lloyd, A. W.; Mata, R. A.; May, A. J.; McNicholas, S. J.; Meyer, W.; Mura, M. E.; Nicklass, A.; O'Neill, D. P.;

Palmieri, P.; Peng, D.; Pflüger, K.; Pitzer, R.; Reiher, M.; Shiozaki, T.; Stoll, H.; Stone, A. J.; Tarroni, R.; Thorsteinsson, T.; Wang, M. *MOLPRO, a package of ab initio programs*, version 2015.1, see www.molpro.net.

³² Werner, H.-J.; Knowles, P. J.; Knizia, G.; Manby, F. R.; Schütz, M. Molpro: A General-Purpose Quantum Chemistry Program Package. *Wiley Interdiscip. Rev. Comput. Mol. Sci.* **2012**, *2*, 242-253.

³³ Werner, H.-J.; Knowles, P. J.; Manby, F. R.; Black, J. A.; Doll, K.; Heßelmann, A.; Kats, K.; Köhn, A.; Korona, T.; Kreplin, D. A.; Ma, Q.; Miller, T. F. III; Mitrushchenkov, A.; Peterson, K. A.; Polyak, I.; Rauhut, G.; Sibae, M. *J. Chem. Phys.* **2020**, *152*, 144107.

³⁴ Frisch, M. J.; Trucks, G. W.; Schlegel, H. B.; Scuseria, G. E.; Robb, M. A.; Cheeseman, J. R.; Scalmani, G.; Barone, V.; Petersson, G. A.; Nakatsuji, H.; Li, X.; Caricato, M.; Marenich, A. V.; Bloino, J.; Janesko, B. G.; Gomperts, R.; Mennucci, B.; Hratchian, H. P.; Ortiz, J. V.; Izmaylov, A. F.; Sonnenberg, J. L.; Williams-Young, D.; Ding, F.; Lipparini, F.; Egidi, F.; Goings, J.; Peng, B.; Petrone, A.; Henderson, T.; Ranasinghe, D.; Zakrzewski, V. G.; Gao, J.; Rega, N.; Zheng, G.; Liang, W.; Hada, M.; Ehara, M.; Toyota, K.; Fukuda, R.; Hasegawa, J.; Ishida, M.; Nakajima, T.; Honda, Y.; Kitao, O.; Nakai, H.; Vreven, T.; Throssell, K.; Montgomery Jr., J. A.; Peralta, J. E.; Ogliaro, F.; Bearpark, M. J.; Heyd, J. J.; Brothers, E. N.; Kudin, K. N.; Staroverov, V. N.; Keith, T. A.; Kobayashi, R.; Normand, J.; Raghavachari, K.; Rendell, A. P.; Burant, J. C.; Iyengar, S. S.; Tomasi, J.; Cossi, M.; Millam, J. M.; Klene, M.; Adamo, C.; Cammi, R.; Ochterski, J. W.; Martin, R. L.; Morokuma, K.; Farkas, O.; Foresman, J. B.; Fox, D. J. *Gaussian 16*, Revision C.03; Gaussian, Inc.: Wallingford, CT, 2019.

³⁵ Heger, H.; Cheramy, J.; Xie, F.; Chen, Z.; Xu, Y. Structural and Energetic Properties of Protonated and Sodiated Asparagine Probed by A New Laboratory IRMPD Spectrometer. *J. Mol. Spectrosc.* **2018**, *352*, 36-44.

³⁶ Lehnig, R.; Jäger, W. Infrared Spectroscopy of the Antisymmetric Stretching Mode of 16OC18O in Helium Nanodroplets. *Chem. Phys. Lett.* **2006**, *424*, 146-150.

-
- ³⁷ Raston, P. L.; Knapp, C. J.; Jäger, W. Rotovibrational Spectroscopy of Hydrogen Peroxide Embedded in Superfluid Helium Nanodroplets. *Phys. Chem. Chem. Phys.* **2011**, *13*, 18789–18798.
- ³⁸ Prell, J. S.; O'Brien, J. T.; Williams, E. R. IRPD Spectroscopy and Ensemble Measurements: Effects of Different Data Acquisition and Analysis Methods. *J. Am. Soc. Mass Spectrom.* **2010**, *21*, 800-809.
- ³⁹ Seo, J.; Warnke, S.; Pagel, K.; Bowers, M. T.; von Helden, G. Infrared Spectrum and Structure of the Homochiral Serine Octamer-Dichloride Complex. *Nat Chem.* **2017**, *9*, 1263-1268.
- ⁴⁰ *MacroModel*, version 9.8; Schrödinger, LLC: New York, NY, 2010.
- ⁴¹ Aradi, B.; Hourahine, B.; Frauenheim, T. DFTB+, A Sparse Matrix-Based Implementation of the DFTB Method. *J. Phys. Chem. A* **2007**, *111*, 5678-5684.
- ⁴² Hourahine, B.; Aradi, B.; Blum, V. et al. DFTB+, A Software Package for Efficient Approximate Density Functional Theory Based Atomistic Simulations. *J. Chem. Phys.* **2020**, *152*, 124101.
- ⁴³ Poline, M.; Rebrov, O.; Larsson, M.; Zhaunerchyk, V. Theoretical Studies of Infrared Signatures of Proton-Bound Amino Acid Dimers with Homochiral and Heterochiral Moieties. *Chirality* **2020**, *32*, 359-369.
- ⁴⁴ Xie, F.; Seifert, N. A.; Heger, M.; Thomas, J.; Jäger, W.; Xu, Y. The Rich Conformational Landscape of Perillyl Alcohol Revealed by Broadband Rotational Spectroscopy and Theoretical Modelling. *Phys. Chem. Chem. Phys.* **2019**, *21*, 15408–15416.
- ⁴⁵ Xie, F.; Fusè, M.; Hazrah, A. S.; Jäger, W.; Barone, V.; Xu, Y. Discovering the Elusive Global Minimum in a Ternary Chiral Cluster: Rotational Spectra of Propylene Oxide Trimer. *Angew. Chem. Int. Ed.* **2020**, *59*, 22427-22430; *Angew. Chem.* **2020**, *132*, 22613-22616.
- ⁴⁶ Pracht, P.; Bauer, C. A.; Grimme, S. Automated and Efficient Quantum Chemical Determination and Energetic Ranking of Molecular Protonation Sites. *J. Comput. Chem.* **2017**, *38*, 2618–2631.

-
- ⁴⁷ Oswald, S.; Seifert, N. A.; Bohle, F.; Gawrilow, M.; Grimme, S.; Jäger, W.; Xu, Y.; Suhm, M. A. The Chiral Trimer and A Metastable Chiral Dimer of Achiral Hexafluoroisopropanol: A Multi-Messenger Study. *Angew. Chem. Int. Ed.* **2019**, *58*, 5080-5084; *Angew. Chem.* **2019**, *131*, 5134-5138.
- ⁴⁸ Seifert, N. A.; Thomas, J.; Jäger, W.; Xu, Y. Rotational Spectra and Theoretical Study of Tetramers and Trimers of 2-Fluoroethanol: Dramatic Intermolecular Compensation for Intramolecular Instability. *Phys. Chem. Chem. Phys.* **2018**, *20*, 27630-27637.
- ⁴⁹ Xie, F.; Ng, X.; Seifert, N. A.; Thomas, J.; Jäger, W.; Xu, Y. Rotational Spectroscopy of Chiral Tetrahydro-2-furoic Acid: Conformational Landscape, Conversion and Abundances. *J. Chem. Phys.* **2018**, *149*, 224306.
- ⁵⁰ Weigend, F.; Ahlrichs, R. Balanced Basis Sets of Split Valence, Triple Zeta Valence and Quadruple Zeta Valence Quality for H to Rn: Design and Assessment of Accuracy. *Phy. Chem. Chem. Phys.* **2005**, *7*, 3297.
- ⁵¹ Grimme, S.; Antony, J.; Ehrlich, S.; Krieg, H. A Consistent and Accurate *ab initio* Parametrization of Density Functional Dispersion Correction (DFT-D) for the 94 elements H-Pu. *J. Chem. Phys.* **2010**, *132*, 154104.
- ⁵² Grimme, S.; Ehrlich, D.; Goerigk, L. Effect of the Damping Function in Dispersion Corrected Density Functional Theory. *J. Comput. Chem.* **2011**, *32*, 1456-1465.
- ⁵³ Alonso, J. L.; López, J. C. Microwave Spectroscopy of Biomolecular Building Blocks. In *Gas-Phase IR Spectroscopy and Structure of Biological Molecules*, Vol. 364; Rijs, A. M.; Oomens, J., Ed.; 2015; pp 335–402.
- ⁵⁴ Miller, R. E. The Vibrational Spectroscopy and Dynamics of Weakly Bound Neutral Complexes. *Science* **1998**, *240*, 447-453.
- ⁵⁵ Juanes, M.; Saragi, R. T.; Caminati, W.; Lesarri, A., The Hydrogen Bond and Beyond: Perspectives for Rotational Investigations of Non-Covalent Interactions. *Chem. Eur. J.* **2019**, *25*, 11402-11411.
- ⁵⁶ Calabrese, C.; Uriarte, I.; Insausti, A.; Vallejo-López, M.; Basterretxea, F. J.; Cochrane, S. A.; Davis, B. G.; Corzana, F.; Cocinero, E. J. Observation of the Unbiased Conformers of Putative DNA-Scaffold Ribosugars. *ACS Cent. Sci.* **2020**, *6*, 293-303.

-
- ⁵⁷ Zhu, P.; Yang, G.; Poopari, M. R.; Bie, Z.; Xu, Y. Conformations of Serine in Aqueous Solutions as Revealed by Vibrational Circular Dichroism. *Chem. Phys. Chem.* **2012**, *13*, 1272-1281.
- ⁵⁸ Rak, J.; Skurski, P.; Simons, J.; Gutowski, M. Low-Energy Tautomers and Conformers of Neutral and Protonated Arginine. *J. Am. Chem. Soc.* **2001**, *123*, 11695-11707.
- ⁵⁹ Simon, A.; MacAleese, L.; Maître, P.; Lemaire, J.; McMahon, T. B. Fingerprint Vibrational Spectra of Protonated Methyl Esters of Amino Acids in the Gas Phase. *J. Am. Chem. Soc.* **2007**, *129*, 2829-2840.
- ⁶⁰ Heaton, A. L.; Bowman, V. N.; Oomens, J.; Steill, J. D.; Armentrout, P. B. Infrared Multiple Photon Dissociation Spectroscopy of Cationized Asparagine: Effects of Metal Cation Size on Gas-Phase Conformation. *J. Phys. Chem.* **2009**, *113*, 5519-5530.
- ⁶¹ Andersson, Å.; Poline, M.; Houthuijs, K. J.; van Outersterp, R. E.; Berden, G.; Oomens, J.; Zhaunerchyk, V. IRMPD Spectroscopy of Homo- and Heterochiral Asparagine Proton-Bound Dimers in the Gas Phase. *J. Phys. Chem. A* **2021**, *125*, 7449-7456.
- ⁶² Johnson, E. R.; Keinan, S.; Mori- Sánchez, P.; Contreras- Garcia, J.; Cohen, A. J.; Yang, W. Revealing Noncovalent Interactions. *J. Am. Chem. Soc.* **2010**, *132*, 6498-6506.
- ⁶³ Emamian, S.; Lu, T.; Kruse, H.; Emamian, H. Exploring Nature and Predicting Strength of Hydrogen Bonds: A Correlation Analysis Between Atoms-in-Molecules Descriptors, Binding Energies, and Energy Components of Symmetry-Adapted Perturbation Theory. *J. Comput. Chem.* **2019**, *40*, 2868-2881.
- ⁶⁴ Borho, N.; Xu, Y. Tailoring the Key in a Molecular Lock-and-Key Model System: The Propylene Oxide···2-Fluoroethanol Complex. *J. Am. Chem. Soc.* **2008**, *130*, 5916-5921.
- ⁶⁵ Thomas, J.; Jäger, W.; Xu, Y. Chirality Induction and Amplification in the 2, 2, 2-Trifluoroethanol··· Propylene Oxide Adduct. *Angew. Chem. Int. Ed.* **2014**, *53*, 7277-7280.

-
- ⁶⁶ Klyne, J.; Bouchet, A.; Ishiuchi, S. I.; Fujii, M.; Schneider, M.; Baldauf, C.; Dopfer, O. Probing Chirality Recognition of Protonated Glutamic Acid Dimers by Gas-Phase Vibrational Spectroscopy and First Principles Simulations. *Phys. Chem. Chem. Phys.* **2018**, *20*, 28452-28464.
- ⁶⁷ Heaton, A. L.; Armentrout, P. B. Thermodynamics and Mechanism of Protonated Asparagine Decomposition. *J. Am. Mass Spectrom.* **2009**, *20*, 852-866.
- ⁶⁸ Uddin, K. M.; Warburton, P. L.; Poirier, R. A. Comparisons of Computational and Experimental Thermochemical Properties of α -Amino Acids. *J. Phys. Chem. B* **2012**, *116*, 3220-3234.
- ⁶⁹ Bleiholder, C.; Suhar, S.; Paizs, B. Revising the Proton Affinity Scale of the Naturally Occurring Alpha-Amino Acids. *J. Am. Soc. Mass Spectrom.* **2006**, *17*, 1275-1281.
- ⁷⁰ Lin, C.; Shishido, R.; Huang, Q.; Fujii, A.; Kuo, J. Vibrational Spectroscopy of Protonated Amine-Water Clusters: Tuning Fermi Resonance and Lighting up Dark States. *Phys. Chem. Chem. Phys.* **2020**, *22*, 22035-22046.
- ⁷¹ Hopkins, W. S.; Marta, R. A.; McMahon, T. B. Proton-Bound 3-Cyanophenylalanine Trimethylamine Clusters: Isomer-Specific Fragmentation Pathways and Evidence of Gas-Phase Zwitterions. *J. Phys. Chem. A* **2013**, *117*, 10714-10718.

CHAPTER 4

Conclusion and Future Applications

This thesis begins by introducing the idea and importance of chirality and chirality recognition, along with a powerful spectroscopic method, i.e., IRMPD spectroscopy, to perform these types of studies. Previous chirality studies using other spectroscopic methods are also briefly summarized.

Following the introduction, a breakdown of the IRMPD instrumentation that we implemented in our lab and the associated experimental details are described in Chapter 2. The information of how each part functions and the fundamental theory of IRMPD spectroscopy is also discussed in this chapter.

In Chapter 3, studies of the proton bound serine-asparagine and valine-asparagine dimers in both homochiral and heterochiral forms were carried out. A three-tiered computational approach was used to explore the conformational spaces for the four dimer species in a systemic way. The conformational spaces found for HSerAsn⁺ and HValAsn⁺ are classified based on their binding topologies. Theoretically predicted spectra were compared with the experimental IRMPD spectra recorded as a function of fragmentation with respect to laser frequencies in the 2600-3800 cm⁻¹ region. The identified most stable Type I structure is found where serine or valine form strong intermolecular hydrogen bonds from the NH₃⁺ group to the carbonyl O and NH₂ of asparagine. NCI and QTAIM analyses were carried out to gain further insight into the intermolecular interactions. A free energy gap between the observed homo- and heterochiral binary complexes of 2.3 kJ mol⁻¹ (HSerAsn⁺) and 0.7 kJ mol⁻¹ (HValAsn⁺) is evaluated. Although the IRMPD spectra observed for the homochiral and heterochiral dimers appear very similar in the current study, it is anticipated that a lower experimental temperature would lead to observable chirality recognition spectral signatures, i.e., different IR spectra for the homo- versus heterochiral dimers. IR spectra were also predicted in the lower wavenumber region which reveal some chirality recognition spectral signatures in the 1500-1700 cm⁻¹ region.

As for future work, it would be highly desirable to investigate our amino acid dimer systems using the HENDI “arm” of our instrumentation.¹ Based on our analysis, a cryogenic experimental temperature will allow one to tease out the chirality recognition spectral signatures in these systems. One drawback of doing IRMPD spectroscopy is the spectral broadening due to the thermal activation of ions during the sequential absorption of multiple photons. This leads to the congestion of some important peaks, making our IRMPD spectra less resolved. By using HENDI,^{2,3} the low equilibrium temperature of helium droplets at 0.37 K, maintained by evaporative cooling results in the absence of the thermal contributions; this enables the acquisition of IR spectra that are little affected by line broadening. Then, the obtained IR spectra can be used to compare with our room temperature IRMPD spectra to gain more insight into structural information and chirality preferences of our molecular systems. It would also be interesting to obtain IRMPD spectra in the lower wavenumber region ($< 2000 \text{ cm}^{-1}$) where we predicted some chirality recognition spectral features which may be detectable.

4.1 References

¹ Herger, M.; Cheramy, J.; Xie, F.; Chen, Z.; Xu, Y. Structural and Energetic Properties of Protonated and Sodiated Asparagine Probed by a New Laboratory IRMPD Spectrometer. *J. Mol. Spectrosc.* **2018**, *352*, 36-44.

² Raston, P. L.; Knapp, C. J.; Jäger, W. Rotovibrational Spectroscopy of Hydrogen Peroxide Embedded in Superfluid Helium Nanodroplets. *Phys. Chem. Chem. Phys.* **2011**, *13*, 18789-18798.

³ Das, P.; Knapp, C. J.; Jäger, W. Ro-Vibrational Spectroscopy of the Formic Acid-*d*₁ Monomer Embedded in Helium Nanodroplets. *J. Mol. Spectrosc.* **2017**, *341*, 17-22.

Bibliography

- ¹ Kim, J. H.; Scialli, A. R. Thalidomide: The Tragedy of Birth Defects and the Effective Treatment of Disease. *Toxicol Sci.* **2011**, *122*, 1-6.
- ² Lenz, W. Thalidomide and Congenital Abnormalities. *Lancet.* **1962**, *1*, 45-46.
- ³ Lenz, W. A Short History of Thalidomide Embryopathy. *Teratol.* **1988**, *38*, 203-215.
- ⁴ Eriksson, T.; Björkman, S.; Roth, B.; Fyge, A.; Höglund, P. Stereospecific Determination, Chiral Inversion in Vitro and Pharmacokinetics in Humans of the Enantiomers of Thalidomide. *Chirality* **1995**, *7*, 44-52.
- ⁵ Yang, G.; Xu, Y. Vibrational Circular Dichroism Spectroscopy of Chiral Molecules. *Top. Curr. Chem.* **2011**, *298*, 189-236.
- ⁶ Merten, C.; Hiller, K.; Xu, Y. Effects of Electron Configuration and Coordination Number on the Vibrational Circular Dichroism Spectra of Metal Complexes of *Trans*-1,2-Diaminocyclohexane. *Phys. Chem. Chem. Phys.* **2012**, *14*, 12884-12891.
- ⁷ Wu, T.; Li, G.; Kapitán, J.; Kessler, J.; Xu, Y.; Bouř, P. Two Spectroscopies in One: Interference of Circular Dichroism and Raman Optical Activity. *Angew. Chem. Int. Ed.* **2020**, *59*, 21895-21898.
- ⁸ Zhang, Y.; Poopari, M. R.; Cai, X.; Savin, A.; Dezhahang, Z.; Cheramy, J.; Xu, Y. IR and Vibrational Circular Dichroism Spectroscopy of Matrine- and Artemisinin-Type Herbal Products: Stereochemical Characterization and Solvent Effects. *J. Nat. Prod.* **2016**, *79*, 1012-1023.
- ⁹ Poopari, M. R.; Dezhahang, Z.; Xu, Y. A Comparative VCD Study of Methyl Mandelate in Methanol, Dimethyl Sulfoxide, and Chloroform: Explicit and Implicit Solvation Models. *Phys. Chem. Chem. Phys.* **2013**, *15*, 1655-1665.
- ¹⁰ Perera, A. S.; Thomas, J.; Poopari, M. R.; Xu, Y. The Clusters-in-a-Liquid Approach for Solvation: New Insights from the Conformer Specific Gas Phase Spectroscopy and Vibrational Optical Activity Spectroscopy. *Frontiers in Chemistry* **2016**, *4*, 9.
- ¹¹ Thomas, J.; Sukhorukov, O.; Jäger, W.; Xu, Y. Chirped-Pulse and Cavity-Based Fourier Transform Microwave Spectra of the Methyl Lactate...Ammonia Adduct: Lock and Key Selectivity and Internal Rotation Motions. *Angew. Chem. Int. Ed.* **2013**, *52*, 4402-4405.

- ¹² Thomas, J.; Seifert, N. A.; Jäger, W.; Xu, Y. A Direct Link from the Gas to the Condensed Phase: A Rotational Spectroscopic Study of 2,2,2-Trifluoroethanol Trimers. *Angew. Chem. Int. Ed.* **2017**, *56*, 6289-6293.
- ¹³ Thomas, J.; Liu, X.; Jäger, W.; Xu, Y. Unusual H-bond Topology and Bifurcated H-bonds in the 2-Fluoroethanol Trimer. *Angew. Chem. Int. Ed.* **2015**, *54*, 11711-11715.
- ¹⁴ Seifert, N. A.; Thomas, J.; Jäger, W.; Xu, Y. Rotational Spectra and Theoretical Study of Tetramers and Trimers of 2-Fluoroethanol: Dramatic Intermolecular Compensation for Intramolecular Instability. *Phys. Chem. Chem. Phys.* **2018**, *20*, 27630-27637.
- ¹⁵ Su, Z.; Borho, N.; Xu, Y. Chiral Self-Recognition: Direct Spectroscopic Detection of the Homochiral and Heterochiral Dimers of Propylene Oxide in the Gas Phase. *J. Am. Chem. Soc.* **2006**, *128*, 17126-17131.
- ¹⁶ Borho, N.; Xu, Y. Tailoring the Key in a Molecular Lock-and-Key Model System: The Propylene Oxide...2-Fluoroethanol Complex. *J. Am. Chem. Soc.* **2008**, *130*, 5916-5921.
- ¹⁷ Borho, N.; Xu, Y. Lock-and-Key Principle on a Microscopic Scale: The Case of the Propylene Oxide...Ethanol Complex. *Angew. Chem. Int. Ed.* **2007**, *46*, 2276-2279.
- ¹⁸ Xie, F.; Fusè, M.; Hazrah, A. S.; Jäger, W.; Barone, V.; Xu, Y. Discovering the Elusive Global Minimum in a Ternary Chiral Cluster: Rotational Spectra of Propylene Oxide Trimer. *Angew. Chem. Int. Ed.* **2020**, *59*, 22427-22430.
- ¹⁹ Xie, F.; Seifert, N. A.; Jäger, W.; Xu, Y. Conformational Panorama and Chirality Controlled Structure-Energy Relationship in a Chiral Carboxylic Acid Dimer. *Angew. Chem. Int. Ed.* **2020**, *59*, 15703-15710.
- ²⁰ Pate, B. H.; Evangelisti, L.; Caminati, W.; Xu, Y.; Thomas, J.; Patterson, D.; Perez, C.; Schnell, M. Quantitative Chiral Analysis by Molecular Rotational Spectroscopy. In *Chiral Analysis: Advances in Spectroscopy, Chromatography and Emerging Methods*, 2nd ed.; Elsevier, 2018, pp 679-729.
- ²¹ Domingos, S. R.; Pérez, C.; Marshall, M. D.; Leung, H. O.; Schnell, M. Assessing the performance of Rotational Spectroscopy in Chiral Analysis. *Chem. Sci.* **2020**, *11*, 10863-10870.

- ²² Medel, R.; Stelbrink, C.; Suhm, M. A. Vibrational Signatures of Chirality Recognition Between α -Piene and Alcohols for Theory Benchmarking. *Angew. Chem. Int. Ed.* **2019**, *58*, 8177-8181.
- ²³ Zehnacker, A.; Suhm, M. A. Chirality Recognition between Neutral Molecules in the gas phase. *Angew. Chem. Int. Ed.* **2008**, *47*, 6970-6992.
- ²⁴ Chai, H.; Chen, Z.; Wang, S.; Quan, M.; Yang, L.; Ke, H.; Jiang, W. Enantioselective Recognition of Neutral Molecules in Water by a Pair of Chiral Biomimetic Macrocyclic Receptors. *CCS Chem.* **2020**, *2*, 440-452.
- ²⁵ Polfer, N. C. Infrared Multiple Photon Dissociation Spectroscopy of Trapped Ions. *Chem. Soc. Rev.* **2011**, *40*, 2211-2221.
- ²⁶ Rajabi, K.; Fridgen, T. D. Structure of Aliphatic Amino Acid Proton-Bound Dimers by Infrared Multiple Photon Dissociation Spectroscopy in the 700-2000 cm^{-1} Region. *J. Phys. Chem. A* **2008**, *112*, 23-30.
- ²⁷ Feng, R.; Yin, H.; Kong, X. Structure of Protonated Tryptophan Dimer in the Gas Phase Investigated by IRPD Spectroscopy and Theoretical Calculations. *Rapid Commun. Mass Spectrom.* **2016**, *30*, 24-28.
- ²⁸ Poline, M.; Rebrov, O.; Larsson, M.; Zhaunerchyk, V. Theoretical Studies of Infrared Signatures of Proton-Bound Amino Acid Dimers with Homochiral and Heterochiral Moieties. *Chirality* **2020**, *32*, 359-369.
- ²⁹ Scuderi, D.; Correia, C. F.; Balaj, O. P.; Ohanessian, G.; Lemaire, J.; Maitre, P. Structural Characterization by IRMPD Spectroscopy and DFT Calculations of Deprotonated Phosphorylated Amino Acids in the Gas Phase. *ChemPhysChem* **2009**, *10*, 1630-1641.
- ³⁰ Tan, Y.; Zhao, N.; Liu, J.; Li, P.; Stedwell, C. N.; Yu, L.; Polfer, N. C. Vibrational Signatures of Isomeric Lithiated N-acetyl-D-hexosamines by Gas-Phase Infrared Multiple-Photon Dissociation (IRMPD) Spectroscopy. *J. Am. Soc. Mass Spectrom.* **2017**, *28*, 539-550.
- ³¹ Fales, B. S.; Fujamade, N. O.; Oomens, J.; Rodgers, M. T. Infrared Multiple Photon Dissociation Action Spectroscopy and Theoretical Studies of Triethyl Phosphate

Complexes: Effects of Protonation and Sodium Cationization on Structure. *J. Am. Soc. Mass Spectrom.* **2011**, *22*, 1862-1871.

³² Polfer, N. C.; Oomens, J.; Dunbar, R. C. IRMPD Spectroscopy of Metal-Ion/Tryptophan Complexes. *Phys. Chem. Chem. Phys.* **2006**, *8*, 2744-2751.

³³ Yang, Y.; Liao, G.; Kong, X. Charge-state Resolved Infrared Multiple Photon Dissociation (IRMPD) Spectroscopy of Ubiquitin Ions in the Gas Phase. *Sci. Rep.* **2017**, *7*, 16592.

³⁴ Schug, K. A.; Lindner, W. Chiral Molecular Recognition for the Detection and Analysis of Enantiomers by Mass Spectrometric Methods. *J. Sep. Sci.* **2005**, *28*, 1932-1955.

³⁵ Han, D. -Q.; Yao, Z. -P. Chiral Mass Spectrometry: An Overview. *TrAC Trends Anal. Chem.* **2020**, *123*, 115763.

³⁶ Dwivedi, P.; Wu, C.; Matz, L. M.; Clowers, B. H.; Seims, W. F.; Hill, H. H. Jr. Gas-Phase Chiral separations by Ion Mobility Spectrometry. *Anal. Chem.* **2006**, *78*, 8200-8206.

³⁷ Sunahori, F. X.; Yang, G.; Kitova, E. N.; Klassen, J. S.; Xu, Y. Chirality Recognition of the Protonated Serine Dimer and Octamer by Infrared Multiphoton Dissociation Spectroscopy. *Phys. Chem. Chem. Phys.* **2013**, *15*, 1873-1886.

³⁸ Lepere, V.; Barbu-Debus, K. L.; Clavaguéra, C.; Scuderi, D.; Piani, G.; Simon, A. -L.; Chirot, R.; MacAleese, L.; Dugourd, P.; Zehnacker, A. Chirality-Dependent Structuration of Protonated or Sodiated Polyphenylalanines: IRMPD and Ion Mobility Studies. *Phys. Chem. Chem. Phys.* **2016**, *18*, 1807-1817.

³⁹ Cheng, R.; Loire, E.; Martens, J.; Fridgen, T. D. An IRMPD Spectroscopic and Computational Study of Protonated Guanine-Containing Mismatched Base Pairs in the Gas Phase. *Phys. Chem. Chem. Phys.* **2020**, *22*, 2999-3007.

⁴⁰ Podlech, J. Origin of Organic Molecules and Biomolecular Homochirality. *Cell. Mol. Life Sci.* **2001**, *58*, 44-60.

⁴¹ Cooks, R. G.; Zhang, D.; Koch, K. J.; Gozzo, F. C.; Eberlin, M. N. Chiroselective Self-Directed Octamerization of Serine: Implications for Homochirogenesis. *Anal. Chem.* **2001**, *73*, 3646-3655.

- ⁴² Kong, X.; Lin, C.; Infusini, G.; Oh, H. -B.; Jiang, H.; Breuker, K.; Wu, C. -C.; Charkin, O. P.; Chang, H. -C.; McLafferty, F. W. Numerous Isomers of Serine Octamer Ions Characterized by Infrared Photodissociation Spectroscopy. *ChemPhysChem* **2009**, *10*, 2603-2606.
- ⁴³ Raston, P. L.; Knapp, C. J.; Jäger, W. Rotovibrational Spectroscopy of Hydrogen Peroxide Embedded in Superfluid Helium Nanodroplets. *Phys. Chem. Chem. Phys.* **2011**, *13*, 18789-18798.
- ⁴⁴ Das, P.; Knapp, C. J.; Jäger, W. Ro-Vibrational Spectroscopy of the Formic Acid-*d*₁ Monomer Embedded in Helium Nanodroplets. *J. Mol. Spectrosc.* **2017**, *341*, 17-22.
- ⁴⁵ Herger, M.; Cheramy, J.; Xie, F.; Chen, Z.; Xu, Y. Structural and Energetic Properties of Protonated and Sodiated Asparagine Probed by a New Laboratory IRMPD Spectrometer. *J. Mol. Spectrosc.* **2018**, *352*, 36-44.
- ⁴⁶ Lehmann, K. K.; Scoles, G.; Pate, B. H. Intramolecular Dynamics from Eigenstate-Resolved Infrared Spectra. *Annu. Rev. Phys. Chem.* **1994**, *45*, 241-274.
- ⁴⁷ Nesbitt, D. J.; Field, R. W. Vibrational Energy Flow in Highly Excited Molecules: Role of Intramolecular Vibrational Redistribution. *J. Phys. Chem.* **1996**, *100*, 12735-12756.
- ⁴⁸ Heger, M. SCORPION User Handbook. **2021**.
- ⁴⁹ Kelly, R. T.; Page, J. S.; Luo, Q.; Moore, R. J.; Orton, D. J.; Tang, K.; Smith, R. D. Chemically Etched Open Tubular and Monolithic Emitters for Nanoelectrospray Ionization Mass Spectrometry. *Anal. Chem.* **2006**, *78*, 7796-7801.
- ⁵⁰ Finlayson-Pitts, B. J.; Pitts Jr., J. N. Analytical Methods and Typical Atmospheric Concentrations for Gases and Particles. In *Chemistry of the Upper and Lower Atmosphere*; Academic Press, 2000; pp 547-656.
- ⁵¹ Kicman, A. T.; Parkin, M. C.; Iles, R. K. An Introduction to Mass Spectrometry Based Proteomics- Detection and Characterization of Gonadotropins and Related Molecules. *Mol. Cell. Endocrinol.* **2007**, *260-262*:212-227.
- ⁵² Miller, P. E.; Denton, M. B. The Transmission Properties of an RF-Only Quadrupole Mass Filter Mass Filter. *Int. J. Mol. Sci.* **1986**, *72*, 223-238.

- ⁵³ Pedder, R. E. Practical Quadrupole Theory: Graphical Theory. *Extrel Application Note RA_2010A*.
- ⁵⁴ Pedder, R. E. Practical Quadrupole Theory: Peak Shapes at Various Ion Energies. *Extrel Application Note RA_2011A*.
- ⁵⁵ Somogyi, Á. Mass Spectrometry Instrumentation and Techniques. In *Medical Applications of Mass Spectrometry*; Elsevier, 2008; pp 93-140.
- ⁵⁶ Page, J. S.; Tang, K.; Kelly, R. T.; Smith, R. D. A Subambient Pressure Ionization with Nanoelectrospray (SPIN) Source and Interface for Improved Sensitivity in Mass Spectrometry. *Anal. Chem.* **2008**, *80*, 1800-1805.
- ⁵⁷ Cox, J. T.; Kronewitter, S. R.; Shukla, A. K.; Moore, R. J.; Smith, R. D.; Tang, K. High Sensitivity Combined with Extended Structural Coverage of Labile Compounds via Nanoelectrospray Ionization at Subambient Pressures. *Anal. Chem.* **2014**, *86*, 9504-9511.
- ⁵⁸ Heger, M. SCORPION SOP: Hydrofluoric Acid Etching of Tapered-Tip ESI Emitters. **2021**.
- ⁵⁹ Paezi, M.; Zamani, N.; Hassanian-Moghaddam, H.; Shadnia, S.; Zamani, N.; Chaleshi, V.; Mafi, A. A. Treatment of Adult Lead Poisoning with D-Penicillamine. *Drug Metab. Personal. Ther.* **2019**, *34*.
- ⁶⁰ Kajiwara, T. Effect of D-Penicillamine on Vitamin B6 and Collagen Metabolism (author's transl). *Nihon Seikeigeka Gakkai Zasshi.* **1979**, *53*, 1595-1605.
- ⁶¹ Brooks, W. H.; Guida, W. C.; Daniel, K. G. The Significance of Chirality in Drug Design and Development. *Curr. Top. Med. Chem.* **2011**, *11*, 760-770.
- ⁶² Barron, L. D. *Molecular Light Scattering and Optical Activity*, Cambridge University Press, 2004.
- ⁶³ Nafie, L. A. *Vibrational Optical Activity: Principles and Applications*, Wiley, 2011.
- ⁶⁴ Hirata, K.; Mori, Y.; Ishiuchi, S.; Fujii, M.; Zehnacker, A. Chiral Discrimination between Tyrosine and β -Cyclodextrin Revealed by Cryogenic Ion Trap Infrared Spectroscopy. *Phys. Chem. Chem. Phys.* **2020**, *22*, 24887-24894.

- ⁶⁵ Maris, A.; Giuliano, B. M.; Bonazzi, D.; Caminati, W. Molecular Recognition of Chiral Conformers: A Rotational Study of the Dimers of Glycidol. *J. Am. Chem. Soc.* **2008**, *130*, 13860-13861.
- ⁶⁶ Brown, G. G.; Dian, B. C.; Douglass, K. O.; Geyer, S. M.; Shipman, S. T.; Pate, B. H. A Broadband Fourier transform Microwave Spectrometer Based on Chirped Pulse Excitation. *Rev. Sci. Instrum.* **2008**, *79*, 053103.
- ⁶⁷ Maitre, P.; Scuderi, D.; Corinti, D.; Chiavarino, B.; Crestoni, M. E.; Fornarini, S. Applications of Infrared Multiple Photon Dissociation (IRMPD) to the Detection of Posttranslational Modifications. *Chem. Rev.* **2020**, *120*, 3261–3295.
- ⁶⁸ Wu, R.; McMahon, T. B. An Investigation of Protonation Sites and Conformations of Protonated Amino Acids by IRMPD Spectroscopy. *ChemPhysChem* **2008**, *9*, 2826-2835.
- ⁶⁹ Andersson, Å.; Poline, M.; Kodambattil, M.; Rebroy, O.; Loire, E.; Maître, P.; Zhaunerchyk, V. Structure of Proton-Bound Methionine and Tryptophan Dimers in the Gas Phase Investigated with IRMPD Spectroscopy and Quantum Chemical Calculations. *J. Phys. Chem. A* **2020**, *124*, 2408–2415.
- ⁷⁰ Kong, X.; Tsai, I-A.; Sabu, S.; Han, C. -C.; Lee, Y. T.; Chang, H. -C.; Tu, S. -Y.; Kung, A. H.; Wu, C. -C. Progressive Stabilization of Zwitterionic Structure in [H(Ser)₂-8]⁺ Studied by Infrared Photodissociation Spectroscopy. *Angew. Chem. Int. Ed.* **2006**, *45*, 4130-4134.
- ⁷¹ Ren, J.; Wang, Y. -Y.; Feng, R. -X.; Kong, X. -L. Investigation of L/D- Threonine Substituted L-Serine Octamer Ions by Mass Spectrometry and Infrared Photodissociation Spectroscopy. *Chinese Chemical Letters* **2017**, *28*, 537-540.
- ⁷² Shi, Y.; Du, M.; Ren, J.; Zhang, K.; Xu, Y.; Kong, X. Application of Infrared Multiple Photon Dissociation (IRMPD) Spectroscopy in Chiral Analysis. *Molecules* **2020**, *25*, 5152.
- ⁷³ Nugrahani, I.; Jessica, M. A. Amino Acids as the Potential Co-Former for Co-Crystal Development: A Review. *Molecules* **2021**, *26*, 3279.
- ⁷⁴ Kojo, S.; Uchino, H.; Yoshimura, M.; Tanaka, K. Racemic D, L-Asparagine Causes Enantiomeric Excess of Other Coexisting Racemic D,L- Amino Acids During

Recrystallization: A Hypothesis Accounting for the Origin of L- Amino Acids in the Biosphere. *Chem. Commun.* **2004**, *19*, 2146-2147.

⁷⁵ Blanco, S.; Sanz, M. E.; López, J. C.; Alonso, J. L. Revealing the Multiple Structures of Serine. *PNAS* **2007**, *104*, 20183-20188.

⁷⁶ Lesarri, A.; Cocinero, E. J.; López, J. C.; Alonso, J. L. The Shape of Neutral Valine. *Angew. Chem. Int. Ed.* **2004**, *43*, 605-610

⁷⁷ Cabezas, C.; Varela, M.; Peña, I.; Mata, S.; Lopez, J. C.; Alonso, J. L. The Conformational Locking of Asparagine. *Chem. Commun.* **2012**, *48*, 5934–5936.

⁷⁸ Pracht, P.; Bohle, F.; Grimme, S. Automated Exploration of the Low-Energy Chemical Space with Fast Quantum Chemical Methods. *Phys. Chem. Chem. Phys.* **2020**, *22*, 7169-7192.

⁷⁹ Werner, H.-J.; Knowles, P. J.; Knizia, G.; Manby, F. R.; Schütz, M.; Celani, P.; Györffy, W.; Kats, D.; Korona, T.; Lindh, R.; Mitrushenkov, A.; Rauhut, G.; Shamasundar, K. R.; Adler, T. B.; Amos, R. D.; Bernhardsson, A.; Berning, A.; Cooper, D. L.; Deegan, M. J. O.; Dobbyn, A. J.; Eckert, F.; Goll, E.; Hampel, C.; Hesselmann, A.; Hetzer, G.; Hrenar, T.; Jansen, G.; Köppl, C.; Liu, Y.; Lloyd, A. W.; Mata, R. A.; May, A. J.; McNicholas, S. J.; Meyer, W.; Mura, M. E.; Nicklass, A.; O'Neill, D. P.; Palmieri, P.; Peng, D.; Pflüger, K.; Pitzer, R.; Reiher, M.; Shiozaki, T.; Stoll, H.; Stone, A. J.; Tarroni, R.; Thorsteinsson, T.; Wang, M. *MOLPRO, a package of ab initio programs*, version 2015.1, see www.molpro.net.

⁸⁰ Werner, H.-J.; Knowles, P. J.; Knizia, G.; Manby, F. R.; Schütz, M. Molpro: A General-Purpose Quantum Chemistry Program Package. *Wiley Interdiscip. Rev. Comput. Mol. Sci.* **2012**, *2*, 242-253.

⁸¹ Werner, H.-J.; Knowles, P. J.; Manby, F. R.; Black, J. A.; Doll, K.; Heßelmann, A.; Kats, K.; Köhn, A.; Korona, T.; Kreplin, D. A.; Ma, Q.; Miller, T. F. III; Mitrushchenkov, A.; Peterson, K. A.; Polyak, I.; Rauhut, G.; Sibae, M. *J. Chem. Phys.* **2020**, *152*, 144107.

⁸² Frisch, M. J.; Trucks, G. W.; Schlegel, H. B.; Scuseria, G. E.; Robb, M. A.; Cheeseman, J. R.; Scalmani, G.; Barone, V.; Petersson, G. A.; Nakatsuji, H.; Li, X.; Caricato, M.; Marenich, A. V.; Bloino, J.; Janesko, B. G.; Gomperts, R.; Mennucci, B.;

Hratchian, H. P.; Ortiz, J. V.; Izmaylov, A. F.; Sonnenberg, J. L.; Williams-Young, D.; Ding, F.; Lipparini, F.; Egidi, F.; Goings, J.; Peng, B.; Petrone, A.; Henderson, T.; Ranasinghe, D.; Zakrzewski, V. G.; Gao, J.; Rega, N.; Zheng, G.; Liang, W.; Hada, M.; Ehara, M.; Toyota, K.; Fukuda, R.; Hasegawa, J.; Ishida, M.; Nakajima, T.; Honda, Y.; Kitao, O.; Nakai, H.; Vreven, T.; Throssell, K.; Montgomery Jr., J. A.; Peralta, J. E.; Ogliaro, F.; Bearpark, M. J.; Heyd, J. J.; Brothers, E. N.; Kudin, K. N.; Staroverov, V. N.; Keith, T. A.; Kobayashi, R.; Normand, J.; Raghavachari, K.; Rendell, A. P.; Burant, J. C.; Iyengar, S. S.; Tomasi, J.; Cossi, M.; Millam, J. M.; Klene, M.; Adamo, C.; Cammi, R.; Ochterski, J. W.; Martin, R. L.; Morokuma, K.; Farkas, O.; Foresman, J. B.; Fox, D. J. *Gaussian 16*, Revision C.03; Gaussian, Inc.: Wallingford, CT, 2019.

⁸³ Lehnig, R.; Jäger, W. Infrared Spectroscopy of the Antisymmetric Stretching Mode of 16OC18O in Helium Nanodroplets. *Chem. Phys. Lett.* **2006**, *424*, 146-150.

⁸⁴ Prell, J. S.; O'Brien, J. T.; Williams, E. R. IRPD Spectroscopy and Ensemble Measurements: Effects of Different Data Acquisition and Analysis Methods. *J. Am. Soc. Mass Spectrom.* **2010**, *21*, 800-809.

⁸⁵ Seo, J.; Warnke, S.; Pagel, K.; Bowers, M. T.; von Helden, G. Infrared Spectrum and Structure of the Homochiral Serine Octamer-Dichloride Complex. *Nat Chem.* **2017**, *9*, 1263-1268.

⁸⁶ *MacroModel*, version 9.8; Schrödinger, LLC: New York, NY, 2010.

⁸⁷ Aradi, B.; Hourahine, B.; Frauenheim, T. DFTB+, A Sparse Matrix-Based Implementation of the DFTB Method. *J. Phys. Chem. A* **2007**, *111*, 5678-5684.

⁸⁸ Hourahine, B.; Aradi, B.; Blum, V. et al. DFTB+, A Software Package for Efficient Approximate Density Functional Theory Based Atomistic Simulations. *J. Chem. Phys.* **2020**, *152*, 124101.

⁸⁹ Xie, F.; Seifert, N. A.; Heger, M.; Thomas, J.; Jäger, W.; Xu, Y. The Rich Conformational Landscape of Perillyl Alcohol Revealed by Broadband Rotational Spectroscopy and Theoretical Modelling. *Phys. Chem. Chem. Phys.* **2019**, *21*, 15408–15416.

- ⁹⁰ Pracht, P.; Bauer, C. A.; Grimme, S. Automated and Efficient Quantum Chemical Determination and Energetic Ranking of Molecular Protonation Sites. *J. Comput. Chem.* **2017**, *38*, 2618–2631.
- ⁹¹ Oswald, S.; Seifert, N. A.; Bohle, F.; Gawrilow, M.; Grimme, S.; Jäger, W.; Xu, Y.; Suhm, M. A. The Chiral Trimer and A Metastable Chiral Dimer of Achiral Hexafluoroisopropanol: A Multi-Messenger Study. *Angew. Chem. Int. Ed.* **2019**, *58*, 5080-5084; *Angew. Chem.* **2019**, *131*, 5134-5138.
- ⁹² Xie, F.; Ng, X.; Seifert, N. A.; Thomas, J.; Jäger, W.; Xu, Y. Rotational Spectroscopy of Chiral Tetrahydro-2-furoic Acid: Conformational Landscape, Conversion and Abundances. *J. Chem. Phys.* **2018**, *149*, 224306.
- ⁹³ Weigend, F.; Ahlrichs, R. Balanced Basis Sets of Split Valence, Triple Zeta Valence and Quadruple Zeta Valence Quality for H to Rn: Design and Assessment of Accuracy. *Phys. Chem. Chem. Phys.* **2005**, *7*, 3297.
- ⁹⁴ Grimme, S.; Antony, J.; Ehrlich, S.; Krieg, H. A Consistent and Accurate *ab initio* Parametrization of Density Functional Dispersion Correction (DFT-D) for the 94 elements H-Pu. *J. Chem. Phys.* **2010**, *132*, 154104.
- ⁹⁵ Grimme, S.; Ehrlich, D.; Goerigk, L. Effect of the Damping Function in Dispersion Corrected Density Functional Theory. *J. Comput. Chem.* **2011**, *32*, 1456-1465.
- ⁹⁶ Alonso, J. L.; López, J. C. Microwave Spectroscopy of Biomolecular Building Blocks. In *Gas-Phase IR Spectroscopy and Structure of Biological Molecules*, Vol. 364; Rijs, A. M.; Oomens, J., Ed.; 2015; pp 335–402.
- ⁹⁷ Miller, R. E. The Vibrational Spectroscopy and Dynamics of Weakly Bound Neutral Complexes. *Science* **1998**, *240*, 447-453.
- ⁹⁸ Juanes, M.; Saragi, R. T.; Caminati, W.; Lesarri, A., The Hydrogen Bond and Beyond: Perspectives for Rotational Investigations of Non-Covalent Interactions. *Chem. Eur. J.* **2019**, *25*, 11402-11411.
- ⁹⁹ Calabrese, C.; Uriarte, I.; Insausti, A.; Vallejo-López, M.; Basterretxea, F. J.; Cochrane, S. A.; Davis, B. G.; Corzana, F.; Cocinero, E. J. Observation of the Unbiased Conformers of Putative DNA-Scaffold Ribosugars. *ACS Cent. Sci.* **2020**, *6*, 293-303.

- ¹⁰⁰ Zhu, P.; Yang, G.; Poopari, M. R.; Bie, Z.; Xu, Y. Conformations of Serine in Aqueous Solutions as Revealed by Vibrational Circular Dichroism. *Chem. Phys. Chem.* **2012**, *13*, 1272-1281.
- ¹⁰¹ Rak, J.; Skurski, P.; Simons, J.; Gutowski, M. Low-Energy Tautomers and Conformers of Neutral and Protonated Arginine. *J. Am. Chem. Soc.* **2001**, *123*, 11695-11707.
- ¹⁰² Simon, A.; MacAleese, L.; Maître, P.; Lemaire, J.; McMahon, T. B. Fingerprint Vibrational Spectra of Protonated Methyl Esters of Amino Acids in the Gas Phase. *J. Am. Chem. Soc.* **2007**, *129*, 2829-2840.
- ¹⁰³ Heaton, A. L.; Bowman, V. N.; Oomens, J.; Steill, J. D.; Armentrout, P. B. Infrared Multiple Photon Dissociation Spectroscopy of Cationized Asparagine: Effects of Metal Cation Size on Gas-Phase Conformation. *J. Phys. Chem.* **2009**, *113*, 5519-5530.
- ¹⁰⁴ Andersson, Å.; Poline, M.; Houthuijs, K. J.; van Outersterp, R. E.; Berden, G.; Oomens, J.; Zhaunerchyk, V. IRMPD Spectroscopy of Homo- and Heterochiral Asparagine Proton-Bound Dimers in the Gas Phase. *J. Phys. Chem. A* **2021**, *125*, 7449-7456.
- ¹⁰⁵ Johnson, E. R.; Keinan, S.; Mori- Sánchez, P.; Contreras- Garcia, J.; Cohen, A. J.; Yang, W. Revealing Noncovalent Interactions. *J. Am. Chem. Soc.* **2010**, *132*, 6498-6506.
- ¹⁰⁶ Emamian, S.; Lu, T.; Kruse, H.; Emamian, H. Exploring Nature and Predicting Strength of Hydrogen Bonds: A Correlation Analysis Between Atoms-in-Molecules Descriptors, Binding Energies, and Energy Components of Symmetry-Adapted perturbation Theory. *J. Comput. Chem.* **2019**, *40*, 2868-2881.
- ¹⁰⁷ Thomas, J.; Jäger, W.; Xu, Y. Chirality Induction and Amplification in the 2, 2, 2-Trifluoroethanol ··· Propylene Oxide Adduct. *Angew. Chem. Int. Ed.* **2014**, *53*, 7277-7280.
- ¹⁰⁸ Klyne, J.; Bouchet, A.; Ishiuchi, S. I.; Fujii, M.; Schneider, M.; Baldauf, C.; Dopfer, O. Probing Chirality Recognition of Protonated Glutamic Acid Dimers by Gas-Phase Vibrational Spectroscopy and First Principles Simulations. *Phys. Chem. Chem. Phys.* **2018**, *20*, 28452-28464.

- ¹⁰⁹ Heaton, A. L.; Armentrout, P. B. Thermodynamics and Mechanism of Protonated Asparagine Decomposition. *J. Am. Mass Spectrom.* **2009**, *20*, 852-866.
- ¹¹⁰ Uddin, K. M.; Warburton, P. L.; Poirier, R. A. Comparisons of Computational and Experimental Thermochemical Properties of α -Amino Acids. *J. Phys. Chem. B* **2012**, *116*, 3220-3234.
- ¹¹¹ Bleiholder, C.; Suhar, S.; Paizs, B. Revising the Proton Affinity Scale of the Naturally Occurring Alpha-Amino Acids. *J. Am. Soc. Mass Spectrom.* **2006**, *17*, 1275-1281.
- ¹¹² Lin, C.; Shishido, R.; Huang, Q.; Fujii, A.; Kuo, J. Vibrational Spectroscopy of Protonated Amine-Water Clusters: Tuning Fermi Resonance and Lighting up Dark States. *Phys. Chem. Chem. Phys.* **2020**, *22*, 22035-22046.
- ¹¹³ Hopkins, W. S.; Marta, R. A.; McMahon, T. B. Proton-Bound 3-Cyanophenylalanine Trimethylamine Clusters: Isomer-Specific Fragmentation Pathways and Evidence of Gas-Phase Zwitterions. *J. Phys. Chem. A* **2013**, *117*, 10714-10718.

Appendix A

Vibrational Spectroscopy of Homo- and Heterochiral Amino Acid Dimers: Conformational Landscape

Supporting Information 1: PDY Calculation

An IRMPD spectrum can be generated by plotting the photo-dissociation yield (*PDY*) at each laser frequency using the following equation:

$$PDY = \frac{\sum_i I_i}{I_p + \sum_i I_i} \quad (1)$$

where I_p is the intensity of the molecular ion after dissociation and I_i is the detected intensity of the ionic fragment i . Since we have one main monomeric fragment, HAsn^+ ($m/z=133$), we can simply it to the contribution of each individual fragment ion is represented by:

$$PDY_i = \frac{I_i}{I_p + \sum_i I_i} \quad (2)$$

where with $\sum_i PDY_i = PDY$. Because of its non-covalently bonding nature, the background dissociation results in non-zero PDY in the monomer mass channels even without laser irradiation. This can be easily corrected by taking the difference of the irradiated (PDY_i) and background (PDY_i^0) scan to obtain the corrected \overline{PDY}_i :

$$\overline{PDY}_i = PDY_i - PDY_i^0 \quad (3)$$

Only one monomeric fragment, HAsn^+ ($m/z=133$), is observed in the current experiments. By monitoring its intensity, I_{133} , and using equation (3), an IRMPD spectrum (red in Figure A-1) is generated. There is a negative band at 3510 cm^{-1} , indicating that I_{133} , is higher with laser is off than with laser on. This can happen because with laser on, HAsn^+ can further dissociate into smaller fragments by losing H_2O and $\text{H}_2\text{O} + \text{CO}_2$, thus generating m/z peak at 115 and 87, respectively. By adding up I_{87} and I_{115} to I_{133} , one obtains $I_{133,\text{sum}}$ which is the amount of HAsn^+ with laser on and without further fragmentation. Since we observed no evidence of further fragmentation of HAsn^+ with laser off, using equation (3) with $I_{133,\text{sum}}$, the proper

IRMPD spectrum is obtained (the blue trace in Figure A-1), with a small positive peak at 3510 cm^{-1} , the same one presented in the main text.

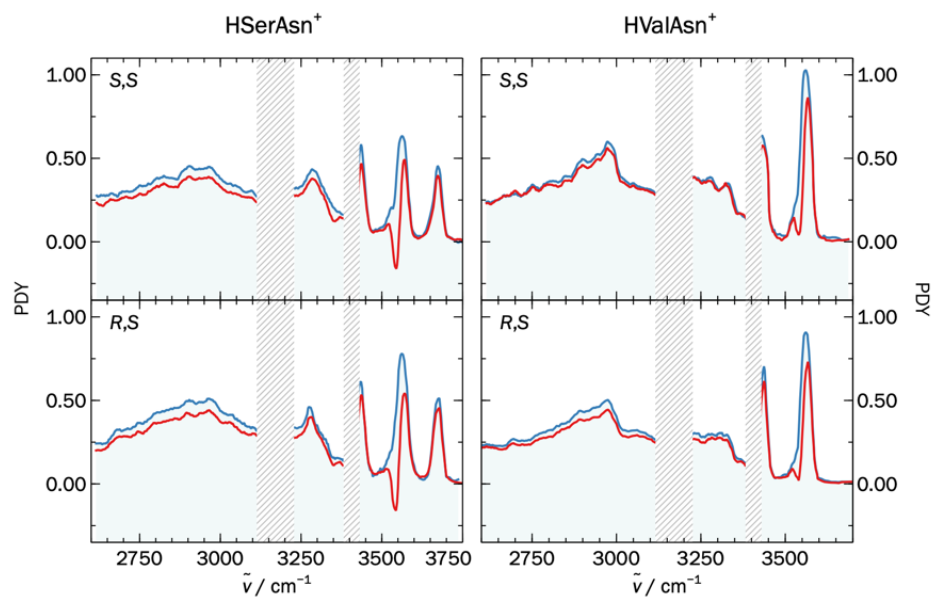
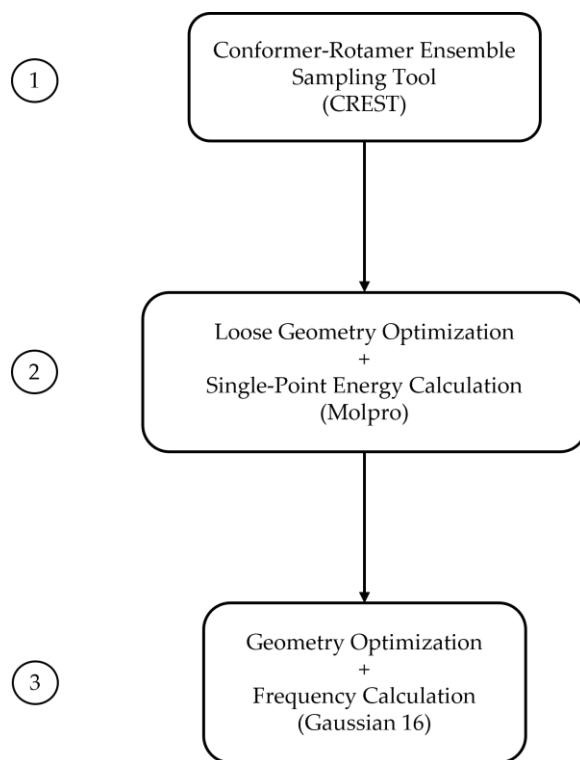


Figure A-1. IRMPD spectra at 15 mJ generated by using the HAsn^+ intensity directly (red trace) and by taking into account the further fragmentation of HAsn^+ (the blue trace). The two laser “blind” regions mentioned are indicated by the shaded areas.

Supporting Information 2: Computational Details

A flow chart of the three-tiered approach is illustrated below:



1. We ran CREST multiple times with the same and different starting geometries including both *cis*- and *trans*-COOH configurations of the three amino acid subunits. To remove the redundant structures, we used a Python program to calculate the root-mean-square deviation (RMSD) of atomic Cartesian coordinates for the obtained conformations. A RMSD value of zero indicates identical conformations, whereas the larger the value, the more unlike the two conformations are. By trial and error, a RMSD threshold of 0.6 was used in the current study. The RMDS program written in Python can be obtained from the authors upon request.

2. The key word line used in the Molpro loose optimization and single point energy calculations is provided below:

```
revPBE-D3(0)/def2-SVP loose opt + B3LYP-D3(0)/def2-TZVP single point
```

Again, we applied the RMSD program to remove redundant structures at this step.

3. We selected all isomers within an energy window of 10 kJ mol⁻¹ using the single point energies obtained above. In the final step, we carried out full geometry optimization and harmonic frequency calculations at the B3LYP-D3BJ/def2-TZVP level using Gaussian 16. The key word lines are provided below:

```
{%chk=}  
# opt b3lyp def2tzvp empiricaldispersion=gd3bj freq
```

```
{title card}
```

```
{charge, multiplicity}
```

```
{molecule specification}
```

In addition, we also carried out single point energy calculations with the inclusion of the mixed solvent using the PCM implemented in Gaussian 16. The key word lines are provided below:

```
{%chk=}  
# sp b3lyp def2tzvp empiricaldispersion=gd3bj SCRF=(Solvent=Generic,  
Read)
```

```
{title card}
```

```
{charge, multiplicity}
```

```
{molecule specification}
```

```
EPS={add the value of linear combination of both solvents}
```

```
EpsInf=(add the value of linear combination of both solvents)
```

The dielectric constant of a binary solvent is calculated using the formula below:

$$\epsilon_m = x_1\epsilon_1 + x_2\epsilon_2$$

where x_1 and x_2 are the mole fractions of solvent 1 and 2, respectively, in the binary mixture, and ϵ_1 and ϵ_2 are their corresponding dielectric constants. The dielectric constants of water and methanol are 78.3553 and 32.613, respectively. The dielectric constant of the 1:1 water + methanol solvent is $\epsilon = 0.5*(78.3553) + 0.5*(32.613) = 55.48415$.

Table A-1. Calculated relative ZPE corrected electronic energies, (ΔE) and Gibbs free energies, (ΔG) in kJ mol^{-1} of the *S,S*-HSerAsn⁺ isomers and the percentage Boltzmann factor (B_f , %) based on ΔG at room temperature

Isomer# ^a	Type	ΔE^b	$\Delta E(\text{PCM})^c$	ΔG^b	B_f
1	ZW	3.7	13.7	0	36.7
2	I	0	28.9	2.5	13.2
3	II	0.7	20.5	3.3	9.7
4	ZW	1.9	1.8	3.4	9.4
5	III	4.0	29.2	4.3	6.5
6	II	2.3	21.7	4.7	5.6
7	OTHER	6.2	32.4	5.6	3.8
8	I	7.2	30.7	6.1	3.1
9	III	4.2	25.5	6.2	3.0
10	ZW	5.6	0	6.4	2.8
11	OTHER	1.2	25.9	6.8	2.4
12	I	6.4	33.2	7.7	1.7
13	OTHER	3.3	30.2	8.7	1.1
14	OTHER	5.3	18.2	9.1	1.0

^a The ranking is based on ΔG . The shaded ones are those observed experimentally.

^b Calculated at the B3LYP-D3BJ/def2-TZVP level of theory using G16.

^c Single point energies at the B3LYP-D3BJ/def2-TZVP level with the inclusion of the 1:1 mixed water + methanol solvent using the PCM model with a dielectric constant of 55.48415.

Table A-2. Calculated relative ZPE corrected electronic energies, (ΔE) and Gibbs free energies, (ΔG) in kJ mol^{-1} of the *R,S*-HSerAsn⁺ isomers and the percentage Boltzmann factor (B_f , %) based on ΔG at room temperature

Isomer# ^a	Type	ΔE^b	$\Delta E(\text{PCM})^c$	ΔG^b	B_f
1	ZW	4.0	14.9	0	38.1
2	ZW	1.9	3.0	3.2	10.5
3	II	0	20.0	3.7	8.5
4	ZW	4.1	0	4.4	6.5
5	I	8.3	32.2	4.5	6.1
6	III	8.7	33.9	4.6	6.0
7	I	6.0	34.6	4.7	5.8
8	II	2.9	23.1	4.8	5.5
9	OTHER	6.7	34.4	5.2	4.8
10	I	4.3	31.9	6.2	3.1
11	OTHER	9.8	32.5	7.3	2.0
12	III	8.8	30.5	8.4	1.3
13	OTHER	4.5	17.1	8.8	1.1
14	OTHER	6.4	22.0	9.4	0.8

^a The ranking is based on ΔG . The shaded ones are those observed experimentally.

^b Calculated at the B3LYP-D3BJ/def2-TZVP level of theory using G16.

^c Single point energies at the B3LYP-D3BJ/def2-TZVP level with the inclusion of the 1:1 mixed water + methanol solvent using the PCM model with a dielectric constant of 55.48415.

Table A-3. Calculated relative ZPE corrected electronic energies, (ΔE) and Gibbs free energies, (ΔG) in kJ mol^{-1} of the *S,S*-HValAsn isomers and the percentage Boltzmann factor (B_f , %) based on ΔG at room temperature

Isomer# ^a	Type	ΔE^b	$\Delta E(\text{PCM})^c$	ΔG^b	B_f
1	I	0	14.7	0	33.6
2	ZW	3.3	0	1.6	17.6
3	I	0.3	13.6	1.9	15.6
4	III	2.7	14.6	2.2	13.6
5	I	0.6	13.8	2.6	11.9
6	OTHER	6.0	20.0	6.0	3.0
7	OTHER	6.0	22.7	6.2	2.7
8	II	2.7	15.5	7.2	1.9

^a The ranking is based on ΔG . The shaded ones are those observed experimentally.

^b Calculated at the B3LYP-D3BJ/def2-TZVP level of theory using G16.

^c Single point energies at the B3LYP-D3BJ/def2-TZVP level with the inclusion of the 1:1 mixed water + methanol solvent using the PCM model with a dielectric constant of 55.48415.

Table A-4. Calculated relative ZPE corrected electronic energies, (ΔE) and Gibbs free energies, (ΔG) of the *R,S*-HValAsn⁺ conformers and the percentage Boltzmann distribution (B_f) of ΔG of at room temperature

Isomer# ^a	Type	ΔE^b	$\Delta E(\text{PCM})^d$	ΔG^b	B_f
1	I	2.0	21.2	0	32.8
2	I	0	16.7	0.1	31.8
3	ZW	3.5	0	1.3	19.4
4	III	2.9	16.8	3.2	9.0
5	I	5.9	16.3	4.8	4.7
6	II	3.9	14.7	7.9	1.3
7	OTHER	7.4	20.9	9.0	0.9

^a The ranking is based on ΔG . The shaded ones are those observed experimentally.

^b Calculated at the B3LYP-D3BJ/def2-TZVP level of theory using G16.

^c Single point energies at the B3LYP-D3BJ/def2-TZVP level with the inclusion of the 1:1 mixed water + methanol solvent using the PCM model with a dielectric constant of 55.48415.

Table A-5. The monomeric composition of all isomers within 10 kJ mol⁻¹ for the four binary species studied

# ^a	<i>S,S</i> -HSerAsn ⁺	<i>R,S</i> -HSerAsn ⁺	<i>S,S</i> -HValAsn ⁺	<i>R,S</i> -HValAsn ⁺
	Type, Ser/Asn Comp ^b	Type, Ser/Asn Comp ^b	Type, Val/Asn Comp ^b	Type, Val/Asn Comp ^b
1	Type ZW1, HS1 ⁺ /ZW	Type ZW1, HS1 ⁺ /ZW	Type I, HV1 ⁺ /A1 ^c	Type I, HV1 ⁺ /A1 ^c
2	Type I, HS1 ⁺ /A1 ^c	Type ZW2, HS3 ⁺ /ZW	Type ZW1, HV1 ⁺ /ZW	Type I, HV1 ⁺ /A1
3	Type II, HS1 ⁺ /A2	Type II, HS3 ⁺ /A2	Type I, HV1 ⁺ /A1	Type ZW1, HV1 ⁺ /ZW
4	Type ZW2, HS1 ⁺ /ZW	Type ZW2, HS2 ⁺ /ZW	Type III, HV1 ⁺ /A2	Type III, HV1 ⁺ /A2
5	Type III, S1/HA ⁺ ^c	Type I, HS1 ⁺ /A1 ^c	Type I, HV1 ⁺ /A1	Type I, HV1 ⁺ /A1
6	Type II, HS2 ⁺ /A2	Type III, S1/HA ⁺ ^c	OTHER, HV1 ⁺ /A2	Type II, HV3 ⁺ /A2
7	OTHER, HS1 ⁺ /A2	Type I, HS1 ⁺ /A1	OTHER, HV1 ⁺ /A1	OTHER, HV1 ⁺ /A2
8	Type I, HS1 ⁺ /A1	Type II, HS2 ⁺ /A2	Type II, HV3 ⁺ /A2	
9	Type III, S1/HA ⁺	OTHER, HS1 ⁺ /A2		
10	Type ZW2, HS1 ⁺ /ZW	Type I, HS1 ⁺ /A1		
11	OTHER, HS3 ⁺ /A2	OTHER, HS1 ⁺ /A2		
12	Type I, HS3 ⁺ /A1	Type III, S1/HA ⁺		
13	OTHER, HS2 ⁺ /A2	OTHER, HS1 ⁺ /A1		
14	OTHER, HS1 ⁺ /A1	OTHER, HS1 ⁺ /A2		

^a Ordering based on the free energy of the most stable isomer of each type. Note that the ordering of Type I and Type II of *S,S*- and *R,S*-HSerAsn⁺ are opposite.

^b The composition of the two monomeric subunits. S = Ser; V = Val; A = Asn; ZW = zwitterionic form. We add “H” and “+” for the protonated species and 1, 2, etc., indicates the relative stability of the protonated subunit going from the most stable one to the least. For the neutral subunits, 1,2, etc. are used to indicate the structural difference among different subunits, rather than energy ordering because the structure inside a dimer species often differs greatly from its isolated ones. See the main text for discussions.

^c The shaded ones are those assigned, i.e. observed experimentally in Figure 3-6 and 3-7.

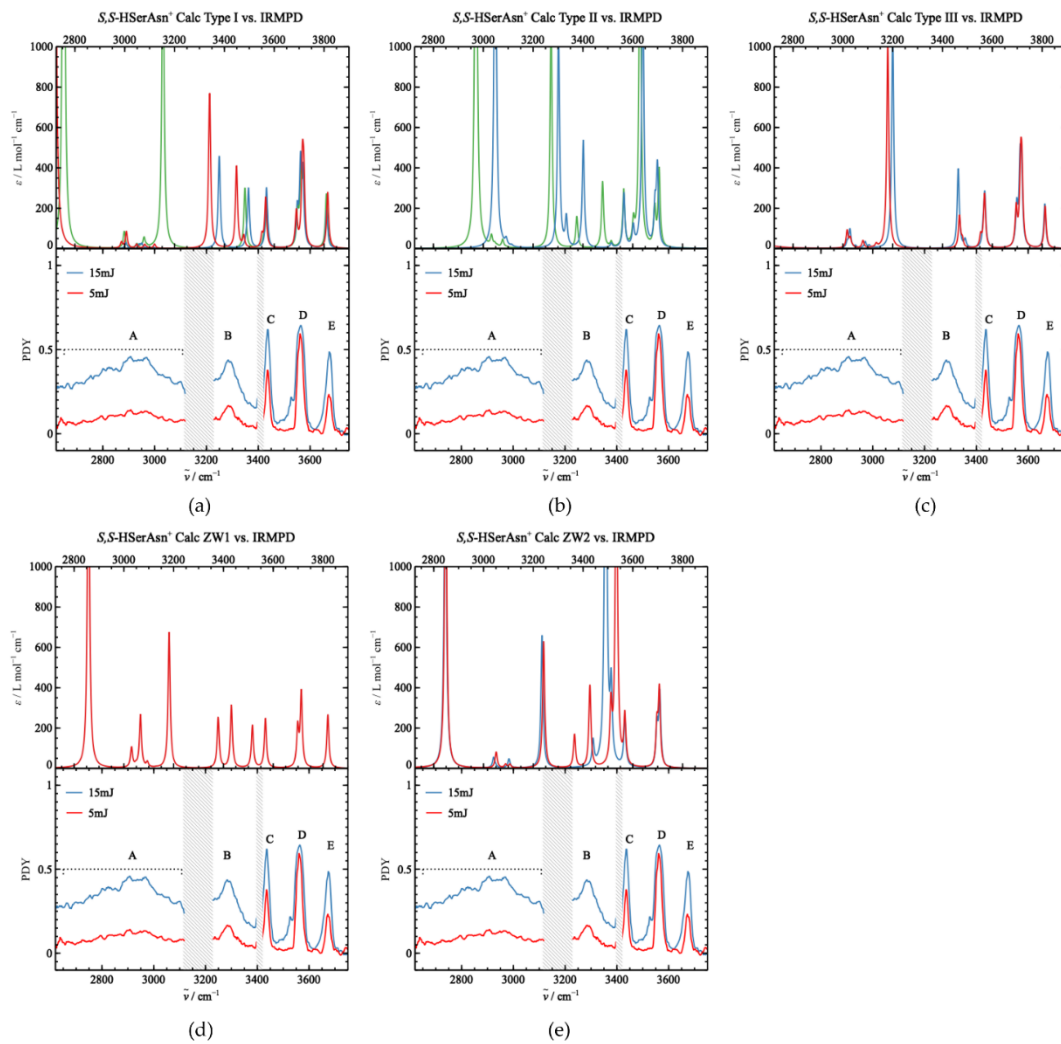


Figure A-2. Comparison of the experimental IR spectra of S,S -HSerAsn⁺ with the combined theoretical IR spectra of all dimer structures in (a) Type I, (b) Type II, (c) Type III, (d) Type ZW1, and (e) Type ZW2.

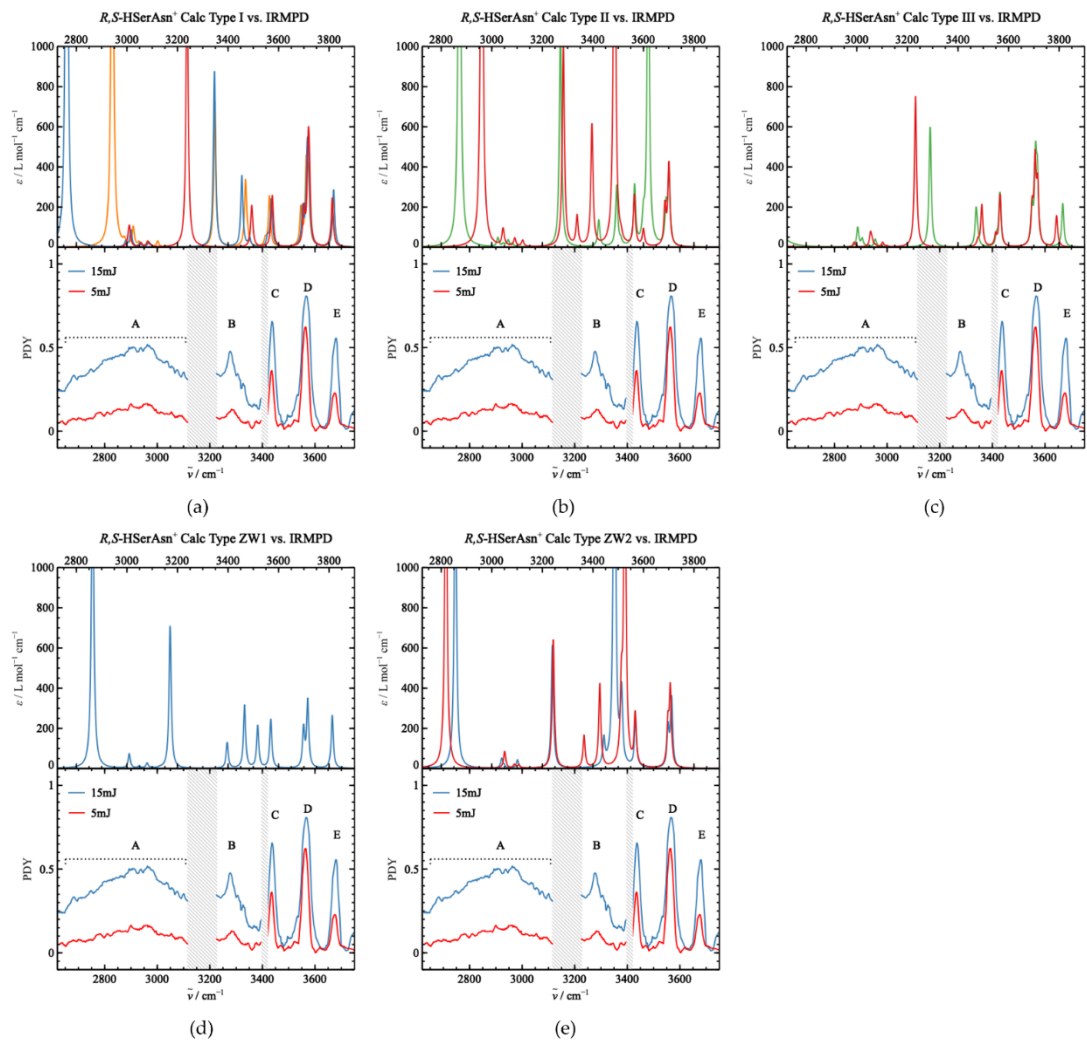


Figure A-3. Comparison of the experimental IR spectra of R,S -HSerAsn⁺ with the combined theoretical IR spectra of all dimer structures in (a) Type I, (b) Type II, (c) Type III, (d) Type ZW1, and (e) Type ZW2.

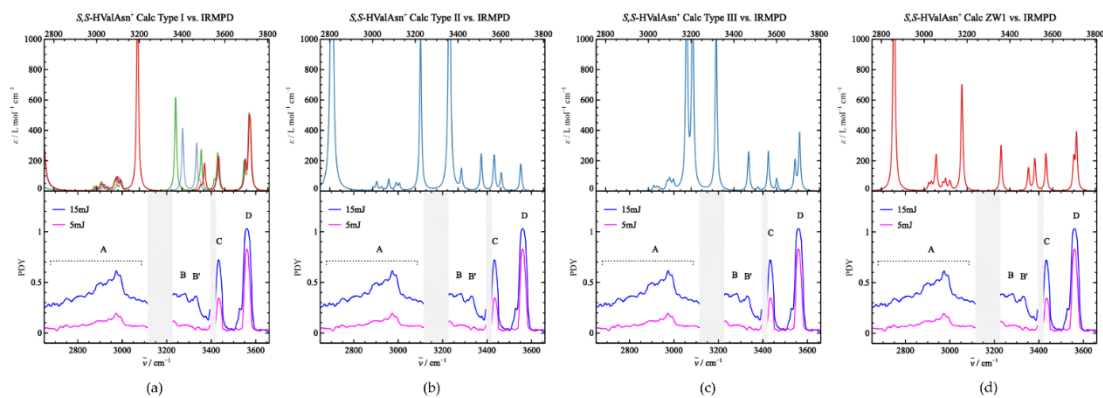


Figure A-4. Comparison of the experimental IR spectra of S,S -HValAsn⁺ with the combined theoretical IR spectra of all dimer structures in (a) Type I, (b) Type II, (c) Type III, and (d) Type ZW1.

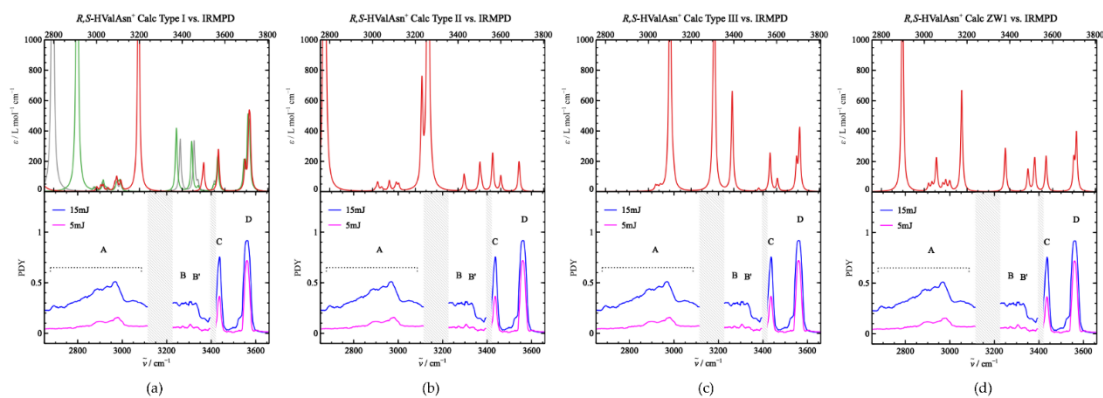


Figure A-5. Comparison of the experimental IR spectra of R,S -HValAsn⁺ with the combined theoretical IR spectra of all dimer structures in (a) Type I, (b) Type II, (c) Type III, and (d) Type ZW1.

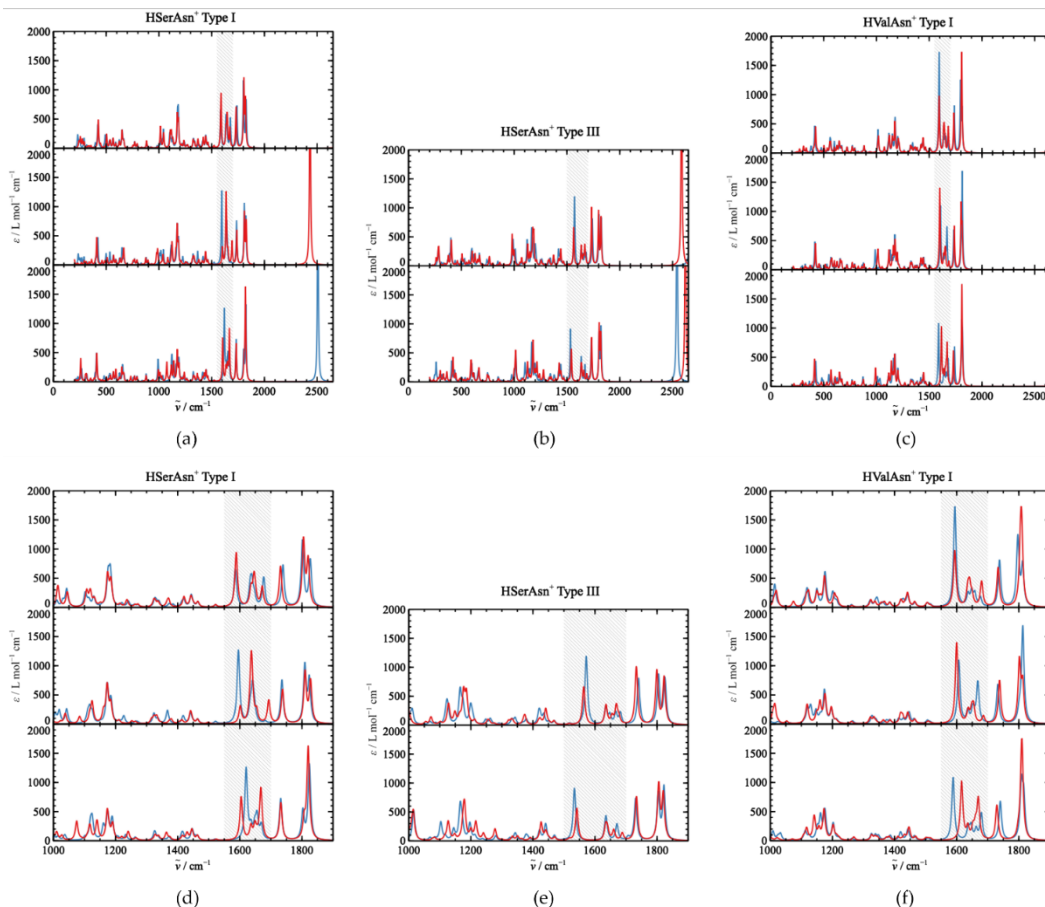


Figure A-6. Predicted IR spectra in the 0-2650 cm^{-1} region of (a) HSerAsn⁺ Type I structures, (b) HSerAsn⁺ Type III structures (c) HValAsn⁺ Type I structures. IR spectra of homochiral dimer species are shown in color red, while IR spectra of heterochiral dimer species are shown in color blue. The corresponding zoom-in spectra in the 1000-1900 cm^{-1} region are given in (d), (e), and (f). The “shaded” area indicates the region where chirality recognition differences between the homo- and heterochiral species are most prominent, where the absorption bands are associated with the scissoring or the twisting motions of the NH_3^+ and sidechain NH_2 functional groups, as well as the NH_3 umbrella bending motion.

Table A-6. Cartesian coordinates of the optimized isomers of *S,S*-HSerAsn⁺

Cartesian coordinates for *S,S*-HSerAsn⁺#1 at the B3LYP-D3BJ/def2-TZVP level of theory.

C	-1.08469700	-0.82051400	-0.12696800
O	-0.42733500	-1.00664400	0.91213500
O	-0.71012300	-0.31430300	-1.21211100
H	0.74835300	0.12994300	-1.18955300
C	-2.55919900	-1.31126500	-0.09119600
N	-2.89118800	-1.47220900	1.36558200

C	-3.54379800	-0.38649600	-0.80292000
C	-3.73782200	0.93221800	-0.07188100
O	-3.76749400	0.96895000	1.16217000
N	-3.91127400	2.02532900	-0.82053500
C	3.37555500	1.05011600	0.60650800
O	3.35731500	2.16687800	0.15720400
O	4.15533500	0.63634400	1.60184500
H	4.70671100	1.37957800	1.89857500
C	2.44061900	-0.04744800	0.11757800
N	1.78707500	0.45695400	-1.12338700
C	3.12094300	-1.37449100	-0.17420400
O	3.93178000	-1.15197900	-1.32057700
H	4.39954400	-1.95738000	-1.56494100
H	-2.57785500	-2.29572700	-0.55840900
H	-3.49891000	-2.25961400	1.57397000
H	-1.96197000	-1.56309800	1.82021900
H	-3.33013500	-0.55453000	1.65135500
H	-4.52652900	-0.86071900	-0.87874500
H	-3.17257700	-0.23318000	-1.81376600
H	-3.86041300	1.99964800	-1.82402000
H	-4.09812200	2.90520300	-0.36417500
H	1.65746200	-0.20554100	0.86330000
H	2.32654000	0.12448600	-1.92673000
H	1.84555400	1.48024500	-1.11653600
H	2.35699700	-2.13443300	-0.36479100
H	3.70762400	-1.67208400	0.69578300

Cartesian coordinates for *S,S*-HSerAsn+ #2 at the B3LYP-D3BJ/def2-TZVP level of theory.

C	-1.48919900	-1.46970800	-0.69196800
O	-0.32162500	-1.59901300	-0.96198500

O	-2.48426300	-1.66197100	-1.56229600
H	-2.10443500	-1.90430400	-2.42237500
C	-2.01923800	-1.15857900	0.70029400
N	-0.89105300	-0.82103900	1.57114700
C	-3.09427100	-0.07113400	0.69744400
C	-2.67929700	1.23258400	0.03124800
O	-1.65455500	1.33397900	-0.63852100
N	-3.52447600	2.26194200	0.20269500
C	2.63019200	-0.77114400	0.38261800
O	2.21944200	-1.05914100	1.47471100
O	3.67850100	-1.33445500	-0.21618200
H	4.05363000	-2.00818700	0.37489800
C	1.98542600	0.27584900	-0.51834600
N	0.89877800	0.92864100	0.25744100
C	2.96424100	1.33467200	-1.00370800
O	3.35107300	2.05665800	0.15669600
H	4.01893700	2.71552600	-0.06045500
H	-2.51836600	-2.08209000	1.02187700
H	-1.21607400	-0.62361900	2.51125000
H	-0.24352700	-1.60085500	1.63966600
H	-3.41263000	0.12462300	1.72428400
H	-3.97237200	-0.44727500	0.16917300
H	-4.38779800	2.16862900	0.71004800
H	-3.34106000	3.12981900	-0.27573500
H	1.53476500	-0.24802200	-1.35920700
H	1.31407300	1.63713700	0.86572900
H	0.33403400	0.24399200	0.84245100
H	0.18348500	1.35618500	-0.34527400
H	2.46964300	1.98529000	-1.73301600
H	3.80924600	0.84265500	-1.48716800

Cartesian coordinates for *S,S*-HSerAsn⁺#3 at the B3LYP-D3BJ/def2-TZVP level of theory.

C	1.45734800	-1.37589000	0.42931000
O	0.75745700	-1.06600200	1.37683700
O	0.99693700	-2.12013400	-0.55799400
H	1.75713500	-2.18723700	-1.19862700
C	2.93401400	-0.99215100	0.29850000
N	3.36091000	-1.29363200	-1.06432500
C	3.17763500	0.43479000	0.79115200
C	2.40512300	1.45043300	-0.03344600
O	1.56267000	1.08432600	-0.85307900
N	2.68360400	2.74226500	0.18922100
C	-3.82197500	-0.01092500	0.01074500
O	-4.25323700	-1.01978100	-0.48003000
O	-4.45863500	1.15362900	0.08459200
H	-5.33339500	1.06480800	-0.33037300
C	-2.45144000	0.05612100	0.67589700
N	-1.76998000	-1.23354900	0.37525900
C	-1.55122800	1.18817300	0.17207000
O	-1.17742400	0.87099600	-1.15095900
H	-0.22998200	1.06591100	-1.26152600
H	3.46037300	-1.67143200	0.97449300
H	3.25013600	-0.50167400	-1.68573000
H	4.30694800	-1.64366200	-1.11840100
H	4.24581800	0.65726100	0.76317700
H	2.85698900	0.52193400	1.83169100
H	3.38928400	3.03176700	0.84492800
H	2.20663400	3.45008200	-0.34708000
H	-2.59505000	0.14023000	1.75389800
H	-0.89714300	-1.34527500	0.94469600

H	-1.45920500	-1.17895900	-0.60346500
H	-2.41235700	-2.02176600	0.46309600
H	-0.67835300	1.25954700	0.82477200
H	-2.10856000	2.12528800	0.22305100

Cartesian coordinates for *S,S*-HSerAsn⁺#4 at the B3LYP-D3BJ/def2-TZVP level of theory.

C	-1.05970700	0.86241900	0.48878700
O	-0.46658400	1.54106800	-0.37676800
O	-0.58036300	0.08550500	1.34243700
H	0.97733300	0.04254500	1.44423100
C	-2.60216400	1.03765400	0.52925700
N	-2.98725100	1.60701500	-0.80734100
C	-3.36951300	-0.24429900	0.84021700
C	-3.28464200	-1.26039300	-0.28762000
O	-3.25922500	-0.89212100	-1.46649600
N	-3.27795700	-2.55140800	0.05477000
C	3.44959000	-1.16008400	-0.17705600
O	3.87228500	-1.74849400	0.78475000
O	3.81984800	-1.37375500	-1.43734400
H	4.49139700	-2.07659800	-1.45768800
C	2.42090300	-0.05248900	-0.08391200
N	2.04936600	0.11287600	1.34977800
C	2.92481700	1.30317600	-0.63887200
O	2.18777100	2.35606100	-0.07152000
H	1.24421300	2.24170900	-0.30374100
H	-2.81175200	1.78669100	1.29302600
H	-3.77747400	2.24609800	-0.77758800
H	-2.12875300	2.07169000	-1.14990100
H	-3.19173100	0.76255700	-1.41029900
H	-4.42883900	-0.02536600	1.00293500
H	-2.97111000	-0.64629500	1.76915900

H	-3.27417800	-2.85054900	1.01449700
H	-3.28604400	-3.25001400	-0.67279300
H	1.52166000	-0.34711300	-0.62431300
H	2.30235100	1.06001500	1.64552400
H	2.54517000	-0.59028900	1.90688800
H	2.86545900	1.27414200	-1.72840500
H	3.96762400	1.45937500	-0.35725100

Cartesian coordinates for S,S-HSerAsn⁺#5 at the B3LYP-D3BJ/def2-TZVP level of theory.

C	1.49366600	1.45557000	-0.42766400
O	0.92980200	1.63061800	-1.47199100
O	2.46669900	2.23478100	0.05612000
H	2.62198600	2.96171100	-0.56997100
C	1.15436600	0.33118700	0.54642200
N	0.35044700	-0.67234500	-0.19877900
C	2.37561800	-0.31296100	1.20606100
C	3.29259800	-0.97980400	0.18673100
O	2.83897400	-1.44057600	-0.85828800
N	4.59104200	-1.05759300	0.50851400
C	-2.82629500	0.66752100	0.65983200
O	-1.78009300	1.13485700	1.03478100
O	-3.93811700	0.63424800	1.39703600
H	-3.75572900	1.03821100	2.26131500
C	-3.05236300	0.03464100	-0.70618700
N	-1.88591900	0.29050300	-1.55033500
C	-3.29343600	-1.46431400	-0.54284700
O	-2.19964700	-2.03459300	0.18352500
H	-2.43076900	-2.93579900	0.43324600
H	0.50878200	0.77189400	1.30563000
H	1.02227800	-1.20894800	-0.77590100

H	-0.15892400	-1.30306900	0.42113400
H	2.04298500	-1.08003400	1.91122000
H	2.90372100	0.44243500	1.78445200
H	4.96450700	-0.64811100	1.34700700
H	5.22041200	-1.52985400	-0.12229000
H	-3.97750300	0.46142300	-1.11011300
H	-0.41561500	-0.23086300	-0.80140800
H	-1.69752400	1.28360500	-1.63994600
H	-2.03444400	-0.07608400	-2.48420600
H	-3.37747500	-1.92290000	-1.53312900
H	-4.23153600	-1.61327900	-0.00639500

Cartesian coordinates for S,S-HSerAsn⁺#6 at the B3LYP-D3BJ/def2-TZVP level of theory.

C	-1.46482400	-1.35304100	-0.55982400
O	-0.60617200	-1.13781800	-1.39539500
O	-1.25941900	-2.17818800	0.44885600
H	-2.09567200	-2.13874700	0.98625600
C	-2.86561400	-0.73626300	-0.60261700
N	-3.51432100	-0.98694700	0.68079200
C	-2.80706100	0.72038800	-1.06395300
C	-2.00327100	1.58468000	-0.10708500
O	-1.28152100	1.07702000	0.75145600
N	-2.11580200	2.91098200	-0.26138200
C	3.44716800	0.16039800	-0.56265700
O	4.12588600	-0.79914300	-0.82092500
O	3.80073900	1.43132600	-0.73060500
H	4.70278600	1.46776900	-1.09272300
C	2.06562200	0.04651700	0.05006800
N	1.67847600	-1.39410300	0.02518600
C	2.02300300	0.54737000	1.51427900

O	0.88945200	0.02788300	2.16042600
H	0.09331100	0.48659400	1.83715500
H	-3.40030700	-1.30553600	-1.36757500
H	-3.37195700	-0.23272100	1.34132700
H	-4.50147500	-1.18456200	0.59733700
H	-3.81896300	1.11368900	-1.17410500
H	-2.33149100	0.77147800	-2.04617400
H	-2.71897700	3.31879200	-0.95534400
H	-1.60132100	3.52609500	0.34918400
H	1.33784300	0.59391400	-0.54614300
H	1.25765700	-1.62865200	0.93374000
H	2.50986300	-1.96229000	-0.17273100
H	0.92800300	-1.54248600	-0.68902300
H	2.05477900	1.63791400	1.50921800
H	2.89557800	0.18028400	2.05766000

Cartesian coordinates for S,S-HSerAsn⁺#8 at the B3LYP-D3BJ/def2-TZVP level of theory.

C	-2.20257500	-1.54852100	-0.14309900
O	-1.38739100	-2.24077900	-0.69619600
O	-3.48496100	-1.45970700	-0.51078200
H	-3.62704900	-2.02977300	-1.28415300
C	-1.93140500	-0.72014300	1.10982200
N	-0.50144400	-0.78972700	1.42586100
C	-2.43494600	0.71917100	0.98975100
C	-1.91589100	1.49169000	-0.21390600
O	-1.28326700	0.96097700	-1.12191000
N	-2.22310600	2.79951500	-0.22918900
C	3.18052900	-0.62441100	-0.02914900
O	4.32706400	0.05154600	0.09493200
O	2.94096800	-1.68288800	0.48299600

H	0.46892900	-0.68965000	0.06686300
C	2.19532300	0.12157700	-0.91692000
N	0.93023800	-0.64744600	-0.91273600
C	1.95083400	1.55854800	-0.44969800
O	1.52588500	1.58716000	0.90589300
H	2.25088200	1.88821500	1.46311200
H	-2.53669000	-1.18653700	1.89609500
H	-0.23557900	-0.07495100	2.09294100
H	-0.26235900	-1.69260300	1.82221300
H	-2.19134000	1.26295400	1.90568600
H	-3.52415200	0.69930100	0.92277800
H	-2.77815700	3.22906800	0.49087000
H	-1.97818100	3.34945900	-1.03707300
H	2.59486900	0.14749900	-1.93373600
H	4.94285500	-0.47178000	0.63523900
H	1.05444200	-1.61466600	-1.20637800
H	0.20244300	-0.19937000	-1.47937700
H	1.15871400	1.99482500	-1.05958300
H	2.86295400	2.13368100	-0.60331500

Cartesian coordinates for S,S-HSerAsn⁺#9 at the B3LYP-D3BJ/def2-TZVP level of theory.

C	-0.85968700	2.11852100	0.17115200
O	-0.50404000	2.67423500	1.17605200
O	-1.09604500	2.70724300	-0.99897800
H	-0.89789500	3.65538900	-0.92094500
C	-1.12985800	0.62479900	0.10565200
N	-0.68398500	0.03136500	1.39344600
C	-2.60424100	0.31090800	-0.16617500
C	-2.87258600	-1.19107200	-0.19879800
O	-2.21820500	-1.97269300	0.48827900

N	-3.87369400	-1.59466900	-0.99315300
C	2.51675400	0.20835100	-0.81399300
O	1.77422500	1.15387200	-0.89699300
O	3.20732000	-0.29617700	-1.83893500
H	3.00780000	0.22132800	-2.63621300
C	2.79195300	-0.55861600	0.46988200
N	2.12195500	0.12834700	1.58044500
C	2.28792100	-1.99362300	0.34041600
O	0.90310100	-1.92730000	0.01586400
H	0.54153600	-2.81335000	-0.09476800
H	-0.50443900	0.19081000	-0.67085500
H	-1.04648700	-0.93961600	1.39726700
H	0.38227900	0.02846000	1.46582400
H	-1.04990800	0.57444800	2.17563100
H	-2.89030800	0.78319800	-1.10469900
H	-3.23562500	0.74531900	0.61571000
H	-4.40697600	-0.95515000	-1.55640800
H	-4.12977900	-2.57012500	-0.99615500
H	3.87973600	-0.59992100	0.59232900
H	2.48207000	-0.21195600	2.46584900
H	2.30256700	1.12709400	1.53989000
H	2.44616900	-2.51585100	1.28989800
H	2.85693900	-2.50442500	-0.43864800

Cartesian coordinates for *S,S*-HSerAsn⁺#10 at the B3LYP-D3BJ/def2-TZVP level of theory.

C	-0.86232900	-0.55848500	-0.34600000
O	-0.57364500	-1.68387000	0.10725200
O	-0.24058900	0.52096900	-0.23165500
H	1.03282300	0.61363400	0.63446600
C	-2.15144800	-0.50552900	-1.21115100

N	-2.94610100	-1.72527500	-0.83690800
C	-2.96613100	0.77462400	-1.04832000
C	-3.62430600	0.87891300	0.31843800
O	-4.04453600	-0.12926300	0.89442100
N	-3.75805300	2.10269700	0.83790400
C	3.65217500	0.92176800	-0.38150600
O	3.27502100	2.05174200	-0.54850200
O	4.61096000	0.31491100	-1.08042300
H	4.96765400	0.93869000	-1.73521500
C	3.08788600	0.00912200	0.68781100
N	1.90309600	0.69211100	1.28248600
C	2.65621900	-1.38417900	0.19916200
O	1.90991300	-1.99969200	1.21865600
H	0.97707900	-2.03942100	0.92237200
H	-1.83546500	-0.60922900	-2.24931300
H	-3.47804300	-2.12908900	-1.60346200
H	-2.24485200	-2.38866700	-0.46355100
H	-3.57879000	-1.40507600	-0.05218200
H	-3.76287000	0.81727200	-1.79664400
H	-2.29728800	1.61242000	-1.23330000
H	-3.40276100	2.92184300	0.37613700
H	-4.24966300	2.21086800	1.71205600
H	3.83771700	-0.10662000	1.47322600
H	2.10161000	1.68191400	1.43028300
H	1.66419000	0.22838500	2.15791100
H	3.55218700	-1.96342800	-0.02437400
H	2.07448500	-1.28600700	-0.72138300

Cartesian coordinates for *S,S*-HSerAsn⁺#12 at the B3LYP-D3BJ/def2-TZVP level of theory.

C	-2.37251000	-1.34137600	0.20242300
---	-------------	-------------	------------

O	-1.57210300	-2.23712700	0.28873900
O	-3.43874400	-1.36029900	-0.60256200
H	-3.43264700	-2.18981600	-1.10738600
C	-2.35459900	-0.07961100	1.06019300
N	-1.14933300	-0.08964400	1.90030100
C	-2.49235200	1.20508100	0.24009200
C	-1.51054100	1.36362700	-0.91083800
O	-0.86176300	0.42167900	-1.36124500
N	-1.44175700	2.59242400	-1.44141700
C	2.34324900	1.05685300	0.55622000
O	3.59471700	1.51273500	0.63584500
O	1.35364600	1.73420000	0.64097500
H	0.45652400	-0.45315700	-0.62048900
C	2.32733200	-0.44979200	0.36382400
N	0.92912500	-0.89653900	0.19059000
C	3.17152300	-0.92871300	-0.81362000
O	2.95653300	-2.32721900	-0.87376300
H	3.45720500	-2.71329300	-1.60058800
H	-3.26301000	-0.14147100	1.67133300
H	-1.02706400	0.80919200	2.35322900
H	-1.24569600	-0.78706300	2.63128900
H	-2.42711600	2.06701800	0.90791400
H	-3.49429200	1.22549600	-0.19366700
H	-1.98558700	3.36188700	-1.09100400
H	-0.85451500	2.74472600	-2.24568900
H	2.71575000	-0.91313900	1.27374900
H	3.57449500	2.47346900	0.78140100
H	0.27569000	-0.62246900	0.98126500
H	0.89148300	-1.90776900	0.06133900
H	4.21657200	-0.67491700	-0.62816900

H 2.84506600 -0.43055400 -1.73451000

Table A-7. Cartesian coordinates of the optimized isomers of *R,S*-HSerAsn⁺

Cartesian coordinates for *R,S*-HSerAsn⁺ #1 at the B3LYP-D3BJ/def2-TZVP level of theory.

C	1.05687500	-0.83084400	0.30774100
O	0.39323400	-1.20795500	-0.67405300
O	0.69330300	-0.11652800	1.27278500
H	1.91727700	-1.95415200	-1.45572600
C	2.52212600	-1.34550400	0.37011600
N	2.84908900	-1.78540000	-1.02913800
C	3.52558500	-0.32502100	0.89942000
C	3.74259000	0.83373800	-0.06005400
O	3.74158200	0.65070300	-1.28122600
N	3.97137800	2.03519700	0.47906100
C	-3.85220800	-0.51711500	0.18163500
O	-4.25880500	-0.67297100	1.30368200
O	-4.53645400	-0.78780800	-0.92716700
H	-5.41372000	-1.12503600	-0.67979300
C	-2.44170900	-0.03031200	-0.12141000
N	-1.85832800	0.44734700	1.16405100
C	-2.36330500	1.08197800	-1.15360600
O	-2.93752600	2.22708700	-0.53575800
H	-2.94353600	2.97197500	-1.14572900
H	2.51974300	-2.22520300	1.01357800
H	3.29239400	-0.94383600	-1.48559900
H	3.45014000	-2.60313500	-1.08384500
H	4.49932100	-0.79557000	1.06395400
H	3.15969300	0.01955800	1.86421400
H	3.94781200	2.18874700	1.47213100
H	4.18191100	2.81156300	-0.12925300

H	-0.78862100	0.23968600	1.21974500
H	-2.03705100	1.45184800	1.24062700
H	-2.35839000	-0.01232600	1.93129400
H	-2.90986400	0.77680900	-2.04669700
H	-1.31499300	1.25007000	-1.41746900
H	-1.83948500	-0.87275700	-0.46841300

Cartesian coordinates for *R,S*-HSerAsn⁺#2 at the B3LYP-D3BJ/def2-TZVP level of theory.

C	-0.92517700	-0.30374300	-0.56905300
O	-0.48814500	0.86689100	-0.59971500
O	-0.39625600	-1.32728300	-0.08520900
H	-1.97366200	-2.34598300	-0.42581900
C	-2.29403100	-0.52839500	-1.26785500
N	-2.81573400	-1.83761600	-0.74585500
C	-3.29542200	0.60430000	-1.05348800
C	-3.79442400	0.67610300	0.38117000
O	-3.98113400	-0.35577600	1.03427100
N	-4.05361600	1.88847100	0.87748200
C	3.98821600	0.53060200	-0.44048100
O	4.29576000	1.68890300	-0.32381400
O	4.75308600	-0.42319600	-0.96557500
H	5.60307300	-0.03720800	-1.23753300
C	2.65578200	-0.02222600	0.02146000
N	1.85465900	1.10689400	0.57310900
C	2.78909800	-1.12538600	1.10155500
O	1.60575500	-1.20442200	1.85436700
H	0.86512200	-1.43172600	1.25620400
H	-2.08958200	-0.64082100	-2.33262800
H	-3.34730800	-2.37601400	-1.42494400
H	-3.40806900	-1.57686900	0.09295300

H	-4.17049500	0.46558700	-1.69487100
H	-2.81034900	1.53008900	-1.35478700
H	-3.88001700	2.72931900	0.35468300
H	-4.44100800	1.96346200	1.80592200
H	0.89055900	1.12086400	0.09043300
H	1.67663600	0.92512100	1.56494200
H	2.37771000	1.97951500	0.44761800
H	3.59063300	-0.87262900	1.79785800
H	3.04883600	-2.06344400	0.60755700
H	2.11397200	-0.42194900	-0.83517600

Cartesian coordinates for *R,S*-HSerAsn⁺ #3 at the B3LYP-D3BJ/def2-TZVP level of theory.

C	1.15173200	-1.42946800	0.52568400
O	0.72415700	-0.94704300	1.55744800
O	0.37610400	-2.07111700	-0.32579100
H	0.97924900	-2.31216900	-1.08092400
C	2.62735300	-1.37285400	0.11834700
N	2.72347300	-1.74932600	-1.28891100
C	3.24510500	-0.03035600	0.51106300
C	2.51175800	1.13917900	-0.12238700
O	1.48415100	0.95991200	-0.78252800
N	3.02997500	2.35496900	0.08875000
C	-3.45414600	-0.38316900	-0.11184100
O	-4.12328100	-0.58735200	0.86802800
O	-3.83168900	-0.59219500	-1.36851400
H	-4.74070000	-0.93805700	-1.37801800
C	-2.05364200	0.19257700	-0.04363400
N	-1.67574900	0.27576900	1.40037100
C	-1.95741500	1.60835300	-0.66483300
O	-0.83435100	2.28007500	-0.15076900

H	-0.01271100	1.90076400	-0.52819900
H	3.11750400	-2.15144600	0.70883200
H	2.65853700	-0.94744700	-1.90434300
H	3.55755200	-2.27755300	-1.50349800
H	4.29876500	-0.01207800	0.22619700
H	3.20274000	0.08869400	1.59576300
H	3.86616100	2.49142500	0.63114900
H	2.58206800	3.16462300	-0.31164500
H	-2.50119900	0.05136400	1.96928800
H	-1.33573500	1.22791600	1.58025600
H	-0.87354400	-0.36676200	1.60929300
H	-2.83344100	2.19729200	-0.38712200
H	-1.93986000	1.51065800	-1.75106500
H	-1.35448500	-0.48091700	-0.53483100

Cartesian coordinates for *R,S*-HSerAsn⁺ #4 at the B3LYP-D3BJ/def2-TZVP level of theory.

C	1.04901500	-1.05763700	0.51928000
O	0.31373100	-0.32235800	1.21492500
O	0.72956300	-1.94797500	-0.29306400
H	2.54315300	-2.14483100	-0.85094700
C	2.57598400	-0.85626800	0.71611600
N	3.22828700	-1.45374800	-0.49928300
C	2.98846900	0.59859000	0.92130000
C	2.78374300	1.43754900	-0.32981900
O	2.99180000	0.95751300	-1.44879700
N	2.41049000	2.70844000	-0.15800800
C	-3.10725200	1.16480200	0.03357800
O	-2.73727600	1.89328200	0.91653100
O	-3.66592000	1.55969400	-1.11112100

H	-3.74447800	2.52842600	-1.10709100
C	-2.99683400	-0.34336000	0.09367600
N	-2.27846600	-0.70116600	1.34940600
C	-2.24464300	-0.97185200	-1.09524000
O	-1.94089000	-2.30553400	-0.77597300
H	-0.97027600	-2.36511500	-0.65499000
H	2.86433600	-1.44842000	1.58466800
H	4.13527200	-1.87739100	-0.32123000
H	3.30173600	-0.65401300	-1.18663300
H	4.04761200	0.66203400	1.18703800
H	2.41492100	0.98638500	1.76010400
H	2.20514000	3.08768700	0.75004000
H	2.32408200	3.30569500	-0.96614000
H	-1.20806500	-0.51996800	1.26478600
H	-2.63193000	-0.15821200	2.13686400
H	-2.39347400	-1.70070800	1.51339200
H	-1.33910200	-0.39451600	-1.30107600
H	-2.88879700	-0.92202800	-1.97333000
H	-4.00126400	-0.76762900	0.14638200

Cartesian coordinates for *R,S*-HSerAsn⁺ #5 at the B3LYP-D3BJ/def2-TZVP level of theory.

C	1.70378600	-1.33336900	0.94486100
O	0.56195200	-1.68598400	1.10665200
O	2.56538100	-1.10175900	1.93686700
H	2.11300400	-1.24140300	2.78469100
C	2.36888400	-1.20191500	-0.41794200
N	1.33223000	-1.31172800	-1.45444700
C	3.20985500	0.06633900	-0.56095300
C	2.45740200	1.35247700	-0.25525100
O	1.35560300	1.34395600	0.28390200

N	3.08521500	2.49090200	-0.59187300
C	-2.80888800	0.85221700	0.73028500
O	-2.52561100	2.00951200	0.58463300
O	-3.82972000	0.38973900	1.45387100
H	-4.30763000	1.14370000	1.83789600
C	-2.00381000	-0.28940600	0.12108000
N	-0.95538500	0.32624400	-0.73535100
C	-2.84588300	-1.23566600	-0.71962800
O	-3.28351700	-0.47475900	-1.83588900
H	-3.93728400	-0.96415700	-2.34577700
H	3.07284800	-2.04250300	-0.46776600
H	1.74760500	-1.18712500	-2.37183500
H	0.94247300	-2.24933200	-1.43722400
H	3.63505900	0.11018800	-1.56662400
H	4.05439700	0.00359400	0.12782400
H	4.00990200	2.49815400	-0.98711900
H	2.66355900	3.37170400	-0.34144800
H	-0.44605800	1.06630200	-0.23464500
H	-1.40267200	0.72791000	-1.56127500
H	-0.20671700	-0.35270600	-1.02986700
H	-3.67577200	-1.60131600	-0.11361200
H	-2.23539300	-2.08976700	-1.03162200
H	-1.50250900	-0.84086000	0.91510400

Cartesian coordinates for *R,S*-HSerAsn⁺ #6 at the B3LYP-D3BJ/def2-TZVP level of theory.

C	-1.88350500	2.03986700	-0.06946100
O	-1.03021300	2.73290200	0.41317700
O	-3.07511200	2.46456600	-0.49722800
H	-3.13872700	3.42401600	-0.35444100
C	-1.72377500	0.54129200	-0.27935200

N	-0.36860200	0.15452800	0.16752200
C	-2.80265300	-0.27841700	0.43283000
C	-2.64416500	-1.77447000	0.16434500
O	-1.56162700	-2.25523300	-0.15241100
N	-3.75161500	-2.51590900	0.32178900
C	2.95119600	0.10146600	0.87639700
O	2.05812400	0.44647100	1.60935300
O	4.03303500	-0.56677400	1.28071600
H	3.96342400	-0.72758500	2.23621100
C	2.99989100	0.36664700	-0.62298200
N	1.91277200	1.28436700	-0.98316400
C	2.86883500	-0.94964900	-1.38660300
O	1.64592200	-1.56374900	-0.99498500
H	1.59937300	-2.45975300	-1.34480800
H	-1.77481000	0.34198700	-1.35155100
H	-0.17460800	0.42630100	1.13256100
H	-0.28695700	-0.86951600	0.06833400
H	-3.78145600	0.07388500	0.11054800
H	-2.74508400	-0.11631800	1.51386800
H	-4.64146600	-2.11536200	0.56314700
H	-3.68801000	-3.51513100	0.20293000
H	1.97001400	1.51851000	-1.96842700
H	1.98301000	2.15171900	-0.45953800
H	0.41603000	0.60803500	-0.39390400
H	3.72682800	-1.58130100	-1.14948200
H	2.87667300	-0.74022700	-2.46202100
H	3.99192800	0.77395900	-0.84647600

Cartesian coordinates for *R,S*-HSerAsn⁺ #7 at the B3LYP-D3BJ/def2-TZVP level of theory.

C	-2.05365800	-1.57245600	-0.11934800
---	-------------	-------------	-------------

O	-1.02759000	-2.11566800	-0.44044400
O	-3.22036400	-1.74531700	-0.74875300
H	-3.08634100	-2.36127900	-1.48751900
C	-2.21098900	-0.67000500	1.09843400
N	-0.88942300	-0.41862900	1.68025800
C	-2.96200700	0.62467800	0.78511500
C	-2.37259000	1.45852800	-0.34375300
O	-1.47360800	1.05089400	-1.07341200
N	-2.92354400	2.67369800	-0.50437300
C	2.86571000	0.27327000	0.97074600
O	2.35074300	-0.43184400	1.79511500
O	4.06742600	0.83912100	1.08144200
H	4.46467900	0.57193400	1.92710500
C	2.18850800	0.67125300	-0.33933800
N	0.92976500	-0.10007300	-0.43997200
C	3.05690500	0.40387600	-1.56142100
O	3.21985800	-1.00314700	-1.60382300
H	3.78739200	-1.25769000	-2.33904000
H	-2.85445800	-1.23584200	1.78439900
H	-0.96253600	0.21107100	2.47150600
H	-0.48430900	-1.28173300	2.03055000
H	-3.02675400	1.23151600	1.69178900
H	-3.98808100	0.37425700	0.50970400
H	-3.69656200	2.99055100	0.05543300
H	-2.62970400	3.24363000	-1.28180100
H	1.12121600	-1.06153200	-0.72933800
H	0.24862400	0.31480000	-1.08751900
H	0.38499200	-0.15449000	0.46978900
H	4.00595600	0.92999500	-1.44599300
H	2.55113000	0.77925100	-2.45787800

H 1.94416900 1.73341200 -0.28617600

Cartesian coordinates for *R,S*-HSerAsn⁺ #8 at the B3LYP-D3BJ/def2-TZVP level of theory.

C -1.21915600 -1.32724400 -0.39388100
O -0.26251600 -0.95339800 -1.04963900
O -1.08003000 -2.14272400 0.63267800
H -2.00038000 -2.24277500 1.00102900
C -2.66779200 -0.95159300 -0.71383900
N -3.49035300 -1.31386100 0.43608800
C -2.76994700 0.49241900 -1.20514400
C -2.30900000 1.47768300 -0.14457300
O -1.76911000 1.08423200 0.88893500
N -2.51593300 2.77682400 -0.40106500
C 3.54361600 0.10345400 -0.52554300
O 3.73517400 -0.76598900 -1.33273300
O 4.09236100 1.31660800 -0.54271200
H 4.68992200 1.38323500 -1.30711000
C 2.63570600 -0.07795600 0.67642500
N 1.92085900 -1.37758500 0.50400800
C 1.59442000 1.02264200 0.88199100
O 0.75145100 0.57918500 1.92055300
H -0.16345600 0.84926600 1.72694800
H -2.94689800 -1.60548700 -1.54486300
H -3.57254500 -0.55380800 1.10063800
H -4.40855900 -1.64842900 0.18017400
H -3.79796300 0.70871300 -1.50150500
H -2.14463700 0.62212600 -2.09126800
H -2.97769000 3.09025300 -1.23780500
H -2.23856600 3.46417500 0.28211000
H 2.56548700 -2.11589300 0.22029200

H	1.16300500	-1.28876900	-0.22884300
H	1.43680000	-1.61238700	1.37237400
H	1.03930700	1.18095700	-0.04721100
H	2.11477700	1.94787500	1.13908900
H	3.25366500	-0.15642600	1.57346700

Cartesian coordinates for *R,S*-HSerAsn⁺ #10 at the B3LYP-D3BJ/def2-TZVP level of theory.

C	-2.30308400	-1.39428000	-0.17570100
O	-1.53051100	-2.14589600	-0.71555500
O	-3.56879800	-1.21638100	-0.56211700
H	-3.73451000	-1.76229400	-1.34789800
C	-1.99515500	-0.59662400	1.08860900
N	-0.58254800	-0.78393700	1.43315700
C	-2.37145700	0.88174400	0.96919000
C	-1.74764300	1.60930100	-0.21217300
O	-1.29664600	1.00823500	-1.18443300
N	-1.77038100	2.94771200	-0.14596300
C	2.45422600	0.99755200	-0.05910600
O	1.54406400	1.56714000	0.47945900
O	3.72954900	1.38700500	-0.03452700
H	3.80351900	2.19574800	0.49865000
C	2.29464900	-0.27449000	-0.88597100
N	0.85664500	-0.61536900	-0.90602300
C	3.10714300	-1.42919500	-0.31579400
O	2.62066200	-1.66245700	0.99555000
H	3.17714400	-2.31250500	1.43793400
H	-2.65575500	-1.01637700	1.85683200
H	-0.29281500	-0.13823600	2.15854900
H	-0.41496300	-1.72444600	1.77399300
H	-2.12267100	1.39255900	1.90198100

H	-3.45495600	0.95302400	0.85485800
H	-2.14992000	3.44179700	0.64286800
H	-1.42091100	3.48118400	-0.92596000
H	0.66018200	-1.49000100	-1.39013300
H	0.25247300	0.11756000	-1.31406100
H	0.43125400	-0.71312800	0.08094500
H	4.16167100	-1.14696400	-0.32117900
H	2.97990700	-2.31111900	-0.95427100
H	2.63569700	-0.07085400	-1.90264200

Cartesian coordinates for *R,S*-HSerAsn⁺ #12 at the B3LYP-D3BJ/def2-TZVP level of theory.

C	-2.66650900	-1.31755000	-0.13227700
O	-2.16987700	-2.40692400	-0.22994000
O	-3.85765000	-0.96358600	-0.61739500
H	-4.26264000	-1.72989500	-1.05771400
C	-1.99429300	-0.15039300	0.57631500
N	-0.73850600	-0.64102900	1.19684600
C	-1.70431700	1.01039200	-0.38256200
C	-0.97803300	2.16230300	0.30164100
O	-0.20154800	1.97138700	1.23587600
N	-1.21134200	3.38306900	-0.20004500
C	2.19137800	0.15222100	-1.10212500
O	1.17859900	0.51697600	-1.64413100
O	3.29350400	0.90314800	-0.99996000
H	3.14087000	1.74537900	-1.45888500
C	2.38058800	-1.21131800	-0.46201100
N	1.09464600	-1.91505100	-0.48958400
C	2.89881000	-1.08584600	0.97573500
O	2.03493400	-0.29118200	1.77885900
H	2.36752200	0.61174000	1.82663500

H	-2.65373900	0.19546400	1.37448100
H	-0.21804000	0.19021400	1.53519000
H	-0.92166000	-1.27773600	1.96932700
H	-2.64724300	1.33896300	-0.81587100
H	-1.05927200	0.67016500	-1.19600400
H	-1.85343200	3.54163700	-0.95694700
H	-0.72273300	4.17251700	0.19301900
H	1.21556500	-2.88618800	-0.22157300
H	0.70358200	-1.90886300	-1.42612400
H	-0.09214700	-1.15526000	0.50881800
H	3.91328200	-0.68907900	0.96457100
H	2.93177700	-2.08107500	1.42304700
H	3.15526800	-1.72431500	-1.04725300

Table A-8. Cartesian coordinates of the optimized isomers of *S,S*-HValAsn⁺

Cartesian coordinates for *S,S*-HValAsn⁺ #1 at the B3LYP-D3BJ/def2-TZVP level of theory.

N	1.21363000	-1.21744500	-1.39901100
C	2.32218200	-1.23843100	-0.44062300
C	1.74603300	-1.28844700	0.96689000
O	0.58500600	-1.49321400	1.21586100
H	0.65247300	-2.05995200	-1.31360100
H	1.56752600	-1.19452600	-2.34919000
H	2.29605200	-1.24684200	2.77161900
H	2.91760700	-2.15628400	-0.53178300
C	3.29452200	-0.07705600	-0.64870900
C	2.73388200	1.29500900	-0.30294000
O	1.65131200	1.44281200	0.25727800
N	3.51532500	2.33605000	-0.63454500
H	3.64401300	-0.07944400	-1.68422700

H	4.17596300	-0.24290500	-0.02671600
H	4.42466600	2.21470000	-1.04665400
H	3.23087700	3.26508500	-0.36681500
O	2.70004300	-1.15835200	1.89308600
N	-0.79508800	0.60933000	-0.62333300
H	-0.18751300	1.27560400	-0.13303100
C	-1.85460100	0.05628800	0.26755700
H	-1.35965000	-0.22097300	1.19657300
C	-2.96830800	1.08039800	0.54991900
C	-2.35066600	-1.22571400	-0.37657500
H	-3.65604100	0.56335600	1.22127700
C	-2.41365200	2.30250900	1.28307500
C	-3.73902200	1.47243600	-0.71184700
O	-1.94852300	-1.64663800	-1.43123000
H	-3.22911400	2.95915400	1.58479200
H	-1.86383400	2.01738100	2.18149400
H	-1.74833900	2.89483700	0.64924600
H	-4.57485200	2.12016200	-0.44989100
H	-3.12166900	2.03743400	-1.41714900
H	-4.14609000	0.60546100	-1.23444300
O	-3.27572500	-1.81876100	0.37677300
H	-3.55877200	-2.63875600	-0.06093100
H	-0.11229400	-0.13284300	-0.96582600
H	-1.20722400	1.05507400	-1.44114800

Cartesian coordinates for *S,S*-HValAsn⁺#2 at the B3LYP-D3BJ/def2-TZVP level of theory.

N	-3.02164900	-1.24642600	1.56568000
C	-2.65640400	-1.29087600	0.10868900

C	-1.21298800	-0.72009000	0.02800000
O	-0.83405300	-0.37225300	-1.11764800
H	-3.58182300	-2.03267700	1.88303100
H	-3.52846400	-0.32872500	1.69630900
H	-2.10205800	-1.20072200	2.04678800
H	-2.60202600	-2.33471600	-0.20000100
C	-3.67263500	-0.55171500	-0.75870000
C	-3.97209600	0.84709100	-0.24404300
O	-4.04742600	1.06873500	0.96829900
N	-4.18564400	1.80015300	-1.15614600
H	-4.62119300	-1.09577000	-0.78275600
H	-3.27909000	-0.52988500	-1.77248200
H	-4.09934300	1.62553800	-2.14213700
H	-4.44157600	2.72491200	-0.84525500
O	-0.57988300	-0.69646000	1.09645200
N	1.61730500	0.50673400	-1.15482600
H	2.11000300	0.11642100	-1.95595000
C	2.32551400	0.17627900	0.12145200
H	1.54295700	-0.01511900	0.86030300
C	3.21040600	-1.07438300	-0.00846500
C	3.06772100	1.43274100	0.54189000
H	3.64887500	-1.20992600	0.98150700
C	2.36026000	-2.30543400	-0.32673000
C	4.34974300	-0.88755500	-1.01140800
O	2.97964400	2.47906200	-0.05191700
H	2.98258800	-3.19998700	-0.32247800
H	1.56425300	-2.43462700	0.40663900
H	1.89931500	-2.23961200	-1.31599900

H	4.99756400	-1.76349700	-1.00412600
H	3.99024700	-0.78105400	-2.03991400
H	4.96643700	-0.01833800	-0.77825400
O	3.78829600	1.24463900	1.64462700
H	4.21499300	2.08352800	1.88694300
H	0.58615700	0.13703500	-1.14909600
H	1.63235700	1.52785800	-1.25864600

Cartesian coordinates for *S,S*-HValAsn⁺#3 at the B3LYP-D3BJ/def2-TZVP level of theory.

N	-0.81539500	-1.01047300	1.36132100
C	-2.21000600	-0.96981900	0.91395300
C	-2.29714900	-1.51927600	-0.50470400
O	-1.39261600	-2.06478900	-1.08720700
H	-0.47086100	-1.96608500	1.38313300
H	-0.73547600	-0.64764400	2.30459000
H	-3.55665400	-1.79917400	-1.88086600
H	-2.84796800	-1.63603900	1.50900400
C	-2.80935900	0.43034100	1.04751100
C	-2.18472200	1.47116800	0.13042500
O	-1.46707000	1.16514300	-0.81604700
N	-2.48873200	2.74958400	0.41584200
H	-2.73311900	0.75735000	2.08729800
H	-3.87507500	0.38085500	0.81652700
H	-3.12524100	2.99646900	1.15429500
H	-2.18151000	3.47531800	-0.21229500
O	-3.53149500	-1.39579900	-0.99771700
N	0.81845900	-0.36531800	-0.82493200
H	0.28823000	0.39095300	-1.26642100

C	2.27403600	-0.09177200	-0.72501800
H	2.70991500	-0.19576700	-1.71957200
C	2.55222900	1.33418200	-0.20697000
C	2.86568700	-1.16576000	0.17390800
H	3.64004900	1.39787100	-0.14323300
C	2.07077700	2.38613500	-1.20778800
C	1.97021400	1.57178600	1.18755000
O	2.20532700	-1.95085500	0.80341300
H	2.38889700	3.37665900	-0.88314500
H	2.48528800	2.21547000	-2.20275000
H	0.98102500	2.41116200	-1.28597300
H	2.31332700	0.83027100	1.91068500
H	2.27558800	2.55230500	1.55115400
H	0.87835400	1.55578200	1.17348800
O	4.19746400	-1.11102800	0.17644100
H	4.54165600	-1.80537500	0.76297200
H	0.59848300	-1.22854400	-1.32443000
H	0.34165100	-0.50166800	0.11564500

Cartesian coordinates for *S,S*-HValAsn⁺ #4 at the B3LYP-D3BJ/def2-TZVP level of theory.

N	-3.21077800	-0.88306700	1.65405700
C	-3.04524600	-1.06585500	0.21428600
C	-1.58906400	-1.45961400	-0.06593700
O	-1.10434200	-1.48040200	-1.17758300
H	-4.10122700	-1.21411100	1.99780500
H	-3.07467300	0.07752400	1.94453100
H	-1.52759900	-1.64890600	1.76838900
H	-3.64059700	-1.93089400	-0.08775400

C	-3.45932900	0.11420500	-0.66725100
C	-2.62754300	1.35630200	-0.39443700
O	-1.52115800	1.28371300	0.14901600
N	-3.15101400	2.52441000	-0.78393900
H	-4.52115600	0.32412700	-0.53136100
H	-3.31261200	-0.15429300	-1.71633700
H	-4.05678000	2.58717500	-1.21693600
H	-2.62011500	3.37150700	-0.65163900
O	-0.89500000	-1.78083100	1.01388100
N	0.93321300	0.30148000	-0.74495500
H	1.35423100	0.82221200	-1.51462600
C	1.95184700	0.05281600	0.31941800
H	1.41096500	-0.30720000	1.19345600
C	2.99537600	-0.99891900	-0.10996000
C	2.57939500	1.40150900	0.62452500
H	3.69234700	-1.04525100	0.72949700
C	2.35899600	-2.37926000	-0.27686900
C	3.77177200	-0.57438700	-1.35796000
O	2.41554200	2.37497500	-0.06424100
H	1.80845500	-2.68037500	0.61416500
H	1.67051700	-2.41941100	-1.12410100
H	3.13673300	-3.11937200	-0.46336400
H	4.23639500	0.40681000	-1.24933100
H	4.56521200	-1.29324600	-1.55834700
H	3.13626800	-0.55608100	-2.24772000
O	3.33605800	1.35135100	1.71956200
H	3.74071400	2.22325200	1.86418700
H	0.49873300	-0.57592000	-1.08194800

H 0.13822400 0.86145600 -0.38469100

Cartesian coordinates for *S,S*-HValAsn⁺ #5 at the B3LYP-D3BJ/def2-TZVP level of theory.

N -1.47519400 -0.10792000 -1.90099900

C -2.61595200 -0.00650300 -0.98176300

C -2.55693400 1.33682400 -0.25946700

O -1.75120000 2.20346400 -0.48864600

H -1.61787700 0.50302900 -2.69853300

H -1.38647800 -1.05406800 -2.25423000

H -3.51629400 2.33790000 1.02016800

H -3.56648000 0.00916200 -1.52825200

C -2.70462600 -1.19758200 -0.02468900

C -1.61983800 -1.26150100 1.03900300

O -0.96308100 -0.27441900 1.36460600

N -1.46721000 -2.44896200 1.64008700

H -2.72216000 -2.12343700 -0.60364100

H -3.66002400 -1.14214500 0.50131400

H -2.01101500 -3.25544000 1.38630300

H -0.80552800 -2.53243700 2.39526600

O -3.56740800 1.46188700 0.60433400

N 0.72498800 0.84429200 -0.44107600

H 0.33034300 0.48787400 0.44821300

C 2.12322400 0.40929800 -0.67529700

H 2.46235500 0.87749400 -1.60156900

C 3.06603900 0.83085700 0.47087700

C 2.09840000 -1.09357600 -0.90014200

H 4.05833500 0.51014400 0.14882500

C 3.08443600 2.35178900 0.63050800

C	2.73376900	0.12459200	1.78634100
O	1.10869400	-1.77475400	-0.81836100
H	3.29480200	2.85722500	-0.31427500
H	2.14046400	2.73444700	1.02728400
H	3.86019400	2.64130900	1.33852300
H	1.74376600	0.39302400	2.16126400
H	2.77478400	-0.96144200	1.68824500
H	3.45620200	0.41187900	2.54959400
O	3.31375700	-1.55143300	-1.20443300
H	3.26400300	-2.51167200	-1.34347800
H	0.62520100	1.85712900	-0.43812300
H	0.02009900	0.46500700	-1.14119500

Cartesian coordinates for *S,S*-HValAsn⁺ #8 at the B3LYP-D3BJ/def2-TZVP level of theory.

N	-3.11442300	-1.36830800	1.39366100
C	-2.87773000	-1.19043800	-0.03569400
C	-1.39594900	-1.47872300	-0.30341000
O	-0.83943000	-1.19528900	-1.35195400
H	-4.01091600	-1.78670100	1.59818900
H	-3.01343500	-0.49096700	1.89111400
H	-1.45207900	-2.12300700	1.41264200
H	-3.41434200	-1.98013700	-0.56901500
C	-3.30347000	0.14891300	-0.65055900
C	-2.50546600	1.31954400	-0.10348600
O	-1.92877700	1.23438500	0.98488700
N	-2.48182600	2.42910500	-0.84609400
H	-4.36082900	0.31776300	-0.43261000
H	-3.20076300	0.10267900	-1.73480500

H	-2.90341700	2.46946100	-1.75775700
H	-1.93905100	3.21832900	-0.53224200
O	-0.77037400	-2.07782000	0.68199200
N	1.80900600	-0.73559900	-1.50140500
H	0.81517000	-1.09850600	-1.51722700
C	2.13442600	-0.26040000	-0.11051400
H	1.95636300	-1.09836600	0.56152700
C	3.58472600	0.23384300	-0.01006800
C	1.10171300	0.83574100	0.14251100
H	3.69250600	1.06288600	-0.71847600
C	3.86202500	0.76393000	1.39809700
C	4.57608100	-0.87190100	-0.38060900
O	0.75657900	1.57454300	-0.75051500
H	3.20752900	1.59329900	1.66279400
H	3.73024400	-0.02148400	2.14496600
H	4.89062800	1.11685600	1.46030100
H	5.59618400	-0.50974400	-0.25822700
H	4.45481800	-1.74269600	0.26786400
H	4.49321600	-1.19955700	-1.42043300
O	0.63597200	0.83079300	1.37279800
H	-0.21912600	1.33154200	1.39354500
H	1.83357400	0.07185800	-2.13026000
H	2.46453000	-1.44585000	-1.82030900

Table A-9. Cartesian coordinates of the optimized isomers of *R,S*-HValAsn⁺

Cartesian coordinates for *R,S*-HValAsn⁺ #1 at the B3LYP-D3BJ/def2-TZVP level of theory.

N	1.20269800	-1.52300800	-0.95360200
C	2.40520300	-1.29105100	-0.14873900

C	2.00608800	-0.97708500	1.28765600
O	0.88865700	-1.07595100	1.73412700
H	0.66179200	-2.29726800	-0.57786300
H	1.46036600	-1.77531600	-1.90122300
H	2.78353600	-0.51216700	2.94177900
H	3.02167300	-2.19617600	-0.07004600
C	3.29990100	-0.21303500	-0.76198100
C	2.69241200	1.18230300	-0.74824100
O	1.70280200	1.45689300	-0.07733200
N	3.32676000	2.09698200	-1.50177500
H	3.55695400	-0.49718400	-1.78518000
H	4.23864200	-0.17414300	-0.20640100
H	4.16714200	1.88281400	-2.01079500
H	3.01897300	3.05596600	-1.46731100
O	3.07113800	-0.65826500	2.02573300
N	-0.76102000	0.28025000	-0.07217600
H	-0.12163300	-0.34116400	-0.64276300
C	-2.14780200	0.39056200	-0.58456000
H	-2.10611500	0.95465500	-1.51843700
C	-3.07337500	1.12419100	0.40616300
C	-2.61424100	-1.01889000	-0.91521400
H	-4.04463600	1.15824100	-0.09020100
C	-2.60087300	2.56060800	0.63430200
C	-3.23210000	0.36058900	1.72214500
O	-1.94301300	-2.00366500	-0.74643500
H	-1.65357600	2.60010500	1.17821000
H	-3.33124100	3.10106800	1.23556200
H	-2.48115200	3.10129400	-0.30656200

H	-2.29847400	0.31467700	2.28900600
H	-3.58634500	-0.65976000	1.56786100
H	-3.95874800	0.86716900	2.35625600
O	-3.84793300	-1.01396600	-1.42024400
H	-4.10989100	-1.92808800	-1.62091900
H	-0.71197000	-0.15796600	0.85281900
H	-0.26885800	1.17415900	-0.00691000

Cartesian coordinates for *R,S*-HValAsn⁺#2 at the B3LYP-D3BJ/def2-TZVP level of theory.

N	-0.83679900	-0.60393100	1.61781700
C	-2.21406200	-0.66436200	1.11495300
C	-2.27240300	-1.62890400	-0.06695700
O	-1.34984400	-2.30603700	-0.44542100
H	-0.61952500	-1.44349100	2.14360700
H	-0.71397900	0.18705800	2.23959400
H	-3.51035200	-2.33296700	-1.30495100
H	-2.89190700	-1.09472800	1.86182700
C	-2.78196500	0.71865200	0.78774700
C	-2.16909800	1.40945700	-0.42041200
O	-1.53614200	0.79699600	-1.27799400
N	-2.41227000	2.72373400	-0.51880100
H	-2.69870200	1.35824300	1.66916500
H	-3.84910500	0.61005500	0.58329900
H	-2.94955000	3.22498100	0.16733200
H	-2.08979300	3.22009500	-1.33425000
O	-3.50411100	-1.68722000	-0.57970000
N	0.77781300	-0.47025400	-0.67249100
H	0.79660100	-1.41498300	-1.05119500

C	2.10994700	0.17982500	-0.70000200
H	2.36335400	0.38809000	-1.74073300
C	3.20556800	-0.72271800	-0.09420600
C	1.98341300	1.50745500	0.02843500
H	4.12264000	-0.13548800	-0.16797100
C	3.38848300	-1.99471600	-0.92351300
C	2.95072500	-1.04049700	1.37977100
O	1.01266300	1.85022700	0.65304100
H	3.55475200	-1.77052500	-1.97856200
H	2.53086500	-2.66865700	-0.84318400
H	4.25303500	-2.55135300	-0.56307200
H	2.06045100	-1.66029800	1.50941400
H	2.83066300	-0.13897200	1.98263700
H	3.79157300	-1.59992700	1.78807700
O	3.09438900	2.23310600	-0.10931100
H	2.98997200	3.06706300	0.37802600
H	0.04715900	0.06035200	-1.18049200
H	0.34137300	-0.53311100	0.29595000

Cartesian coordinates for *R,S*-HValAsn⁺ #3 at the B3LYP-D3BJ/def2-TZVP level of theory.

N	2.99763000	-1.72809400	-1.16449400
C	2.70147200	-1.43656400	0.27967200
C	1.18800700	-1.08761600	0.32380800
O	0.79890100	-0.50240000	1.36426600
H	3.31360000	-0.80878400	-1.57207300
H	3.68300400	-2.46340600	-1.31447000
H	2.06764200	-1.96956900	-1.55987400
H	2.83442700	-2.35584800	0.84964800

C	3.60902300	-0.34557100	0.84090700
C	3.61952800	0.90331100	-0.02558900
O	3.56549300	0.81756500	-1.25591900
N	3.72626700	2.07905000	0.60180700
H	4.64082900	-0.70240200	0.90905800
H	3.26888800	-0.12755200	1.85090100
H	3.75248600	2.14949600	1.60409800
H	3.80242700	2.92088900	0.05170500
O	0.52126500	-1.44415100	-0.66204400
N	-1.78000700	-0.12725600	1.34587200
H	-2.00784900	0.73968700	1.82968100
C	-2.29259500	-0.10220300	-0.05897300
H	-1.59725600	-0.71340800	-0.64028500
C	-2.32444500	1.31975200	-0.64194200
C	-3.63516700	-0.81248700	-0.04552200
H	-2.70287800	1.19551300	-1.65778900
C	-0.91348200	1.90491300	-0.72695200
C	-3.28365200	2.24258100	0.11154700
O	-4.07912500	-1.36168900	0.93170200
H	-0.94252400	2.87421700	-1.22439200
H	-0.24654200	1.25062500	-1.28831900
H	-0.47636600	2.06073900	0.26262500
H	-3.34793800	3.20468500	-0.39568900
H	-2.94605300	2.45640500	1.13079800
H	-4.29267200	1.83163400	0.16862000
O	-4.23090700	-0.78192300	-1.23580500
H	-5.06377200	-1.27985100	-1.18114300
H	-2.26715500	-0.88005300	1.84330400

H -0.69667500 -0.28482800 1.37196000

Cartesian coordinates for *R,S*-HValAsn⁺ #4 at the B3LYP-D3BJ/def2-TZVP level of theory.

N -3.13958500 -0.93988100 1.57067500

C -3.00141100 -1.15376100 0.13223300

C -1.54851400 -1.53997600 -0.16502200

O -1.07457400 -1.55643000 -1.28224100

H -4.02575700 -1.25849400 1.93667500

H -2.99479700 0.02700400 1.83500500

H -1.45429400 -1.71525500 1.66963900

H -3.59431200 -2.03138400 -0.13717600

C -3.44249200 -0.00006300 -0.77016300

C -2.61514600 1.25630500 -0.55163700

O -1.51294000 1.21632100 0.00116200

N -3.14488700 2.40052500 -1.00283000

H -4.50200400 0.20767100 -0.61351000

H -3.32062900 -0.29583500 -1.81496300

H -4.04585800 2.43331800 -1.44886800

H -2.62367700 3.25815000 -0.90849000

O -0.83727500 -1.85577700 0.90400500

N 0.99864100 0.15611300 -0.81406000

H 0.30280300 0.76578200 -0.36226000

C 2.08614100 -0.30501200 0.10587300

H 1.77303800 -1.25704500 0.53096700

C 2.36599200 0.70099400 1.24093200

C 3.30437900 -0.51749600 -0.77948100

H 3.23825100 0.29414700 1.75688100

C 1.20603200 0.74642800 2.23644700

C	2.72108200	2.09188100	0.71285500
O	3.36954600	-0.10680400	-1.91054800
H	1.46795300	1.39275200	3.07398700
H	0.98462400	-0.24536800	2.63197700
H	0.29445700	1.14851900	1.78988300
H	1.86994900	2.56885300	0.21962100
H	3.55366400	2.07057900	0.00835900
H	3.00712900	2.73778200	1.54205500
O	4.26808800	-1.17374200	-0.14226400
H	5.03447800	-1.26814600	-0.73306600
H	0.43985200	-0.64436900	-1.17503400
H	1.43679700	0.62971500	-1.61129100

Cartesian coordinates for *R,S*-HValAsn⁺ #5 at the B3LYP-D3BJ/def2-TZVP level of theory.

N	-1.45889500	-0.47509800	1.86210600
C	-2.63405300	-0.59830400	0.98693900
C	-2.33985200	-1.63847800	-0.08732800
O	-1.37653500	-2.36198400	-0.08526700
H	-1.33659500	-1.33956400	2.38126400
H	-1.61358400	0.25648600	2.54752800
H	-3.12105300	-2.40795500	-1.62253800
H	-3.49688700	-0.99883600	1.53398500
C	-3.08340600	0.74717200	0.41804400
C	-2.12719700	1.36682300	-0.58923900
O	-1.18618800	0.74413100	-1.06983400
N	-2.39332400	2.63921800	-0.93108300
H	-3.26132800	1.44657800	1.23876500
H	-4.04435000	0.60882300	-0.08109800

H	-3.20056300	3.12945400	-0.58527000
H	-1.84789100	3.07187800	-1.65982100
O	-3.32605700	-1.70412000	-0.98523100
N	0.85186300	-0.63603800	0.15746000
H	0.11071600	-0.52437900	0.89480200
C	2.21023100	-0.19580200	0.57519600
H	2.32470800	-0.45820200	1.62942900
C	2.41086300	1.32052800	0.41220600
C	3.20790300	-1.04209500	-0.20581200
H	3.42040600	1.50927500	0.78080200
C	1.42761500	2.09867700	1.28812400
C	2.34362500	1.76392200	-1.05062700
O	2.87905000	-1.92855200	-0.94890500
H	1.48480300	1.78606600	2.33263800
H	0.39876400	1.97336100	0.94491800
H	1.65555300	3.16349400	1.24794400
H	1.34447100	1.63840800	-1.47410900
H	3.05283000	1.22086100	-1.67677800
H	2.58958100	2.82307700	-1.12304600
O	4.46502900	-0.69185600	0.06299100
H	5.06578000	-1.27285800	-0.43344300
H	0.86243900	-1.61691900	-0.13557600
H	0.47793100	-0.10122000	-0.63482800

Cartesian coordinates for *R,S*-HValAsn⁺ #6 at the B3LYP-D3BJ/def2-TZVP level of theory.

N	-3.69292500	-1.17674100	0.91362600
C	-3.11669700	-0.86623600	-0.39117800
C	-1.67993600	-1.39801800	-0.40162700

O	-0.85306000	-1.09374700	-1.24703200
H	-4.67410200	-1.41326700	0.86839100
H	-3.54549700	-0.42060200	1.57186600
H	-2.23288800	-2.25642500	1.12432200
H	-3.64219100	-1.46316500	-1.14190300
C	-3.16845700	0.59701000	-0.84077100
C	-2.28134700	1.48059500	0.01806000
O	-1.81732400	1.05147900	1.08156400
N	-2.04154600	2.71360300	-0.42790200
H	-4.19910700	0.95471800	-0.78623100
H	-2.85538100	0.67453800	-1.88278100
H	-2.35392200	3.01837900	-1.33399500
H	-1.37344100	3.28809500	0.06290400
O	-1.40491500	-2.24500300	0.56455200
N	1.66576600	-1.52906700	-0.39494300
H	0.70090200	-1.49781100	-0.83580700
C	2.29172800	-0.15560500	-0.42709400
H	2.44149900	0.09614800	-1.47585200
C	3.62659400	-0.13125100	0.33272900
C	1.25499900	0.81127300	0.13627400
H	3.41274500	-0.39459400	1.37440200
C	4.21716900	1.27962300	0.30296100
C	4.61223500	-1.14919800	-0.24622800
O	0.99832900	1.86940800	-0.36882700
H	3.55040700	2.01515100	0.75121500
H	4.42557400	1.59457600	-0.72145900
H	5.15507100	1.29568600	0.85665500
H	5.56645400	-1.07740500	0.27430000

H	4.80012200	-0.95643700	-1.30530600
H	4.28062200	-2.18480700	-0.13450900
O	0.68653600	0.30723700	1.23019600
H	-0.16730900	0.78527300	1.40916800
H	1.52455600	-1.82221200	0.57387400
H	2.25255400	-2.21456000	-0.86709900